Ultrasound Harmonic Classification of Microemboli

ISBN 90-77595-64-3

Printed in The Netherlands by: Optima Grafische Communicatie, Rotterdam.
Cover illustration: Harmonic Bubbling.

Ultrasound Harmonic Classification of Microemboli

Harmonisch ultrageluid voor het classificeren van Micro-embolieën

PROEFSCHRIFT

Ter verkrijging van de graad van doctor
aan de Erasmus Universiteit Rotterdam,
op gezag van de Rector Magnificus
Prof. dr. S.W.J. Lamberts,
en volgens het besluit van het College voor Promoties.

De openbare verdediging zal plaatsvinden op
woensdag 22 september 2004 om 15:45 uur

door

Peggy Christiane Palanchon

geboren te Rosny-Sous-Bois, Frankrijk.

PROMOTIECOMMISSIE

PROMOTORS	Prof. dr. J. Klein Prof. dr. ir. N. de Jong
OVERIGE LEDEN	Prof. D.H. Evans Prof. dr. ir. A.F.W. van der Steen Prof. dr. B.F. Lachmann Prof. dr. ir. N. Bom Prof. dr. H.H.M. Korsten dr. R.G.A. Ackerstaff dr. G.H. Visser

The financial contributions of Terumo (Tustin CVS, USA), Bracco Research S.A. (Geneva, Switzerland), Oldelft (Delft, the Netherlands), Spencer Technology (Seattle, USA) are gratefully acknowledged.

Financial support by the Netherlands Heart Foundation for the publication of this thesis is gratefully acknowledged.

A Ayache et Enzo,

A mes parents,

Contents

Chapter 1

General introduction

1.1 Embolus and embolism

An embolus is defined as a foreign body that arises from a location and travel in the blood stream. It may consist of gas bubbles or biologic aggregates such as blood clots, fat cells, tumor tissues, platelet aggregates or fibrin clots. A single or multiple emboli can result in a sudden interruption of blood flow to an organ or body part called embolism. Depending on the clinical situation, the nature, the size and the number of emboli can show important variations. For instance, up to 620 embolic events per 30 minutes period were recorded in patients with prosthetic heart valves[1] while patient with carotid plaque can produce only a single embolus per hour. It is quite complex, however, to estimate precisely the size range of clinically significant embolus. Literature indicates that an embolus size can vary from $20\,\mu$m to $300\,\mu$m[2,3].

The consequences of an embolism are strongly correlated to the embolus type (nature, number and size) and the location of the embolism. They can either be immediate or appear slowly over the time[4,5]. Embolism can lead to momentary neurological deficits up to heart attack and stroke. Stroke is the third leading cause of death in western countries and 80% of them are a direct result of a cerebral thrombosis or embolism blocking an artery in the brain or in the neck.

1.2 Sources of embolization and associated symptoms

Emboli have been reported in a wide variety of clinical fields. A short description of the possible sources of embolism and its outcome is given below.

- Cardiac surgery: Neuropsychological and neurological deficits after routine Cardiopulmonary bypass surgery (CPB) have been reported in up to 79% of patients[6] and are attributed to the presence of microemboli[7,8]. These neurological deficits range from postoperative delirium to intellectual function and memory deficits to stroke[9,10]. The microemboli have been reported to be both gaseous[11,12] or particulate[13]. Despite the use of membrane oxygenators and filters in the arterial line, microemboli can pass into the circulation and microembolic events were noticed during several stages of the intervention: aortic cannulation and decannulation, cross-clamping of the aorta, and at the start of cardiac ejection[14,15].

- Carotid Endarterectomy (CEA): Embolic events were recorded during each stage of the operation and they can be both gaseous or particulate emboli[16]. Particulate emboli were noticed before, during and after the dissection phase and they are produced by the rupture of an atherosclerotic plaque or by the breaking off of a thrombus formed on an ulcerated surface. Gaseous emboli mainly occur upon release of common carotid artery crossclamps or during manipulations for inserting a shunt[17].

- Carotid artery and middle cerebral artery stenosis: A stenosis is defined as an atherosclerotic plaque appearing on the carotid wall and causing a narrowing of the vessel. An unstable plaque can break off into small pieces that will move and obstruct small brain vessels thereby leading to ischemic stroke. *In-Vivo* studies have shown that a high number of particulate embolic events were detected especially in patients with high-grade stenosis[18−20].

- Prosthetic heart valve: prosthetic heart valve replacement, particularly when mechanical devices are used, is associated with the generation of microemboli that can persist through out the follow up period. They can be either fibrin or platelet microemboli or gaseous bubbles produced by cavitation occurring around the prothesis[1,21−23].

- Cerebral angiography: neurological complications following angiography are supposed to be the result of microembolism. Most of them are gaseous emboli and they are produced during catheter flushing and contrast injection. Nevertheless, some particulate emboli may also arise from clot adherent to guidewires and atheromatous debris[24,25].

-Cerebral angioplasty: The most common complication of carotid angioplasty is distal embolization of debris and/or thrombus. Nevertheless, some clinical studies have shown that most of them are asymptomatic[26−28].

- Atrial fibrillation: Atrial fibrillation is a disorder of the heart beat leading to the formation of stagnant blood within the atria. Clots can be formed from this blood and enter into the circulation. Atrial fibrillation is the cause of 15% of all strokes[29].

- Diving and hyperbaric medicine: gaseous bubbles released in the tissue or the bloodstream during compression or decompression exposure are considered precursors to decompression sickness. They can affect nerves, arteries, veins, muscles and bones[2,30].

Microembolic signals were also reported, to a less extend, in the following clinical situations: patient with bone fractures[31]; patient with acute myocardial infarction[32], detection of right-to-left shunts[33]; during aneurysmal subarachnoid hemorrhage[34]; Eisenmenger's syndrome[35]; mitral valve prolapse[36]; dilative cardiomyopathy[37]; left ventricular assist device[38]; bacterial endocarditis[39] and Sneddon syndrome[40].

1.3 Emboli detection techniques

Transcranial Doppler (TCD) is nowadays recognized as a valuable instrument in the detection of microemboli. The ability of Doppler ultrasound to detect emboli circulating in the blood stream was first described in the sixties during cardiopulmonary bypass and experimental hyperbaric decompression[8,41]. Conventionally, the middle cerebral artery is insonated using a TCD device transmitting a frequency between 2 MHz and 2.5 MHz. The Doppler probe is adequately fixed over the temporal bone and the Doppler sample volume depth is set between 50 mm and 55 mm. The principles underlying the Doppler technique are simple: when a moving particle (particulate or gaseous) is passing through the Doppler sample volume, the impedance mismatch between the embolus and the surrounding medium leads to an increase in the received Doppler signal which can be clearly distinguished from the background flow signal (Figure 1.1).

Figure 1.1: *Microembolic signal in the Doppler waveform.*

Microembolic signals (MES) present specific features that were firstly catalogued by Spencer[42] and next by the Consensus Committee of the Ninth International Cerebral Hemodynamics. They are summarized in Table 1.1. Transient signals may also be induced by patient or transducer movements and by surgical manipulations and therefore be falsely classified as MES signals. The distinction between both signals can be performed by exploiting the specific characteristics of artifacts[42] presented in Table 1.2. The detection of MES using TCD monitoring, is based on the previous features, and in particular on the measurement of the relative intensity increase also called Embolus to Blood Ratio (EBR). This ratio is defined as the difference between the acoustic power from the embolus signal and that of the surrounding medium expressed in dB[43]. The EBR is strongly correlated to the nature and the size of the embolus (gaseous emboli produce stronger signals than solid particles), the Doppler sample volume (smaller volume leads to a better detection) and the technical settings (gain, frequency)[44]. The discrimination between true MES and artefacts is a crucial point in TCD monitoring. It is not an easy task: there are many circumstances where a MES and an artefact present the same signature. For instance, MES due gaseous emboli can conduct to an

Basic Criteria of Doppler Microembolic Signals
1- Short duration signal (between 1 and 100ms)
2- Duration depends on the travel time through the Doppler sample volume
3- High intensity signal (increase of the amplitude between 30 dB and 60 dB above the background Doppler level)
4- Unidirectional signal (as long as it remains in the dynamic range of the Doppler system)
5- Appear randomly within the cardiac cycle
6- Characterized by a particular auditory effect (harmonic chirps or clicks depending on their velocity)

Table 1.1

Basic Criteria of Doppler Artefact Signals
1-Bi-directional signals (they appears simultaneously above and below the Doppler baseline)
2-High power in the low frequency region
3-Sound like noisy impact

Table 1.2

electronic saturation of the TCD system. Indeed, the MES will appear bi-directionally on the TCD waveform. The gold standard remains the human experts who analyze the audio Doppler signals. Nevertheless, it is costly, requires man power and is time consuming and therefore it is restricted to research studies. To enter into a clinical routine, several approaches have been investigated to develop an automated detection system.

On-line detection systems using a neural network showed good performance but their sensitivity remained low[45–47]. Lately, the use of a frequency filtering approach was found to be valuable in improving the detection of MES and their discrimination from artefacts. This technique is based on the principle that MES reach their maximum intensity over a narrow frequency band whereas the intensity of artefacts is concentrated at low frequencies. Using this technique, the EBR could be increased by up to 3 dB[48,49] which is important to detect MES of low intensity from Doppler speckle. The performance of an online system has been tested using various embolic sources. This system led to similar sensitivity and specificity to that of human experts for signals recorded after carotid endarterectomy and in patients with symptomatic carotid stenosis while the results are less good when emboli are due to asymptomatic carotid stenosis and atrial fibrillation[50,51]. Fan et al.[52] have reported an automated method using a ‘rule based expert system’. It exploits the knowledge acquired over the years concerning the characteristics of MES signals and artefacts. It is based on the Fast Fourier Transform (FFT) approach that uses both the time domain and the frequency domain features of the embolic signals. The preliminary results look promising with a sensitivity of 94.7% and a specificity of 95.1% which is comparable to the results from human experts. The low sensitivity of the TCD methods to detect MES has been attributed to use of the FFT that cannot provide a good temporal and spectral resolution simultaneously. Some alternatives have been proposed and the most effective method consists of studying the Doppler signal using the wavelet analysis. The MES signal is decomposed into a set of functions whose time and duration are jointly defined. The high frequency components are filtered using narrow time windows while larger windows are applied to low frequency components. The preliminary results emphasize the good performance of this signal analysis[53,54]. Various other signal analysis approaches have been investigated in order to improve the embolus detection such as the pseudo-Wigner distribution function (WDF)[55,56], the non-linear forecasting[57], methods based on the postembolic spectral patterns[58] or on the narrow band hypothesis[59] and parametric autoregressive modelling[60], but they did not contribute to significant improvement in TCD performances.

The dual-gate or multigate approach could offer an appreciable progress towards a better discrimination between embolic signals and artefacts. The approach is based on the assumption that an embolus will travel with the blood flow while artefact will not. Therefore, if the artery is insonified at two depths, an embolic signal will be characterized by a time delay between the two channels whereas an artefact will occur simultaneously in both channels. The discrimination between true MES and artefact is based on the occurrence of this time delay between both Doppler signals. Preliminary reports showed promising results both *in-vitro* and *in-vivo*, with a sensitivity approaching 100% when the measurements of the time delay are performed manually[61–64]. Nevertheless, when this technique is applied to automatic detection, its sensitivity is not superior to those reported in previous methods. The main limitation of this approach results from a low signal to noise ratio which do not allow detection of embolus. A second limitation is coming from the artery anatomy. The insonification of the vessel at two separate locations requires an adequate temporal window that may be difficult to obtain. Furthermore, Smith et al.[65] reported that emboli may slip from one artery to another, in which case the embolic signal will appear only in one channel. Therefore, the performance of this method can be seriously reduced. Molloy and Markus[66] have reported a decay in sensitivity from 98.9% down to 75.2% in the case of a MES that was detected only in a single channel. To overcome this limitation, a variant of the multigate approach was proposed by Russel[67]. The second sample volume takes place outside the vessel, close to the temporal bone and it is called 'reference gate'. Therefore, only artefacts will lead to an intensity increase in the second sample volume. This technique is also based on multifrequency Doppler that insonates both sample volumes simultaneously at frequencies of 2 and 2.5 MHz. A new parameter derived from this multiple insonification is defined: the quarter Doppler shift, directly derived from the Doppler shift formula. This approach leads to a sensitivity of 98.6%, but the contribution of the quarter Doppler shift compared to the reference gate is not clearly specified. Combining the multigate approach with the characteristics of the backscattered signal could improve the MES detection. Indeed, Devuyst et al.[54,68] combined the dual-gate TCD with the wavelet representation to classify MES. Their off-line automated system reached a sensitivity of 97% and a specificity of 98% for separating artifacts from MES signals.

The second challenge in the microemboli research field is the discrimination between gaseous and solid emboli. Previous studies have demonstrated that the EBR is strongly dependent on the composition and the size of an embolus[69,70].The intensity of the Doppler signal is directly correlated to the acoustic impedance mismatch between the embolus and the surrounding blood where larger difference in impedance gives rise to higher signal intensity. The acoustic impedance of the whole blood, a gaseous embolus and a solid particle (fat cells) are respectively 1.47 MRayls, 368 Rayls and 1.68 MRayls. Consequently, gaseous emboli produce stronger signals than particulate emboli. The EBR is also strongly dependant on the embolus size: a larger embolus produces a higher intensity. Indeed, the EBR cannot be used as a unique parameter to characterize an embolus since a small air bubble can produce an intensity increase similar to the one generated by a large solid embolus.

Several attempts have been made to develop a method to classify the MES based on the determination of several parameters such as the MEP, the embolic duration, the embolic velocity and the effective sample volume length (SVL) defined as the product of the embolic velocity and duration[69−73]. A more complex approach, based on a classification tree, was developed by Devuyst et al.[68]. MES are classified as solid or gaseous matter, by extracting only four parameters from the TCD signals: the peak frequency, the time delay, the relative power and the symmetry of the signal envelope. They achieved a specificity of 86% and a sensitivity of 89%. Recently, the technique using dual frequencies was also investigated by Russel[67]. The method is based on the theory that solid emboli scatter stronger signals at high frequency compared to a low frequency while gaseous emboli behave in the opposite manner. The study reports surprisingly good results even though the approach suffers from several limitations. The acoustic pressures generated at the region of interest need to be equal for both frequencies which is difficult to achieve if we account for skull reflections, attenuation due to inhomogeneities, diffraction and propagation effects. In addition, the selected frequencies (2 and 2.5 MHz) are too close to each other to reach a significant difference between the responses at the two frequencies and attain by that sufficient sensitivity. As an example and according to theory, for an air bubble, the difference in scattering cross section is less than 1 dB when the frequency increases from 2 MHz to 2.5 MHz. For a solid embolus of the same size and according to the Rayleigh theory, this difference is only of 3.8 dB. This simple calculation demonstrates that the sensitivity is a critical issue for this approach to discriminate between solid and gaseous emboli. All these studies have demonstrated the difficulties to develop a robust method to classify and to a less extent size emboli. TCD represents a powerful instrument for the detection of emboli but improvements concerning both an automated detection and classification with a sufficient sensitivity and specificity need to be carried out.

1.4 Clinical applications

Large differences in the recorded rate of MES have been noticed among the results obtained in several studies dealing with the same clinical aspect. This discordance can be imputed to different TCD monitoring time period as well as to technical parameters that can strongly influence the characteristics of the recorded embolic signals[44]. Due to these different interpretations, the clinical significance of embolic signals could remain uncertain[74]. Nevertheless, several studies have pointed out the clinical value of MES detection in various domains. For instance, MES monitoring during coronary bypass were directly correlated to a decline of cognitive functions[10] and the positive effect of carotid endarterectomy in preventing stroke was established for patients with high grade carotid stenosis[76,77]. TCD monitoring was also successfully used to demonstrate the effectiveness of antiplatelet and antithrombotic therapy[78]. The clinical significance of each type of embolus (gaseous or solid) is relatively speculative because there is no reliable technique to distinguish between gaseous and particulate matter. However, there is circumstantial evidence that particulate emboli are potentially far more damaging than gaseous emboli[75]. A reliable detection and characterization technique may have a number of important clinical implications: monitoring during surgery may help to prevent the formation of microemboli and therefore make the procedure safer, especially during cardiac and carotid surgery. The determination of the nature of an embolus will make possible to specifically determine which lesion is implicated when embolic signals are detected in patients with several possible causes of embolism. It may also improve the identification of patients at high or low risk of embolism and will help to evaluate drug treatment efficiency.

1.5 Outline of the thesis

The aim of this thesis was to investigate a new method to detect, characterize and size microemboli. We know that gas microbubbles, under specific US exposure conditions, can scatter energy at harmonic frequencies, subharmonic frequencies and ultraharmonic frequencies. These nonlinear scattering properties are specific to gaseous emboli and cannot be related to solid emboli. This difference between solid and gaseous microemboli in their nonlinear scattering properties is of significant relevance and thus can be utilized as a parameter to characterize them. In order to validate this approach in a controlled environment, a 'bubble maker' was developed to generate a stream of uniform microbubbles and is described in details in Chapter 2. The generated microbubbles have a diameter ranging from $10\,\mu$m to $200\,\mu$m and their number and precise size can be controlled independently. A visual observation of the dynamics of gaseous microemboli under ultrasonic insonification may help to validate the theory on which the classification method is based.

In Chapter 3, ultrafast optical recordings of the interaction between a gas bubble and ultrasound are presented. These optical recordings demonstrate the dependency of the nonlinear behavior of the gaseous emboli on the ultrasound exposure settings. They also appear as a valuable tool to estimate the performance of the theoretical model to predict the oscillations of a gaseous emboli induced by an ultrasound pulse. To evaluate the performances of the new emboli classification technique, acoustic scattering properties of gaseous emboli of various diameters and excited at different ultrasound settings are measured in an in vitro setup. The results are given in Chapters 4 and 5. In Chapter 4, we focused on higher harmonic components generation as a tool to detect and classify emboli. To enlarge the range of the detectable gaseous emboli, we investigated in Chapter 5 the generation of subharmonic and ultraharmonics as a function of gaseous emboli size. The currently available technology has limited performance in the low frequency range. Therefore, new transducers are needed in order to apply our approach. Two transducer designs for emboli classification are proposed in Chapter 6. The design of these transducers is based on separate transmitting and receiving technology. The first transducer is capable to classify only a limited range of emboli sizes. To widen the classifiable size range, the first design was improved using a multifrequency transducer. Both transducers were evaluated in a controlled in vitro environment.

In Chapter 7, the focus is directed towards elucidating the mechanical influence of the ultrasound beam on gas microemboli. Fast recordings were carried out and demonstrated a strong radiation on microemboli depending on their initial radiation size and the ultrasonic parameters. The experimental data were compared to a theoretical model and confirmed that such strong radiation forces may lead to erroneous readings of the Doppler emboli signals.

References

1. D. Georgiadis, D. Grosset, A. Kelman, A. Faichney, and K.R. Lees, "Prevalence and characteristics of intracranial microemboli signals in patients with different types of prosthetic cardiac valves", *Stroke* vol. 25, no. 11: pp. 587-592, 1994.

2. B.A. Hills and B.D. Butler, "Size distribution of intravascular air emboli produced by decompression", *Undersea Biomed Res*, vol. 8, no. 3: pp. 163-170, 1981.

3. I. Gersh, "Bubbles in bone and associated structures, lung and spleen of guinea pigs decompressed rapidly from high pressure atmospheres", *J Cell Comp Physiol*, vol. 26: pp. 101-117, 1945.

4. M.F. Newman, J.L. Kirchner, B. Phillips-Bute, V. Gaver, H. Grocott, R.H. Jones, D.B. Mark, J.G. Reves and J.A. Blumenthal, "Longitudinal assessment of neurocognitive function after coronary artery bypass surgery", *New Engl J Med*, vol. 344, no. 6: pp. 395-402, 2001.

5. J.M. Murkin, D.L. Baird, J.S. Martzke, S.J. Adams, and P. Lo, "Long-term neurological and neuropsychological outcome 3 years after coronary artery bypass surgery", *Anesth Analg*, vol. 82: pp. S328, 1996.

6. P.J. Shaw, D. Bates, N.E.F. Cartlidge, J.M. French, D. Heaviside, D.G. Julian, and D.A. Shaw, "Neurologic and neuropsychological morbidity following major surgery: comparison of coronary artery bypass and peripheral vascular surgery", *Stroke*, vol. 18, no. 4: pp. 700-707, 1987.

7. W. Pugsley, L. Klinger, C. Paschalis, T. Treasure, M. Harrison, and S. Newman, "The impact of microemboli during cardiopulmonary bypass on neuropsychological functioning", *Stroke*, vol. 25, no. 7: pp. 1393-1399, 1994.

8. W.G. Austen and D.H. Howry, "Ultrasound as a method to detect bubbles or particulate matter in the arterial line during cardiopulmonary bypass", *J Surg Res*, vol. 5, no. 6: pp. 283-284, 1965.

9. G.W. Roach, M. Kanchuger, C.M. Mangano, M.F. Newman, N. Nussmeier, R. Wolman, A. Aggarwal, K. Marschall, S.H. Graham, C. Ley, G. Ozanne, and D.T. Mangano, "Adverse cerebral outcomes after coronary bypass surgery", *New Engl J Med*, vol. 335, no. 25: pp. 1857-1863, 1998.

10. O.A. Selnes, M.A. Goldsborough, L.M. Borowicz, and G.M. McKhann, "Neurobehavioural sequelae of cardiopulmonary bypass", *The Lancet*, vol. 353, no. 9164: pp. 1601-1606, 1999.

11. N.L. Mills and J.L. Ochsner, "Massive air embolism during cardiopulmonary bypass. Causes, prevention and management", *J Thorac Cardiovasc Surg*, vol. 80, no. 5: pp. 708-717, 1980.

12. E.G. Gallagher and D.T. Pearson, "Ultrasonic identification of sources of gaseous microemboli during open heart surgery", *Thorax*, vol. 28, no. 3: pp. 295-305, 1973.

13. A.K. Kaza, J.T. Cope, and S.M. Fiser, "Elimination of fat microemboli during cardiopulmonary bypass", *Ann Thorax Surg*, vol. 75, no. 2: pp. 555-559, 2003.

14. S.K. Braekken, D. Russell, R. Brucher, M. Abdelnoor, and J.L. Svennivig, "Cerebral microembolic signals during cardiopulmonary bypass surgery: Frequency, time of occurrence and association with patient and surgical characteristics", *Stroke*, vol. 28, no. 10: pp. 1988-1992, 1997.

15. J. Van der Linden and H. Casimir-Ahn, "When do cerebral emboli appear during open heart operations?", *Ann Thorax Surg*, vol. 51, no. 2: pp. 237-241, 1991.

16. R.G.A. Ackerstaff, C. Jansen, and F.L. Moll, "Carotid endarterectomy and intraoperative emboli detection", *Echocardiography*, vol. 13, no. 5: pp. 543-550, 1996.

17. M.P. Spencer, "Transcranial Doppler monitoring and causes of stroke from carotid endarterectomy", *Stroke*, vol. 28, no. 4: pp. 685-691, 1997.

18. S.M. Siebler,G. Rose, D. Bendfeldt,H. Steinmetz, "Silent cerebral embolism caused by neurological symptomatic high grade carotid stenosis. Event rates before and after carotid endarterectomy", *Brain*, vol. 116, no. 5: pp. 1005-1015, 1993.

19. V.L. Babikian, C. Hyde, V. Pochay, and M.R. Winter, "Clinical correlates of high intensity transient signals detected on Transcranial Doppler sonography in patients with cerebrovascular disease", *Stroke*, vol. 25, no. 8: pp. 1570-1573, 1994.

20. A.M. Forteza, V.L. Babikian, C. Hyde, M.R. Winter, and V. Pochay, "Effect of time and cerebrovascular symptoms on the prevalence of microembolic signals in patients with cervical carotid stenosis", *Stroke*, vol. 27, no. 4: pp. 687-690, 1996.

21. S.K. Braekken, D. Russell, R. Brucher, and J.L. Svennivig, "Incidence and frequency of cerebral embolic signals in patients with a similar bileaflet mechanical heart valve", *Stroke*, vol. 26, no. 7: pp. 1225-1230, 1995.

22. D. Grosset, P. Cowburn,D. Georgiadis, H.J. Dargie, A. Faichney, and K.R. Lees, "Ultrasound detection of cerebral emboli in patient with prosthetic heart valves", *J Heart Valve Dis*, vol. 3, no. 2: pp. 128-132, 1994.

23. D. Milano, A. D'Alfonso, R. Codecasa, M. De Carlo, C. Nardi, G. Orlandi, L. Landucci, and U. Bortolotti, "Prospective evaluation of frequency and nature of Transcranial high-intensity Doppler signals in prosthetic valve recipients", *J Heart Valve Dis*, vol. 8, no.: pp. 488-494, 1999.

24. H.S. Markus, A. Loh, D.Israel, T. Buckenham, A. Clifton, and M.M. Brown, "Microscopic air embolism during cerebral angiography and strategies for its avoidance", *The Lancet*, vol. 341, no. 8848: pp. 784-787, 1993.

25. A.Dagirnanjian, D.A. Davis, W.E. Rothfus, Z.L. Deeb, and A.L. Goldberg, "Silent cerebral microemboli occurring during carotid angiography: Frequency as determined with doppler sonography", *Am J of Roentgenol*, vol. 161, no. 5: pp. 1037-1040, 1993.

26. H.S. Markus, A. Clifton, T. Buckenham, and M.M. Brown, "Carotid angioplasty: Detection of embolic signals during and after procedure", *Stroke*, vol. 25, no. 12: pp. 2403-2406, 1994.

27. G. Orlandi, S. Fanucchi, C. Fioretti, G. Acerbi, M. Puglioli, R. Padolecchia, F. Sartucci, and L. Murri, "Characteristics of cerebral microembolism during carotid stenting and angioplasty alone", *Arch Neurol*, vol. 58, no. 9: pp. 1410-1413, 2001.

28. F. Crawley, J. Stygall, S. Lunn, M. Harrison, M.M. Brown, and S. Newman, "Comparison of microembolism detected by Transcranial Doppler and neuropsychological sequelae of carotid surgery and percutaneous transluminal angioplasty", *Stroke*, vol. 31, no. 6: pp. 1329-1334, 2000.
29. C.H. Tegeler, L.P. Hitchings, M. Eicke, J. Leighton, R.K. Fredericks, T.R. Downes, D.A. Stump, and G.L. Burke, "Microemboli detection in stroke associated with atrial fibrillation", *J Cardiovascul Tech*, vol. 9, no.: pp. 283-284, 1990.
30. M.P. Spencer, S.D. Campbell, J.L. Sealey, F.C. Henry, and J. Lindberg, "Experiments on decompression bubbles in the circulation using ultrasonic and electromagnetic flowmeter", *J Occup Med*, vol. 11, no. 5: pp. 238-244, 1969.
31. A.M. Forteza, S. Koch, J.G. Romano, G. Zych, I.C. Bustillo, R.C. Duncan, and B. V.L., "Transcranial Doppler detection of fat emboli", *Stroke*, vol. 30, no. 3: pp. 2687-2691, 1999.
32. Z.G. Nadareishvili, Z. Choudary, C. Joyner, D. Brodie, and J.W. Norris, "Cerebral microembolism in acute myocardial infarction", *Stroke*, vol. 30, no. 12: pp. 2679-2682, 1999.
33. D.W. Droste, K. Silling, J. Stypmann, M. Grude, V. Kemeny, T. Wichter, K. Khune, and E.B. Ringelstein, "Contrast Transcranial Doppler ultrasound in the detection of right-to-left shunts: time window and threshold in microbubbles number", *Stroke*, vol. 31, no. 7: pp. 1640-1645, 2000.
34. J.G. Romano, A.M. Forteza, M. Concha, S. Koch, R.C. Heros, J.J. Morcos, and V.L. Babikian, "Detection of microemboli by Transcranial Doppler ultrasonography in aneurysmal subarachnoid hemorrhage", *Neurosurgery*, vol. 50, no. 5: pp. 1026-1031, 2002.
35. D.W. Droste, M.A. Ritter, G. Monnig, V. Kemeny, G. Breithardt, and E.B. Ringelstein, "Abundance of microembolic signals detected by Transcranial Doppler ultrasound in a patient with Einsenmenger's syndrome", *Cerebrovasc Dis*, vol. 9, no. 6: pp. 334-336, 1999.
36. D.W. Droste, R. Schlossberg, R. Mitusch, and M. Kaps, "Low frequency of clinically silent circulating emboli in patient with mitral valve prolapse or patent foreman ovale detected by bigated Transcranial Doppler ultrasound", *Neurol Res*, vol. 20, no. 6: pp. 499-503, 1998.
37. D. Georgiadis, A. Lindner, M. Manz, M. Sonntag, P. Zunker, H.R. Zerkowski, and M. Borggrefe, "Intracranial microembolic signals in 500 patients with potential cardiac or carotid embolic source and in normal controls", *Stroke*, vol. 28, no. 6: pp. 1203-1207, 1997.

38. D.G. Nabavi, D. Georgiadis, C. Schmid, T.G. Mackay, H.H. Scheld, and E.B. Ringelstein, "Clinical relevance of intracranial microembolic signals in patients with left ventricular assist devices. a prospective study", *Stroke*, vol. 27, no. 5: pp. 891-896, 1996.

39. M. Eicke, J. Klein, G.S. Werner, and W. Paulus, "Ongoing cerebral microembolism in patients with bacterial endocarditis", *J Neuroimaging*, vol. 7: pp. 232, 1997.

40. M. Sitzer, D. Sohngen, and M. Siebler, "Cerebral microembolism in patient with Sneddon's syndrome", *Arch Neurol*, vol. 52, no. 3: pp. 271-275, 1995.

41. M. Spencer, S. Campbell, J. Sealey, F. Henry, and J. Lindenbergh, "Experiments on decompression bubbles in the circulation using ultrasonic and electromagnetic flowmeters", *J Occup Med*, vol. 11, no. 5: pp. 238-244, 1969.

42. M.P. Spencer, "Detection of cerebral arterial emboli", *Transcranial Doppler*, edited by D.W. Newell and R. Aaslid: pp. 215-230, 1992.

43. M.A. Moehring and J.R. Klepper, "Pulse Doppler ultrasound detection, characterization and size estimation of emboli in flowing blood", *IEEE Trans Biomed Eng*, vol. 41, no. 1: pp. 35-44, 1994.

44. D.W. Droste, H.S. Markus, and M.M. Brown, "The effect of different settings of ultrasound pulse amplitude, gain and sample volume on the appearance of emboli studied in a Transcranial Doppler mode", *Cerebrovasc Dis*, vol. 4 (Suppl 3): pp. 152-156, 1994.

45. V. Kemeny, D. Droste, S. Hermes, D. Nabavi, Schulte-Altedorneburg, M. Siebler, and B. Ringelstein, "Automatic embolus detection by a neural network", *Stroke*, vol. 30, no. 4: pp. 807-810, 1999.

46. M. Siebler, G. Rose, M. Sitzer, A. Bender, and H. Steinmetz, "Real-time identification of cerebral microemboli with US feature detection by a neural network", *Radiology*, vol. 192, no. 3: pp. 739-742, 1994.

47. E.V. van Zuilen, W.H. Mess, C. Jansen, I. van der Twell, J. van Gijn, and R.G.A. Ackerstaff, "Automatic embolus detection compared with human experts", *Stroke*, vol. 27, no. 10: pp. 1840-1843, 1996.

48. H.S. Markus, M. Cullinane, and G. Reid, "Improved automated detection of embolic signals using a novel frequency filtering approach", *Stroke*, vol. 30, no. 8: pp. 1610-1615, 1999.

49. H. Markus and G. Reid, "Frequency filtering improves ultrasonic embolic signal detection", *Ultrasound Med Biol*, vol. 25, no. 5: pp. 857-860, 1999.

50. M. Cullinane, Z. Kaposzta, S. Reihill, and H.S. Markus, "Online automated detection of cerebral embolic signals from a variety of embolic sources", *Ultrasound Med Biol*, vol. 28, no. 10: pp. 1271-1277, 2002.

51. M. Cullinane, G. Reid, R. Dittrich, Z. Kaposzta, R.G.A. Ackerstaff, V. Babikian, D.W. Droste, D. Grosset, M. Siebler, L. Valton, and H.S. Markus, "Evaluation of new online automated embolic signal detection algorithm including comparison with panel of international experts", *Stroke*, vol. 31, no. 6: pp. 1335-1341, 2000.

52. L. Fan, D. Evans, and A. Naylor, "Automated embolus identification using a rule-based expert system", *Ultrasound Med Biol*, vol. 27, no. 8: pp. 1065-1077, 2001.

53. N. Aydin, S. Padayache, and H.S. Markus, "The use of the wavelet transform to describe embolic signals", *Ultrasound Med Biol*, vol. 25, no. 6: pp. 953-958, 1999.

54. G. Devuyst, J.M. Vesin, P.A. Despland, and J. Bogousslavsky, "The matching pursuit: a new method for characterizing microembolic signal?", *Ultrasound Med Biol*, vol. 26, no. 6: pp. 1051-1056, 2000.

55. L. Fan and D.H. Evans, "Extracting instantaneous mean frequency information from Doppler signals using the Wigner distribution function", *Ultrasound Med Biol*, vol. 20, no. 5: pp. 429-443, 1994.

56. J.L. Smith, D.H. Evans, L. Fan, A.J. Thrush, and A.R. Naylor, "Processing Doppler ultrasound signals from blood-borne emboli", *Ultrasound Med Biol*, vol. 20, no. 5: pp. 455-462, 1994.

57. R.W.M. Keunen, C.J. Stam, D.L.J. Tavy, W.H. Mess, B.M. Titulaer, and R.G.A. Ackerstaff, "Preliminary report of detecting microembolic signals in Transcranial Doppler time series with nonlinear forecasting", *Stroke*, vol. 29, no. 8: pp. 1638-1643, 1998.

58. F. Ries, K. Teimann, C. Pohl, C. Bauer, M. Mundo, and H. Becher, "High resolution emboli detection and differentiation by characteristic postembolic spectral patterns", *Stroke*, vol. 29, no. 3: pp. 668-672, 1998.

59. E. Roy, P. Abraham, S. Montresor, M. Baudry, and J. Saumet, "The narrow band hypothesis: an interesting approach for high intensity transient signals (HITS) detection", *Ultrasound Med Biol*, vol. 34, no. 3: pp. 375-382, 1998.

60. J. Girault, D. Kouame, A. Ouahabi, and F. Patat, "Microemboli detection: an ultrasound Doppler signal processing viewpoint", *IEEE Trans Biom Eng*, vol. 47, no. 11: pp. 1431-1439, 2000.

61. J.L. Smith, D.H. Evans, L. Fan, P.R.F. Bell, and A.R. Naylor, "Differentiation between emboli and artefacts using dual-gated Transcranial Doppler ultrasound", *Ultrasound Med Biol*, vol. 22, no. 8: pp. 1031-1036, 1996.

62. D. Georgiadis, J. Goeke, M. Hill, D. Nabavi, F. Stogbauer, P. Zunker, and E. Ringelstein, "A novel technique for identification of Doppler microembolic signals based on the coincidence method", *Stroke*, vol. 27, no. 4: pp. 683-686, 1996.

63. D. Georgiadis, A. Wenzel, H. Zerkowski, S. Zierz, and A. Lindner, "Automated intraoperative detection of Doppler microemboli signals using the bigate approach", *Stroke*, vol. 29, no. 1: pp. 137-139, 1998.

64. W.H. Mess, M. Titulaer, and G.A. Ackerstaff, "A new algorithm for off-line automated emboli detection based on the pseudo-wigner power distribution and the dual gate TCD technique", *Ultrasound Med Biol*, vol. 26, no. 3: pp. 413-418, 2000.

65. J.L. Smith, D.H. Evans, and A.R. Naylor, "Signals from dual gated TCD systems: curious observations and possible explanations", *Ultrasound Med Biol*, vol. 23, no. 1: pp. 15-24, 1997.

66. J. Molloy and H.S. Markus, "Multigated Doppler ultrasound in the detection of emboli in a flow model and emboli signals in patients", *Stroke*, vol. 27, no. 9: pp. 1548-1552, 1996.

67. D. Russell and R. Brucher, "Online automatic discrimination between solid and gaseous cerebral microemboli with the first multifrequency Transcranial Doppler", *Stroke*, vol. 33, no. 8: pp. 1975-1980, 2002.

68. G. Devuyst, G.A. Darbellay, J.M. Vesin, V. Kemeny, M. Ritter, D.W. Droste, C. Moline, J. Serena, R. Sztajzel, P. Ruchat, C. Lucchesi, G. Dietler, E.B. Ringelstein, P.A. Despland, and J. Bogousslavsky, "Automatic classification of HITS into artifacts or solid or gaseous emboli by a wavelet representation combined with dual gated TCD", *Stroke*, vol. 32, no. 12: pp. 2803-2809, 2001.

69. H.S. Markus and M.M. Brown, "Differentiation between different pathological cerebral embolic materials using Transcranial Doppler in an *in vitro* model", *Stroke*, vol. 24, no. 1: pp. 1-5, 1993.

70. D. Russell, R. Brucher, K.P. Madden, W.M. Clark, P.M. Sandset, and J.A. Zivin, "The intensity of the Doppler signal caused by arterial emboli depends on embolus type and size", *Stroke*, vol. 23, no. 1: pp. 158, 1992.

71. J.L. Smith, D.H. Evans, P.R.F. Bell, and A.R. Naylor, “A comparison of four methods for distinguishing Doppler signals from gaseous and particulate emboli”, *Stroke*, vol. 29, no. 7: pp. 1133-1138, 1998.

72. D. Georgiadis, T.G. Mackay, A.W. Kelman, D.G. Grosset, D.J. Wheastley, and L. K.R., “Differentiation between gaseous and formed embolic materials In-Vivo: application in prosthetic heart valve patients”, *Stroke*, vol. 25, no. 8: pp. 1559-1563, 1994.

73. D.W. Droste, H.S. Markus, D. Nassiri, and M.M. Brown, “The effect of velocity on the appearance of embolic signals studied in Transcranial Doppler models”, *Stroke*, vol. 25, no. 5: pp. 986-991, 1994.

74. J.D. Easton, “Cerebral embolism and Doppler ultrasound”,*Cerebrovasc Dis*, vol. 9, no. 3: pp. 188-192, 1999.

75. M.E. Gaunt, P.J. Martin, S. J.L., T. Rimmer, G. Cherryman, D.A. Ratliff, P.R.F. Bell, and A.R. Naylor, “Clinical relevance of intraoperative embolization detected by Transcranial Doppler ultrasonography during carotid endarterectomy: a prospective study of 100 patients”, *Br J Surg.*, vol. 81, no. 10: pp. 1435-1439, 1994.

76. M. Siebler, M. Sitzer, G. Rose, D. Bendfeldt, and H. Steinmetz, “Silent cerebral embolism caused by neurological symptomatic high grade carotid stenosis. Event rates before and after carotid endarterectomy”, *Brain*, vol. 116, no. 5: pp. 1005-1015, 1993.

77. E.V. van Zuilen, F.L. Moll, F.E.E. Vermeulen, H.W. Mauser, J. van Gijn, and R.G.A. Ackerstaff, “Detection of cerebral microemboli by means of Transcranial Doppler monitoring before and after carotid endarterectomy”, *Stroke*, vol. 26, no. 2: pp. 210-213, 1995.

78. M. Goertler, M. Baeumer, R. Kross, T. Blaser, G. Lutze, S. Jost, and C.W. Wallesch, “Rapid decline of cerebral microemboli of arterial origin after intravenous acetylsalicylic acid”, *Stroke*, vol. 30, no. 1: pp. 66-69, 1999.

Chapter 2

Production of calibrated gaseous emboli

Abstract

For a better understanding of the immediate and long-term consequences of embolism, clinical investigations following the insertion of gaseous bubbles into the body as well as new detection methods need to be carried on. For that purpose, a device has been developed to generate a uniform stream of microbubbles with a diameter ranging between 20 μm and 300 μm. This device comprises a glass micropipette connected to an air pressure source. The micropipette tip crosses a variable liquid flow and the produced bubbles are carried away by the flow. These created bubbles have a very narrow size and density distribution: 90% of the bubbles lie within ±6% of the mean radius and the number of bubbles does not exceed a variation of 10% . The size and density of the produced bubbles can be controlled by adjusting three independent parameters: the liquid flow, the gas pressure level and the micropipette shape. For a given micropipette, increasing the liquid flow or decreasing the gas pressure level leads to a reduction of the bubbles size while the number of produced bubbles increases. As an example, a doubling of the liquid flow results in a variation of the bubble size up to 40%. This technique offers the advantage of generating uniform bubbles of known size and number depending on the settings selected and appears as a valuable tool for embolism studies.

Based on the publication: "Production of standardized air bubbles: application to embolism studies" by P. Palanchon, J. Klein and N. de Jong, *Review of Scientific Instruments*, vol. 74, no. 4: 2558-2564, 2003.

2.1 Introduction

The occurrence of gas bubbles into the intravascular and intracerebral circulation and its neurological or arterial repercussion is of great concern in several clinical procedures. Depending on the clinical situation, the nature of the emboli (gaseous or solid) and the number of embolic events can vary greatly. Hills and Butler[1] measured intravascular gaseous emboli ranging from 19 μm up to 700 μm following decompression in living dogs. Gersh[2] detected bubble sizes between 60 μm and 300 μm in both intravascular and extravascular sites. The number of embolic signals can also show wide variations. Georgiadis et al.[3] recorded between 0-620 embolic events per 30 minutes period for patients with prosthetic heart valves. M*ü*llges et al.[4] have observed between 0.53 and 59.05 embolic signals per minute during extracorporeal circulation in patient undergoing cardiac surgery. According to these results, the development of a device allowing the production of air bubbles of controllable size and density would be a valuable tool for embolism studies, either for clinical (consequences following the insertion of gas bubbles into the circulation) or technical (new ways for detection and characterization of microemboli) investigations.

Various methods have been proposed to generate gas bubbles. One approach is based on electrolysis. Although this technique allows the production of very small bubbles (Miller[5] was able to generate bubbles between 2 μm and 15 μm), the wide size distribution and the high number of bubbles limit significantly this method of production. Furthermore, the production of the bubbles is not easy to reproduce. A second approach is based on the gas injection principle and has been extensively studied theoretically and experimentally through different apparatus[6−13]. Hills and Butler[14], have developed a method to produce a stream of microbubbles with a narrow size distribution. Nitrogen was forced to pass through hypodermic needles to form bubbles. The bubbles produced ranged from 20 μm to 250 μm. More recently, following a similar principle, Gañán-Calvo and Gordillo[15] have described a nonlinear phenomenon based on microfluidic physics that allowed the production of air bubbles. Bubbles as small as 5 μm were created by using different physical parameters such as the orifice diameter, the liquid viscosity and the surface tension. These methods offer to the operator the possibility of producing a wide range of controllable bubble sizes but the number of bubbles produced remains quite high and cannot be adjusted by the operator.

This chapter presents a method to generate a stream of bubbles of known size and number. A homemade micropipette is submerged into a flowing liquid in a vertical tube. Gas is injected through the micropipette, allowing bubbles to escape from the micropipette tip and to be transported by the liquid flow. The gas pressure, micropipette shape and liquid flow can be adjusted to selectively produce bubble sizes ranging from 20 μm up to 300 μm.

2.2 Description of the device

The micropipettes were made of glass capillaries (Model GD 1, Narishige, Japan) with an outer diameter of 1 mm and an inner diameter of 0.6 mm. These tubes were placed in a pipette puller (Narishige, Japan). This instrument is designed to manufacture a variety of micropipettes through manual adjustments: the heating range and the weight, which is placed at the tip the tube. The variation of one of these parameters influences the shape and the diameter of the micropipette. Three parameters were measured: the inner diameter, the length and the contraction length in order to specify the micropipettes. Their definitions are given in Figure 2.1a.

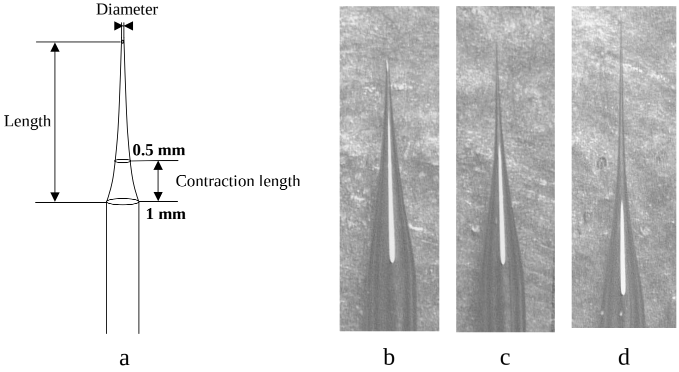

Figure 2.1: *a) Definitions of the micropipette dimensions, b),c) and d) micropipette shape of type I, type II and type III.*

Several trials have been performed to demonstrate the effect of the puller settings on the produced micropipette: an increase of the heater level resulted in an increase of the micropipette length while its diameter and its contraction length decreased. When the weight attached at the end of the micropipette increased, the length and the contraction length increased while the diameter decreased. Examples of the micropipette are displayed in Figures 2.1b, c and d for three different puller settings: heater 65/weight 30g (type I), heater 70/weigth 120g (type II) and heater 80/weigth 30g(type III). For each case, three micropipettes were made and their dimensions measured. The dimension variations are not greater than 3% for the micropipette length and 2% for the diameter while the contraction length remains identical. Indeed, the pipette puller assures a reproducible way to generate micropipettes of known dimensions.

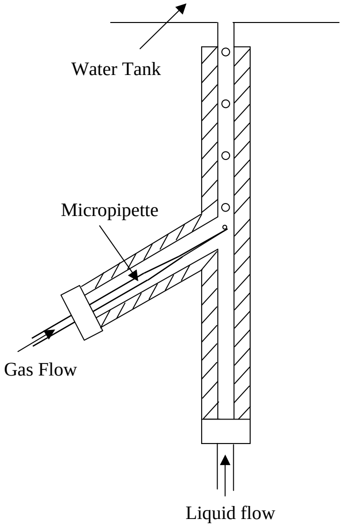

Figure 2.2: *Bubble maker drawing.*

A custom-made bubble generator was developed based on the gas injection principle. Figure 2.2 shows a drawing of the bubble maker. This device is composed of an Y-shaped Plexiglas tube. The main channel is oriented vertically and has an internal diameter of 0.75 mm. The second channel is oriented at an angle of 26 degrees vertically and has an internal diameter of 1.6 mm. A custom made micropipette is positioned inside the second tube and its tip positioned in the center of the main channel. A variable gas pressure source is connected to an electromechanical valve that controls the gas injection rate. Flowing gas passes through the micropipette and generates a bubble at the tip. Non-pulsative liquid flow generated by a gear pump cross the micropipette tip and carries the bubbles towards a water tank. For the current study, air was used and purified water was the surrounding liquid. To define the characteristics of the bubble patterns generated with the 'bubble maker', the bubble diameter and the bubble density number (expressed as the number of bubbles generated over a distance of 1 mm) were optically measured. The optical system is composed of a CCD camera (SONY) mounted on a long zoom microscope (Video Inspection System CC-97-VS2, Sciencescope, Chino, CA, USA). Several frames were saved on a PC for further analysis. The diameter of the bubble and the density number were computed using a MATLAB program (Matlab, Mathworks). The diameters of 30 bubbles were measured as well as the distance separating two successive bubbles. The optical system was positioned 7 cm above the micropipette tip. Since the main application of interest is to direct the bubbles towards an ultrasound device, we do not measure the bubble diameters when they are released from the tip of the micropipette. The size measurements was made so as to notice any possible difference in the bubble diameter at different locations in the water tank. However, no significant change was observed which can be explained by the fact that the time delay between the moment where the bubbles are created at the micropipette tip and the location where the bubbles are observed is short enough to keep the bubble diameter the same (dissolution effects are negligible). Measurement of the bubbles number density was carried out instead of the frequency production of the bubbles commonly used. This choice was motivated by the ultrasonic application. Here, studies dealing with the interaction between bubbles and an ultrasound field require a prior knowledge of the number of bubbles present in the ultrasound beam.

2.3 Bubble pattern characteristics

The pipette puller offers the possibility of creating a wide range of micropipettes. For this study, only three specific micropipettes were selected for further investigations of the parameters that affect the bubble characteristics. In the following section, some general comments will be made concerning any micropipettes and more specific remarks regarding the three selected micropipettes. These micropipettes were defined by the settings of the pipette puller [heater (weight)]: type I: 65(30 g); type II: 70(120 g); type III: 80(30 g), see Figure 2.1 and Table 2.1.

Micropipette	Length(mm)	Curvature(mm)	Diameter(μm)
type I	4.7	1.7	3.17
type II	4.38	1.91	2.4
type III	6.7	1.7	1

Table 2.1: *Dimensions of the micropipette type I, type II and type III.*

The technique proposed resulted in the formation of a stream of microbubbles highly uniform in size and spacing. Depending on the type of micropipette, the bubble pattern (diameter and density number) characteristics strongly differ. Figures 2.3a-c illustrate the different populations of bubbles that could be generated using micropipettes types I, II and III, using a liquid flow of 400 ml/h.

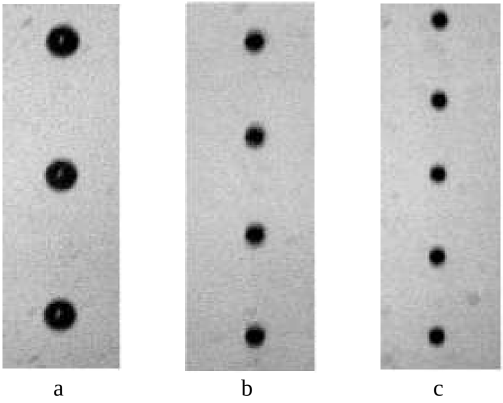

Figure 2.3: *Examples of the bubbles produced by the three selected micropipettes.*

The size distributions are displayed in Figure 2.4 for the three types of micropipettes at a selected liquid flow of 400 ml/h. The uniformity of the bubble diameter can be appreciated in Figures 2.4a-c and it appears to be dependent on the size of the produced bubbles: generation of the smallest bubbles (Figure 2.4a results in a very narrow size distribution: 100% of the bubbles lie within ±4 μm and 86% within ±2 μm. The bubbles produced by micropipette type I are much larger and their size distribution is somewhat wider: only 78% of the bubbles are less than ±4 μm and 70% less ±2 μm. The bubble's density number also exhibits a narrow distribution. Micropipettes types I, II and III produce, respectively, maximal density number variations of 8.2%, 6.7% and 12.3%. Overall, at any given flow and for any kind of micropipette, 90% of the bubbles have a diameter less than ±6% of their mean diameter while their density number does not exceed 10%. To test the reproducibility of the bubble generation process, we performed three different sets of experiments: (a) the bubble maker was run for 30 min and the size of the bubbles was checked every 5 min; (b) the system was stopped and run again every hour for a period of 4 hours. The measurements showed that the size and density distributions remain identical for these two sets of measurements. The last experiment (c) consisted of comparing the bubbles obtained from different micropipettes produced with the same pipette puller settings. As demonstrated in the previous section, the variation in the micropipette dimension was small when the same settings of the pipette puller was used. The bubble patterns for this

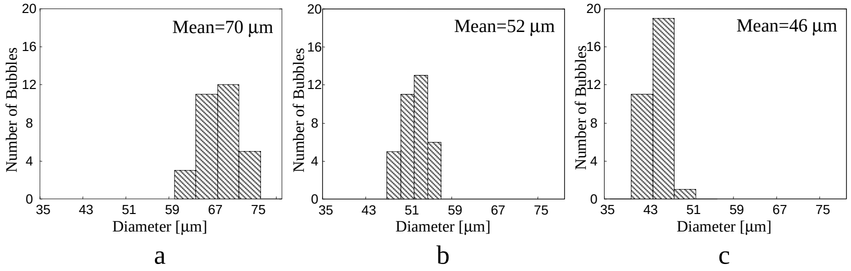

Figure 2.4: *Bubble size distributions for the three types of micropipettes: a) type I, b) type II, c) type III.*

configuration remained very similar. The mean diameter of the bubbles varies by $\pm 2\,\mu$m. The bubbles density number could reach a difference of 1.3 bubbles/mm.

Parameters affecting the bubble patterns

The incidence of different parameters on the bubble size and number was investigated experimentally. The physics behind the bubble formation process have not been studied since the main objective of this work was to generate bubbles and explore the capabilities of the bubble maker for an immediate application.

Gas pressure:

The release of microbubbles at the micropipette tip requires the use of a minimal gas pressure level. This threshold depends on the dimensions of the micropipette employed. For micropipettes type I, II and III, the minimal gas pressure required is 2.3 bars, 4 bars and 5 bars, respectively. Others examples of pressure threshold are displayed in Table 2.2. The gas source could deliver pressures between 1 bar and 7 bars. In some cases, higher pressures were required. Such micropipettes were discarded from this study.

The effects of the gas pressure on the bubble diameter were carried out by progressively increasing the gas pressure applied to the micropipette from 2.3 bars up to 6 bars. Micropipette type I was chosen since it has the lowest pressure threshold for bubble generation. Figure 2.5a presents the variation of the bubble size as a function of the gas pressure for a liquid flow of 400 ml/h. For a pressure between 2.3 bars and 5 bars, the bubble diameter increases linearly with the gas pressure. Typically, an increase of 20 μm is observed for a variation of (1 bar). At 6 bars, the relationship between the bubble size and the gas pressure is no longer linear. For pressures above 5 bars, the bubble size only increases very slightly. For higher pressures, the generated bubbles are nonuniform in size. The gas pressure is then too high for a stable rate of production. The influence of gas pressure on the variation of the density number is displayed in Figure 2.5b. The density number decreases linearly with the gas pressure up to 5 bars. A decrease of around 0.6 bubbles/mm was measured for variation of 1 bar in the gas pressure. For pressures higher than 5 bars, the density of the bubbles remains almost identical. A high level on non-uniformity in the density of the bubbles was also noticed for higher pressures.

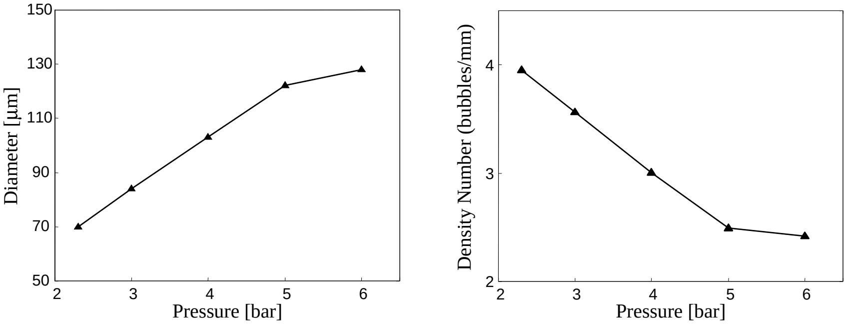

a

b

Figure 2.5: *a) Bubble size variations as a function of the air pressure; b) bubble density number variation as a function of the air pressure.*

In order to quantify the change in bubble pattern with the gas pressure, micropipette type II and III have also been studied. For both micropipettes and at a given liquid flow of 400 ml/h, the gas pressure was raised by 1.5 bars from the threshold of each micropipette. The variations in diameter and density number were measured following an increase in gas pressure. From these measurements it appears that the variation of either the bubble diameter or the density number is strongly dependent on the type of micropipette and cannot be theoretically predicted. Micropipette type II did yield to an increase of 9 μm in diameter while micropipette types I and III, respectively, showed an increase of 28 μm and 12 μm. The variations in bubble density number also depend on the type of micropipette. When the pressure is increased by 1.5 bars, the density number is reduced, respectively, by 0.9, 0.3 and 1.07 bubbles/mm for micropipettes types I, II and III. The changes in the bubble pattern (size and density) relative to the gas pressure cannot be predicted independently of the type of micropipette used.

In the current experimental set-up, if the operator wants to select the pressure as the main parameter by which to control the bubble diameter, the effects will be dominant for micropipettes that requires a low gas pressure threshold to generate bubbles. Thus, the gas pressure could be progressively increased up to a level at which disturbances start appearing.

Liquid flow:

The start of bubble generation occurs when the liquid flow is activated. For liquid flow smaller than 100 ml/h, the bubble diameter and density number tend to vary significantly. Bubble size varying for more than 30% has been observed. This effect may be explained by the fact that the liquid flow is not high enough to generate a stable rate of production. When the flow increases above this threshold the generation of bubbles is stabilized and characterized by a clear stream of bubbles (Figure 2.3). For high flow rates, the bubble size and density become progressively less uniform until the appearance of a cloud of bubbles. This upper limit of the liquid flow rate varies greatly depending on the micropipette used. As an example, the micropipette type I does not produce uniform bubbles when the liquid flow is higher than 450 ml/h whereas for type II and type III the liquid flow can be increased up to 800 ml/h and 1100 ml/h,respectively.

To study the effects of the liquid flow on the bubble size and density number, measurements were performed with a liquid rate varying from 150 ml/h to 650 ml/h. For micropipette type I, the liquid flow was kept below 400 ml/h. Figure 2.6a shows on a semilogarithmic scale the variation of the bubble diameter as a function of the liquid flow for the three types of micropipette studied. As we can observe, the bubble size decreases when the liquid flow becomes higher. This relationship can be approximated by an exponential curve independent of the type of micropipette. The best fit was obtained using

$$\phi(f) = A_1 \exp(-f/350) \tag{2.1}$$

where
ϕ is the bubble diameter in μm;
f is the liquid flow in ml/h;
A_1 is a constant in μm that depends on the type of micropipette.
For micropipettes types I, II and III, coefficient A_1 is, respectively, 260 μm, 170 μm and 130 μm.

With a single micropipette, a wide range of bubbles can be generated by increasing the liquid flow passing the micropipette tip. The micropipettes type I, II and III, respectively, produce bubbles between $20 - 112\,\mu$m, 45 – 115 μm and 70 – 226 μm. The exponential curve indicates that small variations in the liquid flow rate induce large variations in the size of the bubbles produced. For example, an increase of the flow rate from 160 ml/h to 220 ml/h causes a change in bubble size of 17%.

The change in the bubble density number as a function of the liquid flow is displayed in Figure 2.6b on a semilogarithmic scale. The bubble density number shows an exponential increase when the liquid flow increases. This also means that the production frequency of the bubbles increases with the liquid flow. Variation in the number of bubbles as function of the liquid flow is independent of the type of micropipette used and can be approximated by

$$n(f) = A_2 \exp(f/250) \tag{2.2}$$

where
n is the number of bubbles;
f is the liquid flow in ml/h;
A_2 is a constant depending on the micropipette.
For micropipette types I, II and III, the coefficient A_2 is, respectively, 0.5, 0.8 and 1.1.

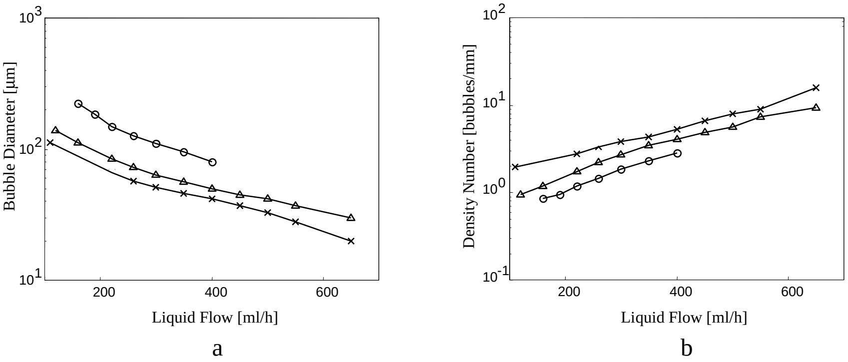

Figure 2.6: *a) Bubble size variations as a function of the liquid flow for three micropipettes: type I (O), type II (△) and type III (×); (b) bubble density number as a function of the liquid flow or three micropipettes: type I (O), type II (△) and type III (×).*

As the liquid flow increases, the density of the bubbles becomes higher. This property offers the possibility of generating bubbles of a fixed diameter but at different rate. Micropipette type III generates bubbles of 100 μm with a density number of 2.5 bubbles/mm. Micropipette type II can generate bubbles of the same size with a density number of 1.6 bubbles/mm.

Selecting adequate micropipettes, the bubble density can be controlled independently of the bubble diameter. For liquid flow higher than 650 ml/h, the empirical curves indicate that bubbles with diameters less than 20 μm are expected. However, for such flows, the optical system does not allow accurate measurements of the bubble size and density due to blurring motion. According to our estimates, bubbles as small as 10 μm could be produced by this method using the micropipette type III. The influence of the gas pressure level on the bubble pattern evolution with the liquid rate was also investigated. Figure 2.7 displays the variation of the bubble size and the density number versus the liquid flow for two different pressures 5 bars and 6.5 bars. The micropipette used here is type III. Both quantities decrease with the liquid flow according to the same exponential curve defined previously: Equation 2.1 for the bubble diameter and Equation 2.2 for the density number. Thus, the production of bubbles as a function of the liquid flow is independent on the applied gas pressure level used. Based on the results presented in this section, the size and the density of bubbles as a function of the liquid flow can be predicted using Equations 2.1 and 2.2 independently of the type of micropipette. The two constants, A_1 and A_2, have to be determined by performing a single measurement at any given flow.

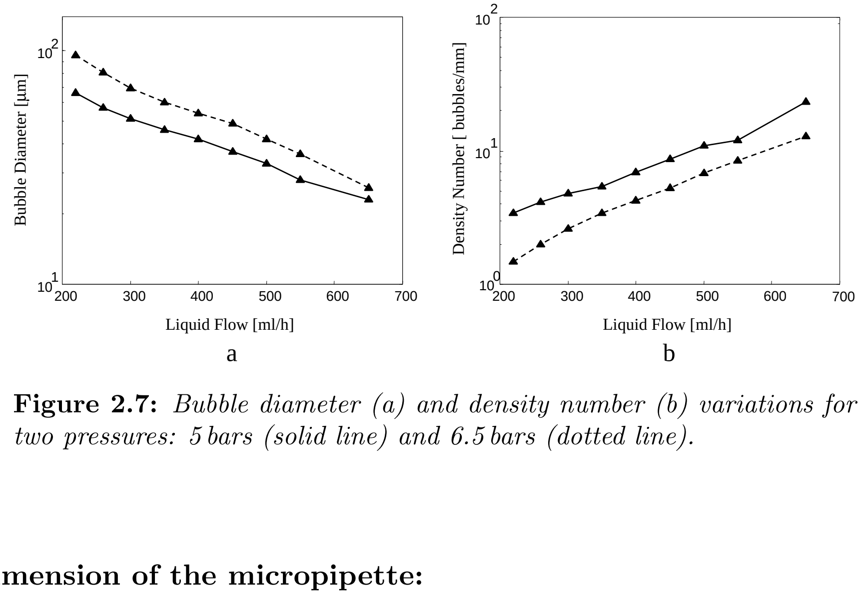

Figure 2.7: *Bubble diameter (a) and density number (b) variations for two pressures: 5 bars (solid line) and 6.5 bars (dotted line).*

Dimension of the micropipette:

The third parameter that influences the bubble production is the type of micropipette. Table 2.2 summarizes the results obtained for seven different micropipette configurations. Each micropipette is defined by the pipette puller settings (heater and weight). The minimal and maximal liquid flow rates used to generate bubbles are specified for each micropipette. Depending on the dimensions of the micropipette, the gas pressure required to generate bubbles and the range of bubble sizes produced vary significantly. The size of the bubbles is directly correlated to the diameter of the micropipette: the larger the diameter, the larger the bubbles. However, the gas pressure applied to the micropipette is also an important parameter. It has been demonstrated previously that the size of the bubble increases with the applied gas pressure and the gas pressure required to generate bubbles depends on the shape of the micropipette. Micropipettes with the smallest diameters do not necessary generate the smallest bubble size. As an example, we can compare the results obtained for micropipette type III with a new micropipette referred as micropipette type IV. This micropipette was obtained with a heater level of 80 and a weight of 60 g. Its dimensions are: length 5.9 mm, curvature 1.5 mm and diameter 0.8 μm. For these two micropipettes, the minimal gas pressures required to generate bubbles are, respectively, 5 bars and 6.5 bars. Even though micropipette type IV has a smaller diameter than micropipette type III, it appears that the bubbles generated by the two pipettes are almost identical. At a flow rate of 400 ml/h, micropipette type IV produced bubbles of 44 μm diameter while micropipette type III yielded bubbles of 42 μm. This example illustrates the case in with the effect of the gas pressure on the bubble diameter cannot be compensated by a smaller tip.

The density of the produced bubbles cannot be assessed with regard to the type of micropipette used. It was only observed that larger diameters produced less dense populations, but no quantitative information could be extracted from the measurements. We considered the case of micropipette types III and IV. At a liquid rate of 400 ml/h, they produce almost identical bubble diameters but the number of bubbles differs. The density number is 7.4 bubbles/mm for micropipette type IV and 5.2 bubbles/mm for micropipette type III. Therefore, the shape of the micropipette can strongly affect the number of bubbles produced while there is negligible effect on the bubble diameters.

From Table 2.2, we can appreciate the different bubbles' patterns. The diameters range from 20 μm up to 226 μm. Different micropipettes can produce the same bubble diameter at different liquid flows. If bubbles of 100 μm are required, five micropipettes can be selected: 75(60g), 70(120g), 70(30g) 65(30g) and 65(120g). A difference will appear for the level of bubble density. For these five micropipettes, the average density number is, respectively, $1.1, 1.4, 1.6, 2.2$ and 2.3 bubbles/mm.

Heater	Weight (g)	Pressure (Bar)	Liquid Flow (ml/h)	Bubble Size (μm)	Density Number (bubbles/mm)
80	1	5	110-640	112-20	1.9-15.8
80	30	6.5	160-600	30-91	2.94-11
75	60	5	120-400	52-140	0.7-3.4
70	30	3	160-400	59-152	1.3-4.5
70	120	4	120-640	30-140	0.95-9.25
65	30	2.3	160-400	70-226	0.85-2.83
65	120	2.8	160-400	61-162	1.5-5.2

Table 2.2: *Bubbles diameter and number and minimum gas pressure level for 8 types of micropipettes.*

2.4 Conclusions

This chapter presents a system to generate calibrated microbubbles of highly uniform size and density number distribution. The bubble size and its number can be individually controlled by varying different settings. The bubble maker possibilities could be improved by studying other parameters that affect the bubble patterns such as liquid viscosity or surface tension. According to previous works, reducing the viscosity of the liquid leads to a decrease in bubble size that should allow the production of extremely small microbubbles. Using this setup, we have produced air bubbles of different sizes to simulate gaseous emboli that occur in blood circulation by applying ultrasound at different frequencies and amplitudes. We have concluded that the nonlinear behavior of these gas bubbles is more suitable as a detection parameter than the fundamental oscillations as used in current emboli detection methods.

References

1. B.A. Hills and B.D. Butler, “Size distribution of intravascular air emboli produced by decompression”, *Undersea Biomed Res*, vol. 8, no. 3: pp. 163-170, 1981.

2. I. Gersh, “Bubbles in bone and associated structures, lung and spleen of guinea pigs decompressed rapidly from high pressure atmospheres”,

J Cell Comp Physiol, vol. 26: pp. 101-117, 1945.

3. D. Georgiadis, M. Kaps, M. Siebler, M. Hill, M. Konig, J. Berg, M. Kahl, P. Zumker, B. Diehl, and E.N. Ringelstein, "Variability of Doppler microembolic signal counts in patient with prosthetic cardiac valves", *Stroke*, vol. 26, no. 3: pp. 439-443, 1995.

4. W. Müllges, D. Franke, W. Reents, and J. Babib-Ebell, "Brain microembolic counts during extracorporeal circulation depend on aortic cannula position", *Ultrasound Med Biol*, vol. 27, no. 7: pp. 933.936, 2001.

5. D.L. Miller, "Ultrasonic detection of resonant cavitation bubbles in a flow tube by their second harmonic emissions", *Ultrasonics*, vol. 21, no. 5: pp. 217-224, 1981.

6. B.M. Jensenn, M. Ekker, A.O. Brubakk, and A. Sira, "Method for producing gas bubbles for use in air-embolism studies", *Med Biol Eng Comput*, vol. 29, no. 1: pp. 104-108, 1991.

7. M. Kameda and Y. Matsumoto, "Nonlinear oscillation of a spherical gas bubble in acoustic fields", *J Acoust Soc Am*, vol. 106, no. 6: pp. 3156-3166, 1999.

8. S. Ramakrishnan, R. Kumar, and N.R. Kuloor, "Studies in bubble formation: I- Bubbles formation under constant flow conditions", *Chem Eng Sci* , vol. 24, no.: pp. 731-474, 1969.

9. R.A.M. Al.-Hayes and R.H.S. Winterton, "Bubble diameter on detachment in flowing liquids", *Int J Heat Mass Transf*, vol. 24, no.: pp. 223-230, 1981.

10. H.N. Oguz and A. Prosperetti, "Dynamics of bubble growth and detachment from a needle", *J Fluid Mech*, vol. 257, no.: pp. 111-145, 1993.

11. C. Ohl, "Generator for single bubbles of controllable size", *Rev Sci Instrum*, vol. 72, no. 1: pp. 252-254, 2001.

12. R. Kumar and N.R. Kuloor, "The formation of bubbles and drops", *Adv Chem Engng*, vol. 8, no. 1: pp. 256-368, 1970.

13. D. Grukle, N. Marsh, and B. Hills, "Experimental air embolism: measurement of microbubbles using the coulter counter",*Br J Exp Path*, vol. 54, no. 6: pp. 684-691, 1973.

14. B. Hills and B. Butler, "A method of producing calibrated microbubbles for air embolism studies", *J Appl Physiol*, vol. 51, no. 2: pp. 524-528, 1981.

15. A. Gañán-Calvo and J. Gordillo, “Perfectly monodisperse microbubbling by capillary flow focusing”, *Phys Rev Lett*, vol. 87, no. 27: pp. 274501-1-274501-4, 2001.

Chapter 3

Modelling of gaseous microemboli in an ultrasound field

Abstract

The study of the bubble oscillations in an acoustic field is a fundamental subject to better understand physical phenomena such as acoustic cavitation or sonoluminescence. Many studies have been conducted to develop a theoretical model that describes the radial motion of the bubble radius. These models have been widely investigated numerically or analytically and have brought fruitful informations about the bubble behavior. The aim of this study was to qualitatively and quantitatively compare the results obtained with optical recording of bubble vibrations and a theoretical model. The bubble oscillations were optically recorded using the high-speed digital camera, BRANDARIS. The radius-time R(t) curve is directly computed from 128 video frames with a high temporal and spatial resolution. Air bubbles with a resting diameter ranging from 26 µm up to 100 µm were used in the experiments. The ultrasound field consisted of an eight-cycle pulse at a frequency of 130 kHz generating an acoustic pressure between 10 kPa and 150 kPa. The time and the frequency response of the bubble radial motion were compared to the Keller model. The comparison between the experimental and the simulated time and frequency responses of the bubble shows globally a good agreement both qualitatively and quantitatively and for all the bubble sizes studied. The theoretical model correctly reproduced the nonlinear features of the bubble oscillations. The results showed that

---

Based on the publication: "Modelling and optical measurements of the acoustic behavior of air bubbles' by P. Palanchon, A. Bouakaz and N. de Jong. Submitted.

for low acoustic pressure levels, the amplitude of the bubble oscillations at the fundamental and second harmonic frequency is maximal for an air bubble with a resting radius of 24 µm, which corresponds to the theoretical resonance size. Bubbles above the resonance size require much higher acoustic pressure to oscillate nonlinearly. In addition, optical recordings showing an onset of the bubble shape also referred to surface mode oscillations, were also observed at pressures as low as 37 kPa. In conclusion, the Keller model can be used to accurately predict the fundamental and harmonic behavior of gaseous microemboli.

3.1 Introduction

Studying the oscillations of a bubble in an acoustic field is a fundamental subject for acoustic cavitation or sonoluminescence. The radius as a function of time $R(t)$ is the single variable involved in the description of the bubble dynamics. Since Lord Rayleigh[1], many studies have been devoted to the development of a theoretical model that describes the radial motion of the bubble radius[2–4]. These models have been widely investigated numerically or analytically and they have brought fruitful informations about the linear and nonlinear behavior of bubbles under ultrasound irradiation. Mainly, for low and moderate driving pressures, the bubble oscillations are periodic and the bubble shape remains spherically symmetric. Depending on the bubble initial radius and the transmitted frequency f_0, the frequency response will include, beyond the main resonance, some nonlinear harmonic components at $2f_0, 3f_0, etc$ as well as subharmonic $(f_0/2)$ and ultraharmonic $(3/2f_0, 5/2f_0, ...)$ components[5–9]. For higher acoustic pressure levels, the bubbles can undergo strong distortions from their initial spherical shape, named surface mode oscillations.

Experimental validation of the theory was mostly performed by indirect means such as the acoustic signal backscattered by the bubble rather than by a direct measurements of radius-time curves. Recently, few studies involving high-speed photography or laser technique have been conducted to determine the variation of the bubble radius as a function of the acoustic parameters, such as the transmitted frequency and the acoustic pressure. Holt and Crum[10] used light scattering method to measure the time-varying response of an oscillating levitated bubble with a initial radius ranging from 20 μm up to 90 μm. The $R(t)$ curve was computed from the light intensity scattered by the bubble. They compared the experimental results to a theoretical model derived by Prosperetti[4] and revealed a discrepancy between the theoretical and experimental responses mainly at the 2^{nd} harmonic frequency. For higher acoustic pressures, the appearance of subharmonic component over a wide range of bubble sizes was suspected to arise from shape oscillation modes. However this technique did not provide any information about the bubble shape, which could explain the difference with the theoretical value. Tian and colleagues[11] performed optical recordings of the oscillations of a single bubble, using a high speed camera with a frame rate of 16.7 ms and ultrasound pulse at 16.3 kHz. Due to the low frame rate, direct observations of the bubble pulsations were limited but the system was used to detect onset of the bubble shape. However, no comparison to any theoretical model was carried out. More recently, Kameda[12] investigated the nonlinear oscillations of a gas bubble in the range of 100 μm and 250 μm in a pressure field with a frequency of 20 kHz.

The Radius-Time (RT) curves were constructed from the successive optical pictures (obtained at a frame rate of 10 ms) and compared to a theoretical model including the effect of the thermo-fluid mechanics of the gas inside the bubble.

This chapter presents an experimental and numerical investigation of the dynamics of a single air bubble in an ultrasound field. The primary aim of the study was to qualitatively and quantitatively compare the results of a theoretical model to optical recordings. The purpose of such a comparison is to validate the performances of the theoretical model in describing the acoustic behavior of gaseous microemboli. The bubbles investigated in this study had initial diameters ranging from 26 μm up to 100 μm, which corresponds roughly to the size of clinically encountered microemboli. The bubble oscillations were optically recorded using a high speed digital camera. The radius-time curves were computed from a total of 128 successive video frames, which gives a total exposure time long enough to study rigorously the bubble dynamics. The time and the frequency responses of the bubble radial motion were compared to the model developed by Keller[3]. Depending on the bubble initial size and the applied acoustic pressure, some bubbles were undergoing shape distortions and thus lost their spherical symmetry. These bubbles were discarded from the comparison study since they did not satisfy the model's assumptions. The appearance of these different surface modes (from mode 2 up to mode 5) is reported in the last section of the chapter.

3.2 Theoretical model

Since Rayleigh[1], many studies have been carried out to develop a theoretical model to describe the oscillations of gas bubbles. In this thesis, we selected the modified Keller equation[3], derived from the Rayleigh-Plesset-Noltingk-Neppiras (RPPN) equation to describe the dynamic behavior of a free gas bubble. The main difference with the RPPN model is in considering the medium as slightly compressible.

The validity of this model is based on the following assumptions:

a) The bubble is surrounded by a compressible fluid of infinite extent with a constant viscosity.
b) The bubble radial motion remains spherically symmetric during its oscillations.
c) There is no rectified diffusion during the ultrasound exposure time.
d) The wavelength is assumed to be much larger than the bubble diameter and only the motion of the bubble surface is

d) The wavelength is assumed to be much larger than the bubble diameter and only the motion of the bubble surface is of interest.

e) The vapor pressure and the polytropic exponent remain constant during the expansion and contraction phases.

The expression of the differential equation of motion of the bubble radius is given by:

$$(1-\frac{\dot{R(t)}}{c})\ddot{R(t)}R(t)+\frac{3}{2}\dot{R(t)}^{2}(1-\frac{\dot{R(t)}}{3c}) = (1+\frac{\dot{R(t)}}{c})\frac{P(t)}{\rho}+\frac{R(t)}{\rho c}\dot{P(t)} \tag{3.1}$$

$$P(t) = (P_{ST}-P_V+\frac{2\sigma}{R_0})(\frac{R_0}{R(t)})^{3\kappa}-\frac{2\sigma}{R(t)}-\delta_t\omega\rho R(t)\dot{R(t)}-P_{ST}+P_V-P_{AC}(t) \tag{3.2}$$

where

$R(t)$ is the instantaneous radius;

$\dot{R}(t)$ is the first time derivative of the instantaneous radius = velocity;

$\ddot{R}(t)$ is the second time derivative of the instantaneous radius = acceleration;

R_0 is the equilibrium radius;

ω is the angular frequency;

c is the sound velocity;

ρ is the density of the surrounding medium;

σ is the surface tension;

P_{ST} is the static pressure (ambient pressure);

δ_t is the total damping coefficient,

P_V is the vapor pressure,

κ is the polytropic exponent,

$P_{AC}(t)$ is the time varying excitation acoustic pressure.

The total damping coefficient is defined as the sum of the damping constants due to the radiation (δ_{rad}), the viscosity of the surrounding medium (δ_{vis}) and the thermal conductivity (δ_{th}). Their expressions were given by Medwin[13]

$$\delta_{tot} = \delta_{rad} + \delta_{vis} + \delta_{th} \tag{3.3}$$

μ is the viscosity of the surrounding medium;
k is the wave number $(2\pi/\lambda)$;
f_R is the resonance frequency of the bubble;
$d/b = 3(\gamma - 1)$ where γ is the ratio of the heat capacity at constant pressure and constant volume.

The bubble resonance frequency was computed using the formula given by Medwin[13]:

$$f_r^2 = \frac{1}{2\pi R_0}\sqrt{\frac{3\gamma b\sigma P_0}{\rho}} \tag{3.7}$$

where
P_0 is the acoustic pressure level;
b=1/κ, κ is the polytropic exponent.

The expression of the effective mass, the polytropic exponent and the surface tension are given by Medwin[13]. Equation 3.1 was solved using the fourth order Runge-Kutta method implemented using Matlab Simulink (Matlab, Mathworks). A fixed step size was used. For the simulations, the initial values at $t = 0$ are $R = R_0$ and $\dot{R}$=0.

3.3 Experimental setup

The experimental setup is shown in Figure 3.1. An electrical gated signal was generated by an arbitrary waveform generator. The electrical signal was amplified by a 50 dB linear power amplifier (2100L, ENI, NY, USA), and its amplitude could be adjusted by a separate attenuator from 0 to 120 dB in steps of 1 dB (355C/D, HP, Palo Alto, CA). The peak negative acoustic pressures were measured separately using a calibrated hydrophone (Reson GmbH, Kiel, Germany). The amplified electrical signal was then directed to an unfocused single element transducer (Matec Instrument Companies Inc, Northborough, USA). The transducer had a center frequency of 130 kHz and a total aperture of 31 mm. The transducer was mounted in a water tank and positioned in such a way to produce acoustic waves directed perpendicularly to the bubble streamline, as shown in Figure 3.2. The bubbles (represented by a needle on the drawing) are located 4 cm away from the transducer surface. A microscope (BXM microscope, Olympus, the Netherlands) was positioned perpendicularly to the water tank, and projected images of the gaseous bubbles with a magnification of 20 times on the digital camera. The optical observations were made using an ultra-fast digital camera, named BRANDARIS. The camera has a time resolution of 40 ns (25 million frames per second) and can store up to 128 frames in every shot. With such a system real-time optical observations of the bubble oscillations are possible with a very high temporal and

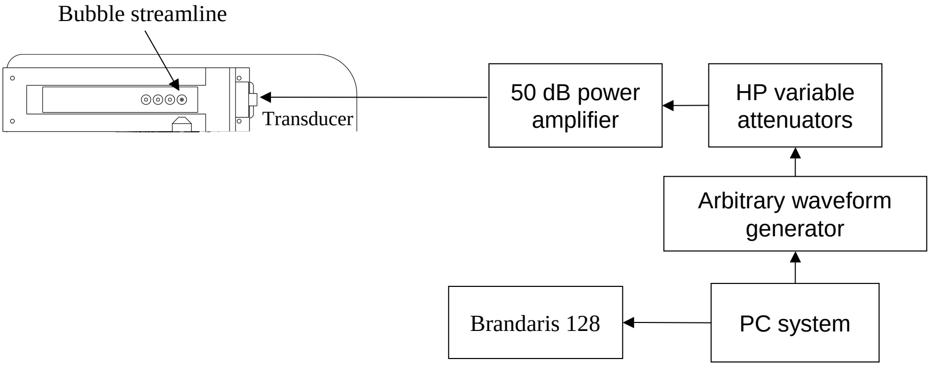

Figure 3.1: *Top view of the experimental setup.*

spatial resolution. More detailed technical description of the camera and its working principle can be found in the website www.brandaris128.nl or in the publication by Chin et al[14]. The transmitted acoustic signal consisted of a burst of 8 cycles at 130 kHz center frequency giving thus a total ultrasound scanning duration of approximately 46 μs. The optical frame rate used ranged from 1.1 MHz to 1.25 MHz corresponding to an optical scanning duration between 102.4 μs and 116.4 μs for a total of 128 frames. Therefore, the total optical observation was always longer than the ultrasound exposure. The first frames of every optical recording were always positioned before ultrasound insonification starts, so that the initial bubble size could be estimated. Typically, 5 frames were recorded before ultrasound was launched. To observe the behavior of the microbubbles at different amplitudes, the acoustic pressure at the location of the bubbles was varied. The acoustic pressure used in these experiments ranged from 10 kPa up to 150 kPa. The acoustic lateral beam profile of the transducer as measured at 4 cm for 130 kHz transmit frequency and had a beam width at -6dB of 20 mm. Over mm distance (corresponding to vertical frame dimension), we can assume that the bubble is submitted to identical pressure level independently of its position within the field of view of the optical system. Bubbles with different sizes were generated with the ‘bubble maker’. Deliberately, sizes below, above and at resonance were selected and used to

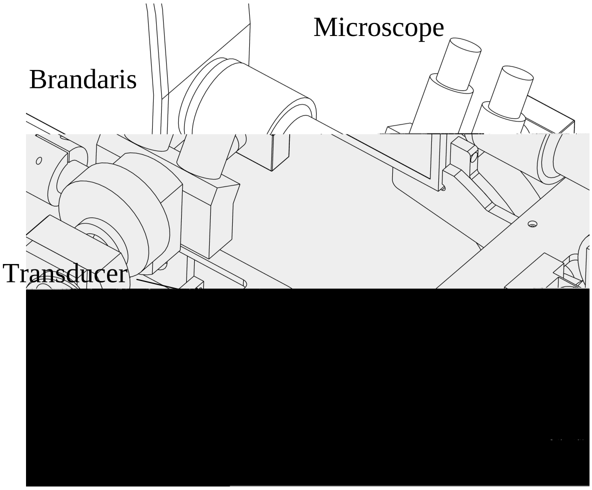

Figure 3.2: *Optical arrangement.*

validate the theoretical model for predicting microemboli interaction with ultrasound.

3.4 Results and discussions

The diameter of the bubble is computed from the 128 frames for a given recording and a radius time $R(t)$ curve is then constructed. The size of the bubble is calculated by detecting the bubble contour using an algorithm based on a Minimum Cost Analysis function. Figure 3.3 illustrates an example of the bubble oscillations. Few optical images of the bubbles at different stages are shown on top of the acoustic pressure wave. The bubble has an initial radius of 48 μm and the applied acoustic peak pressure was 20 kPa. We can clearly appreciate the expansion and contraction phases of the bubbles according to the pressure variations. The largest diameter is obtained when the pressure wave reaches its rarefaction value while the smallest diameter appears for the highest level of the pressure wave. The bubble oscillations were firstly investigated as a function of the resting diameter of the bubble. The amplitude of the bubble oscillations is given by the quantity $(R_{max} - R_{min})/R_0$ and was measured for different bubble sizes undergoing identical ultrasonic scanning conditions. The acoustic field is defined by a 8 cycles burst transmitting a frequency of 130 kHz and generating an acoustic pressure of 20 kPa at the bubble location. The equilibrium bubble diameter extended from 26 μm up to 60 μm.

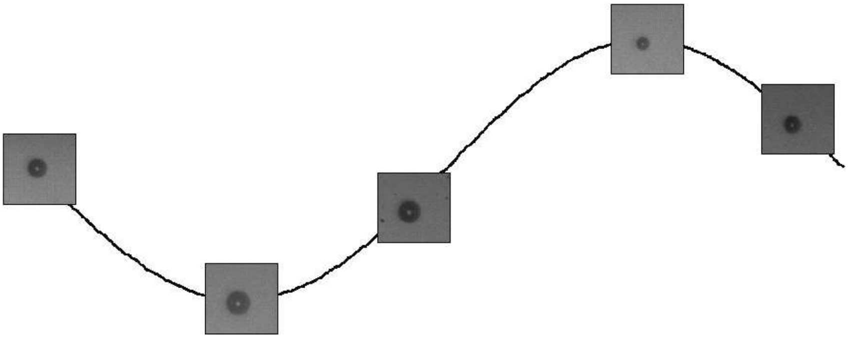

Figure 3.3: *Bubble oscillations as a function of the pressure waveform.*

Figure 3.4a presents the bubble oscillations at the fundamental frequency (130 kHz) while Figure 3.4b displays the bubble oscillations at the second harmonic frequency (260 kHz). The oscillation amplitude at the fundamental frequency exhibits a maximum when the bubble has a resting diameter of 48 μm. This diameter corresponds to the theoretical resonance size as estimated from the formula of Medwin given in Equation 3.7. For bubbles with a diameter away from the resonance, the amplitude of the bubble oscillations decreases quite rapidly. However, the decay rate of the oscillations is more pronounced for bubbles above resonance size. For bubbles around half the resonance size, the oscillations amplitude decreases more than 50% from its maximal value while the same decay rate is achieved for

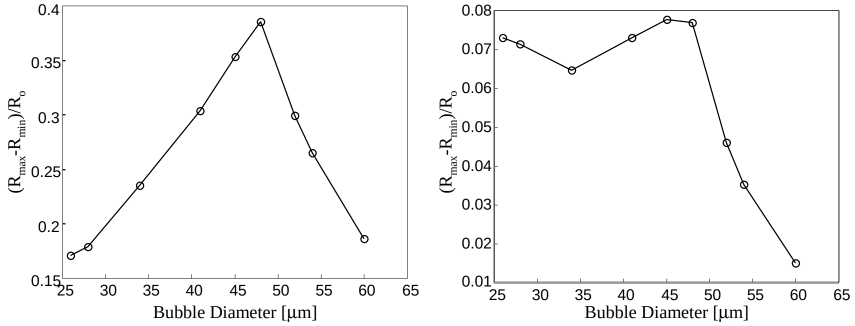

a b

Figure 3.4: *(Measured $R_{max} - R_{min})/R_0$ as a function of the bubble diameter: a) at the fundamental frequency; b) at the second harmonic frequency.*

bubbles that are only 25% above the resonance size. The bubble oscillations at the second harmonic frequency show a different behavior than at the fundamental frequency. The maximal oscillations amplitude is also obtained for bubbles at resonance. Bubbles larger than resonance size show a rapid decay of their vibrations. Bubbles 25% above the resonance size have their amplitude oscillation decreased by 80% compared to the maximal amplitude. However, bubbles smaller than the resonance size behave differently. The amplitude oscillations decays for bubbles slightly smaller than resonance (down to 34 μm), with a slow decay rate. For smaller bubble that are closer to half the resonance size, in this particular case 24 μm, the oscillations at the second harmonic become larger again. The maximal oscillation value is obtained for a 26 μm bubble, which is very close to half the resonance. Unfortunately, we were not able to produce smaller bubbles to investigate their behavior, but the tendency of the curve already confirms the theory that bubbles at half the resonance behave more nonlinearly than bubbles above the resonance. Furthermore, both curves have validated the theoretical expression of the resonance frequency.

The experimental $R(t)$ curves were compared to the theoretical solutions computed from Equation 3.1 for specific bubble diameters. Air bubbles with an initial diameter of 26 μm (near half the resonance), 41 μm (below resonance), 48 μm (at resonance), 54 μm (above resonance) and 97 μm (twice the resonance size) were explored. The acoustic burst contained eight-cycles at a center frequency of 130 kHz and emitting a pressure of 20 kPa at the bubble location.

Figure 3.5 to Figure 3.9 present the experimental (dotted line) and simulated (solid line) results. Each figure displays the diameter-time ($D(t)$) curves and the corresponding frequency spectra normalized to their maximal value at the fundamental frequency. Figure 3.5 presents the results obtained for a bubble with an initial diameter of 26 μm. According to the resonance frequency formula, such a bubble is very close to half the resonance size (24 μm). We can clearly notice, in the frequency spectrum, a strong second harmonic at 260 kHz and a third harmonic at 390 kHz in the frequency spectrum. The simulated results, given by solid lines, exhibit diameter oscillations 4% smaller compared to the experimental measurements. Furthermore, the measured frequency spectra, especially at the fundamental and the second harmonic frequency are in good agreement with the theoretical predictions, while the third harmonic is smaller than expected. Nevertheless, globally, the measured nonlinear features of the $D(t)$ curve are satisfactorily reproduced.

Figure 3.6 presents the oscillations of a bubble with an initial diameter of 34 μm. As noticed previously, the simulated maximal oscillations of the bubbles are smaller than the experimental ones but overall a good correla-

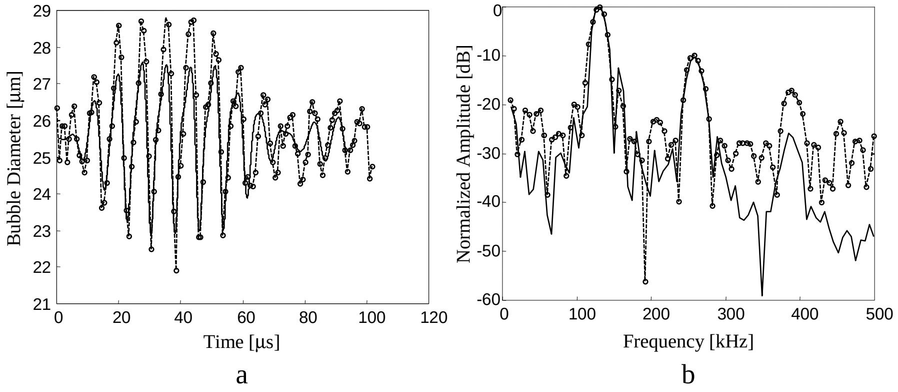

Figure 3.5: *Simulated (solid line) and measured (dotted line) D(t) curves (a) and frequency spectrum (b) of a bubble with a resting diameter of 26 µm insonified at 130 kHz and 20 kPa.*

tion is obtained. The frequency spectra also show a good agreement. It can also be noticed that a 34 μm bubble exhibits a lower number of nonlinear components than the 26 μm bubble. Figure 3.7 compares the theoretical predictions with the measurements for a resonant bubble of 48 μm. The simulated results show slightly larger values than the experimental data but the difference is smaller than 10%. However, the theoretical frequency response perfectly reproduces, both quantitatively and qualitatively, the experimental linear and nonlinear behavior of resonant bubbles. The results obtained with a bubble of 54 μm are shown in Figure 3.8. The experimental $D(t)$ curve and the frequency spectrum are reproduced by the simulations. The amplitude oscillations are lower than resonant bubble and this feature is characterized by a lower number of harmonic components in the frequency spectrum: only a small second harmonic 22 dB below the fundamental is generated by this bubble.

Figure 3.9 shows the $D(t)$ curve and the frequency response of a bubble with a resting diameter of 93 μm, which is very close to twice the resonance size (96 μm). For this particular configuration, the bubble was insonified with a larger acoustic pressure level in order to induce the bubble into nonlinear motion. The pressure level was 150 kPa. The $D(t)$ curves measured and simulated are in good agreement during the first eight cycles of the oscillations. Afterwards, the measurements show that the bubble continues oscillating while the theoretical model exhibit a damping in the oscillations. The oscillations correspond to surface mode oscillations as observed on the optical recording. Therefore, the frequency response was

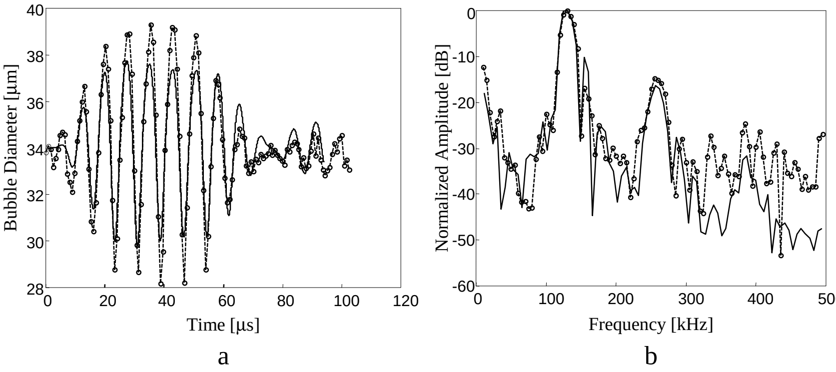

Figure 3.6: *Simulated (solid line) and measured (dotted line) D(t) curves (a) and frequency spectrum (b) of a bubble with a resting diameter of 34 μm insonified at 130 kHz and 20 kPa.*

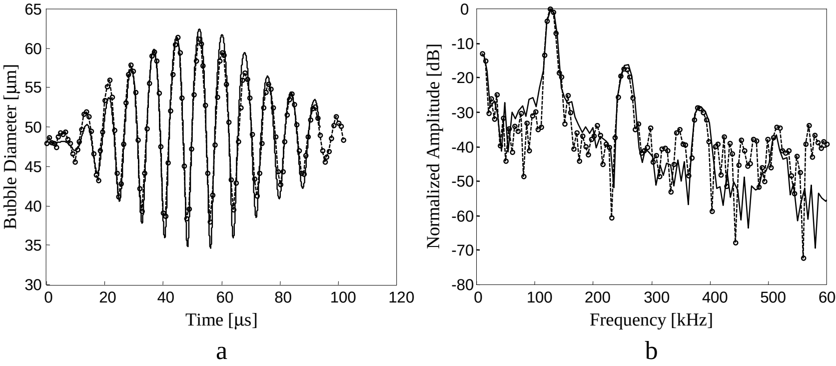

Figure 3.7: *Simulated (solid line) and measured (dotted line) D(t) curves (a) and frequency spectrum (b) of a bubble with a resting diameter of 48 μm insonified at 130 kHz and 20 kPa.*

computed from the $D(t)$ curve corresponding to volume mode oscillations while the end of the curve was discarded. The frequency spectra exhibit a strong second harmonic and a subharmonic components. The theoretical second harmonic agrees with the measurements while there is a discrepancy concerning the subharmonic frequency. Overall, the theoretical model developed by Keller gives a good agreement with the optical recordings of the bubble oscillations.

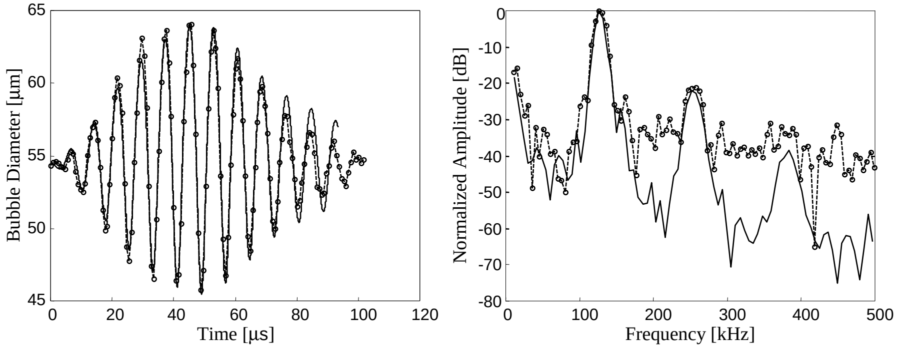

a b

Figure 3.8: *Simulated (solid line) and measured (dotted line) D(t) curves (a) and frequency spectrum (b) of a bubble with a resting diameter of 54 μm insonified at 130 kHz and 20 kPa.*

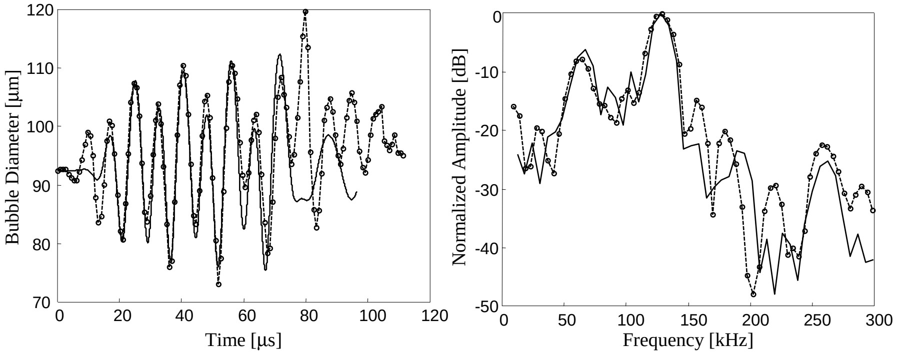

a b

Figure 3.9: *Simulated (solid line) and measured (dotted line) D(t) curves (a) and frequency spectrum (b) of a bubble with a resting diameter of 93 μm insonified at 130 kHz and 20 kPa.*

First observations of surface modes

The previous results were obtained with applied acoustic pressures low enough to allow the bubble shape to remain unchanged during its pulsations and to oscillate volumetrically. Nevertheless, depending on the bubble size, the bubble oscillations can take various shapes, known as surface mode vibrations. The change in shape can be described as the superimposition upon a sphere a spherical harmonic of different mode n, with

$n = 2, 3, 4, ...$ The case n=0 corresponds to the oscillations of the bubble volume and it is called volume mode. Further details about the mode as well as a review of the surface mode studies are given by Leighton[15].

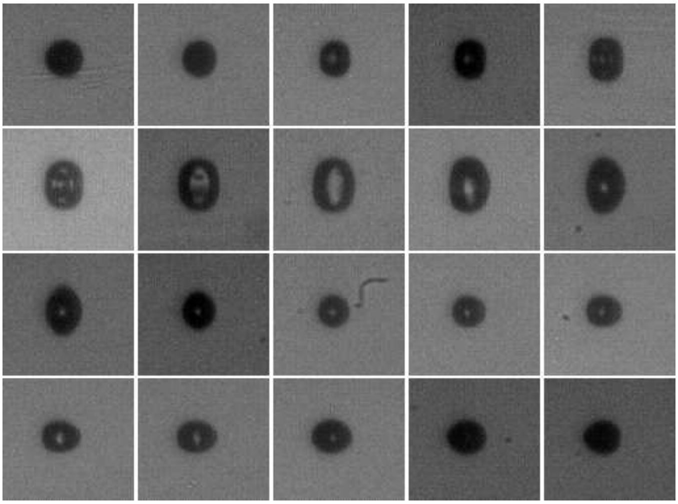

Figure 3.10: *Bubble with a resting diameter of 44 μm undergoing surface mode 2 (transmitted acoustic pressure 37 kPa, f_0=130kHz).*

When insonified at a fixed frequency, free bubble undergoes different surface mode oscillations depending on its diameter. During our investigations, surface modes ranging from mode 2 to mode 5 were observed and they are presented in Figures 3.10 to 3.13. Each figure displays a complete cycle of the surface mode oscillations. Figure 3.10 shows mode 2 surface oscillations. The bubble has an initial diameter of 44 μm and the transmitted acoustic pressure was 37 kPa. We can clearly appreciate the vertical expansion during the growing phase of the oscillation and the horizontal expansion during the contraction phase. Figure 3.11 displays the surface mode 3 generated by a bubble diameter of 54 μm with an acoustic pressure of 37 kPa while Figure 3.12 displays the surface mode 4 for a bubble diameter of 81 μm and an acoustic pressure of 120 kPa. Figure 3.13 shows the illustration of the surface mode 5, obtained for a 96 μm resting diameter bubble and using a transmitted acoustic pressure of 150 kPa. In the last row of the figure, we can notice that for such a high acoustic pressure, the bubble shape distortions are so strong that the bubble breaks and a small bubble is appearing next to the initial bubble. For each case presented, the frequency of the surface mode oscillations was 65 kHz, which corresponds to half the transmitted frequency. This validates previous studies which have

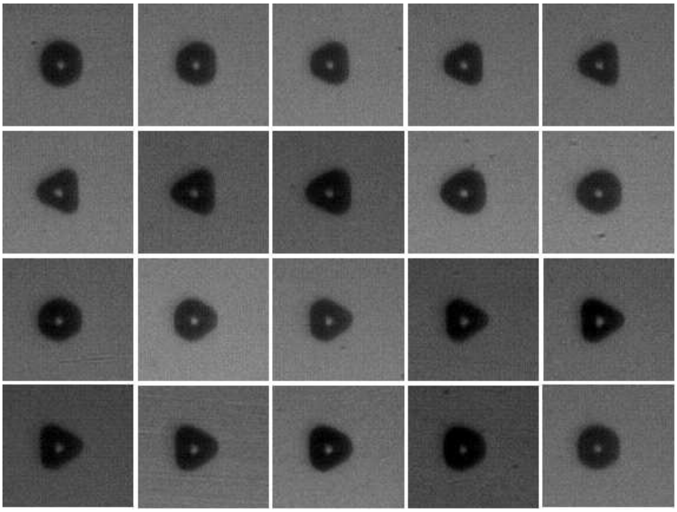

Figure 3.11: *Bubble with an resting diameter of 54 μm undergoing surface mode 3 (transmitted acoustic pressure 37 kPa, f_0=130kHz).*

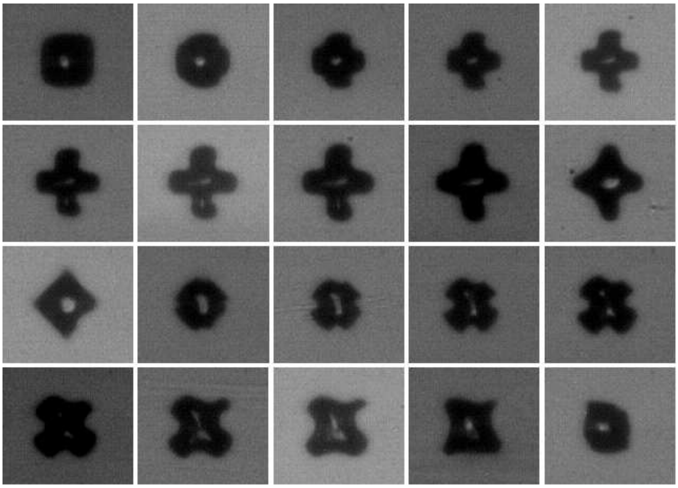

Figure 3.12: *Bubble with an resting diameter of 81 μm undergoing surface mode 4 (transmitted acoustic pressure 120 kPa, f_0=130kHz).*

reported that bubble undergoing surface mode generated a subharmonic component. Further investigations of the surface mode production need to

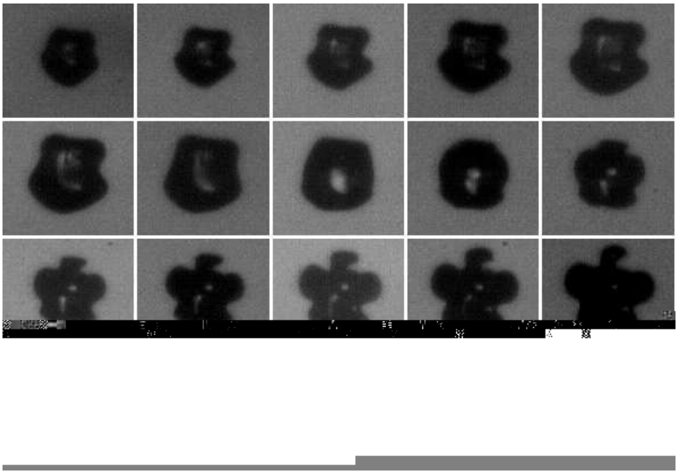

Figure 3.13: *Bubble with an resting diameter of 93 μm undergoing surface mode 5 (transmitted acoustic pressure 150 kPa, f_0=130kHz).*

be carried out in order to better understand its physical characteristics.

3.5 Conclusions

This chapter describes a numerical and experimental investigation of the oscillations of a single air bubble in response to an acoustic field. The optical system allows the recording of the bubble radial motion over a period of time longer than the ultrasound exposure. Therefore, the optical data represent a good basis to perform a quantitative and qualitative comparison with the theory. The study of the oscillations as a function of the bubble size reveals a maximum for a bubble diameter of 48 μm corresponding to the theoretical resonance size. The amplitude of the oscillations at the second harmonic demonstrates that bubble around half the resonance size generates a high number of nonlinear components as suggested by the theory. The experimental data were compared to the theoretical model developed by Keller. There is a good qualitative and quantitative agreement between both, not only for the $R(t)$ curves but also for the frequency response. The most important discrepancy occurs for the frequency response of a bubble around twice the resonance size. Overall, this study demonstrates the usefulness of the Keller model to predict the behavior of the bubbles and its use for emboli studies.

References

1. L. Rayleigh, "On the pressure developed in a liquid during collapse of a spherical cavity", *Philos Mag*, vol. 34, no. 200: pp. 94, 1917.

2. B.E. Noltingk and E.A. Neppiras, "Cavitation produced by ultrasonics", *Proc Phys Soc B*, vol. 63, no. 9: pp. 674-685., 1950.

3. J.B. Keller and M. Miksis, "Bubble oscillations of large amplitude", *J Acoust Soc Am*, vol. 68, no. 2: pp. 628-633, 1980.

4. A. Prosperetti, L.A. Crum, and K.W. Commander, "Nonlinear bubble dynamics", *J Acoust Soc Am*, vol. 83, no. 2: pp. 502-514, 1988.

5. E.A. Neppiras, "Subharmonic and other low frequency emissions from bubbles in sound-irradiated liquids", *J Acoust Soc Am*, vol. 46, no.: pp. 587-601, 1968.

6. B.C. Eatock and R.Y. Nishi, "Numerical studies of the spectrum of low intensity ultrasound scattered by bubbles", *J Acoust Soc Am*, vol. 77, no. 5: pp. 1692-1701, 1985.

7. A. Francescutto and R. Nabergoj, "Steady state oscillations of gas bubbles in liquids: explicit formulas for frequency response curves", *J Acoust Soc Am*, vol. 73, no. 2: pp. 457-460, 1983.

8. W. Lauterborn, "Numerical investigation of nonlinear oscillations of gas bubbles in liquids", *J Acoust Soc Am*, vol. 59, no. 2: pp. 283-293, 1976.

9. A. Prosperetti, "Nonlinear oscillations of gas bubbles in liquids: steady state solutions", *J Acoust Soc Am*, vol. 56, no. 3: pp. 878-885, 1974.

10. R.G. Holt and L.A. Crum, "Acoustically forced oscillations of air bubbles in water: Experimental results", *J Acoust Soc Am*, vol. 91, no. 4: pp. 1924-1932, 1996.

11. Y. Tian, J.A. Ketterling, and R.E. Apfel, "Direct observation of microbubble oscillations", *J Acoust Soc Am*, vol. 100, no. 6: pp. 3976-3978, 1996.

12. M. Kameda and Y. Matsumoto, "Non linear oscillation of a spherical gas bubble in acoustic fields", *J Acoust Soc Am*, vol. 106, no. 6: pp. 3156-3166, 1999.

13. H. Medwin, "Counting bubbles acoustically: a review", *Ultrasonics*, vol. 15, no. 1: pp. 7-13, 1977.

14. C.T. Chin, C. Lancée, J. Borsboom, F. Mastik, M.E. Frijlink, N. de Jong, M. Versluis, and D. Lhose, “Brandaris 128: A digital 25 million frames per second camera with 128 highly sensitive frames”, *Rev Sci Instrum*, vol. 74, no. 12: pp. 5026-5034, 2003.

15. T.G. Leighton, “The Acoustic Bubble”, London Academic Press Limited, 1994.

Chapter 4

Harmonic emission of gas bubbles applied to microemboli detection

Abstract

In this chapter, a new technique based on the nonlinear oscillations of gas bubbles is applied to gaseous emboli detection, characterization and sizing. To simulate gaseous emboli, the experimental "bubble maker" described in Chapter 2 was used to produce air bubbles of uniform diameters ranging from 19 μm up to 200 μm. The ultrasonic set-up consisted of low frequency transducers operating at 130 kHz and 250 kHz and using low acoustic pressures (30 kPa and 55 kPa). The theoretical model evaluated in Chapter 3 is used for comparison. Both experimental and theoretical results showed that depending on the transmitted frequency and the bubbles' sizes, higher harmonic components were produced in the frequency spectrum of the scattered echo. Non-resonating bubbles scatter either linearly when their sizes are far away from the resonance size or nonlinearly at the second or third harmonic frequency when their sizes become close to the resonance size. Only resonant bubbles or bubbles very close to the resonance size are able to scatter at higher harmonic frequencies (fourth and fifth). This property

---

Based on the publication: "New technique for emboli detection and discrimination based on nonlinear characteristics of gas bubbles" by P. Palanchon, A. Bouakaz, J.H. van Blankestein, J. Klein, N. Bom and N. de Jong, *Ultrasound in Medicine and Biology*, vol. 27, no. 6: pp. 801-808, 2001.

is used to discriminate between resonating bubbles from other bubble sizes. The appearance of harmonic component in the frequency spectrum appears as a valuable tool to differentiate gaseous emboli from solid emboli that scatter only linearly.

4.1 Introduction

Several ultrasonic methods have been utilized for microemboli detection. The most widely used is the Doppler. The ability of Doppler ultrasound to detect emboli circulating in the blood stream was first described in the sixties[1,2]. When a moving particle (solid or gaseous) is passing through the Doppler sample volume, the impedance mismatch between the embolus and the surrounding medium leads to an increase in the received Doppler signal. Such signals are defined as short duration, high intensity signals (HITS). Several *in vitro* and *in vivo* studies[3–6] have been attempted to detect emboli and differentiate between gaseous and formed-element emboli. Different parameters have been used for detection, such as the emboli velocity, the time duration and the relative intensity increase of the Doppler signal, expressed as the ratio of the maximal relative power amplitude when an embolus is present to the maximal relative power amplitude of the flowing blood without embolus. Such analysis of the Doppler signals can provide some information about embolus characteristics and size in well-controlled *in-vitro* experiments, but accurate characterization in clinical practice is not yet possible using current technology.

Ultrasonic methods based on ultrasound-bubble interaction may become an alternative approach for emboli detection. Theoretical descriptions and modelling of the interaction between ultrasound waves and gas bubbles have been investigated for many years[7]. Theory shows that, when an ultrasound wave with relatively low acoustic amplitude hits a gas bubble, the bubble starts pulsating with symmetric expansion and contraction phases. The vibrations are maximal when the transmitted frequency (f) is equal to the natural resonance frequency of the bubble. When the transmitted acoustic amplitude is increased, the bubble vibrations become asymmetric. This asymmetry is characterized by the appearance of harmonics ($2f, 3f$), subharmonic ($1/2f$) and ultraharmonic ($3/2f$, $5/2f$) components in the frequency spectrum of the scattered signal. This behavior was widely described in Chapter 3 with the help of optical recordings and theory.

Investigations of detection techniques based on bubble resonance[8,9] revealed that such a method was not ideal due to the fact that a signal of resonant bubbles can be similar, or even smaller than the signal of much larger (non-resonating) bubbles, which can lead to ambiguities in sizing bubbles. Miller[10,11] suggested the use of the second harmonic to detect resonant bubbles. His apparatus provided good results allowing discrimination between resonating and larger bubbles. Nevertheless, such a device was only sensitive to resonant bubbles, leaving non-resonant bubbles undetected. Eatock and Nishi[12] have studied numerically the possibility of detecting bubbles by the use of harmonics (second and third harmonic) and subharmonics at low acoustic pressures. They used transducers operating at 500 kHz and 1 MHz with amplitudes of 17 kPa and 54 kPa, and demonstrated that harmonic generation at low acoustic pressures required a driving frequency being within 10% of the resonance frequency of the bubble or a low integer fraction (1/2, 1/3) of the resonance frequency. These methods based on harmonic emissions are, however, accompanied by two main limitations: frequencies higher than 500 kHz were used, which correspond to resonating bubbles smaller than 12 μm in diameter. Therefore, larger bubbles (during decompression, bubble size was estimated to range from 20 μm to 200 μm[13]) could not be detected. Moreover, low acoustic pressures were required to obtain a good resolution in sizing the bubbles, meaning that only bubbles very close to the resonance size could scatter at the second harmonic frequency and, thus, could be detected. Consequently, these techniques appear sensitive only to very specific bubble, especially bubbles smaller than 12 μm, and so could not be exploited for emboli detection.

Newhouse and Shankar[14] have developed a technique to size the bubbles based on the double frequency method. Bubbles were simultaneously insonated with a constant high frequency called imaging frequency (w_i) and a lower variable frequency called pumping frequency (w_p). Bubbles oscillations become nonlinear when the pump frequency is close to the resonance frequency of the bubbles. Consequently, when the sum and difference frequency ($w_i \pm w_p$) exhibit a maximum, the value of the pumping frequency allow indirect estimation of the bubble's size. Leighton et al.[15] applied the same method by including the subharmonic emissions. The scattered signal at ($w_i \pm w_p/2$) appeared a more sensitive indicator to size bubbles than the signal at ($w_i \pm w_p$). Accurate bubble sizes were obtained but an acoustic pressure threshold was required to obtain a fine resolution and the signal could be correlated only to a single bubble. Furthermore, this method required a complex apparatus that may be quite difficult to adapt for *in vivo* microemboli detection.

The aim of the method proposed in this chapter, was to detect and characterize circulating gaseous emboli. The approach is based on the nonlinear scattering properties of gas bubbles. According to theory, a driving frequency near the natural resonance frequency of the bubbles with a sufficient acoustic amplitude will induce nonlinear vibrations and, therefore, lead to second and higher harmonic scattering. When the driving frequency is chosen to be far away from the resonance, harmonics are hardly generated. Consequently, bubble detection based on harmonic emissions requires the use of transducers operating at frequencies close to the resonance frequencies of the bubbles under investigation. The transducer frequencies used in this study (hundreds of kilohertz, which are low frequencies compared to usual frequencies used in medical diagnostic applications) were selected to correspond to resonance sizes around 50 μm and 25 μm. Moreover, using low-frequency ultrasound waves minimizes considerably the harmonic generation due to nonlinear propagation effects. Therefore, the harmonic components in the frequency spectrum of the scattered signals can only be associated with nonlinear bubble vibrations and not with wave distortion. Solid emboli scatter linearly and their spectra exhibit a peak only at the transmitted fundamental frequency. By monitoring the harmonic emissions, gaseous emboli can be detected and discriminated from solid particles. Size estimation is performed were higher harmonic components (fourth or fifth harmonic) are generated.

4.2 Simulations

To study the dynamic behavior of the free gas bubble, a model developed by Keller is used as a theoretical basis. This model was extensively described in Chapter 3 and the reader can refer to this chapter for further details. To compare the simulations and the experimental results, we assumed that each bubble could be considered as an individual scatterer and that multiple scattering is negligible. Thus, the intensity of the scattered echo of N bubbles of similar size is given by the echo of one bubble multiplied by their number N[16]. It was also assumed that the flow velocity does not interfere on the bubble response (the Keller model was developed for a static bubble) since the flow velocity is low compared to the velocity of sound.

The predicted scattered echo from the bubbles is determined using a simplified relationship between the instantaneous radius of the bubble radius-time curve, $R(t)$, and the wall velocity, $\dot{R}(t)$. The radius-time curve is the solution of Equations 3.1 and 3.2 of the Keller model. When the assumption of a large oscillation amplitude is made but the Mach number is small, the echo is proportional to the time derivative of $R^2\dot{R}$ and is given by the following formula[17]:

$$E(t) = \frac{\rho}{z}(R(t)^2\ddot{R(t)} + 2R(t)\dot{R(t)}^2) \tag{4.1}$$

where z represents the distance between the bubble and the transducer.

In the simulations, the attenuation due to the propagation in the water path was included and then the scattered echo was bandpass filtered using the frequency response of the corresponding transmitting and receiving transducers, which were measured separately. The first simulations were run to better understand the behavior of the bubbles, depending on their size, the transmitted acoustic pressure and the emitted frequency.

For these simulations, the scattered echo was directly computed using Equation 5.1. Figure 4.1 presents the normalized spectra of the predicted echo from a single bubble with a diameter of 48 μm. The transmitted frequency was 130 kHz (natural resonance frequency of the bubble) and different acoustic pressures were used: 30 kPa, 15 kPa and 7.5 kPa. The figure illustrates the influence of the acoustic pressure on the generation of harmonics. At low pressure (7.5 kPa) only few harmonics are present in the scattered spectrum, while increasing the acoustic pressure, harmonic components increase in number and amplitude.

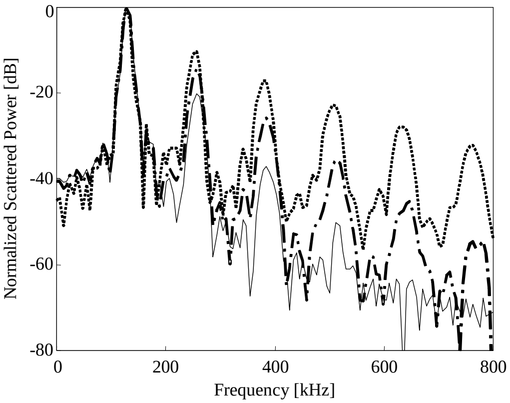

Figure 4.1: *Frequency spectra of the simulated backscattered echo for a bubble of 48 μm insonified with a 130 kHz ultrasound wave for different acoustic pressures: solid line 7.5 kPa; dashed line 15 kPa; dotted line 30 kPa.*

Figure 4.2 shows that, for a given insonation frequency, the harmonic generation is also strongly correlated to the size of the bubble. The figure shows the fundamental, second, third and fourth harmonic components as a function of the bubble diameter for an ultrasound field of 130 kHz. The maximal level of each harmonic component (second, third and fourth) occurs at the resonance size (48 μm diameter). A second peak amplitude appears for half the resonance size (24 μm diameter). For bubbles larger than the resonance size, the harmonic levels decrease significantly. Therefore, the harmonic level can be an indicator of bubble size.

Table 4.1 presents the resonance frequency of different bubble sizes. The bubbles contain air inside and water is considered as the surrounding medium. The resonance frequency was computed using the formula given

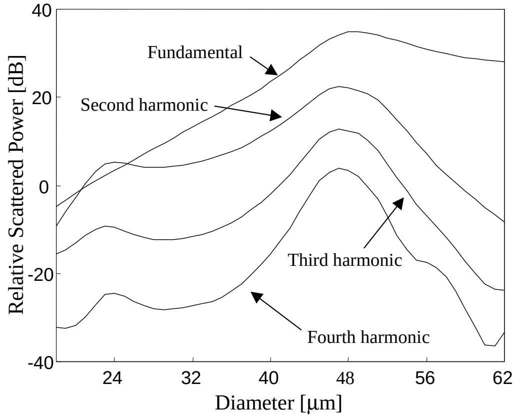

Figure 4.2: *Simulated fundamental, second, third and fourth harmonic scattered levels as a function of the bubble diameter using an ultrasound wave of 30 kPa and 130 kHz.*

by Medwin [18]:

$$f_r^2 = \frac{S_A}{4\pi^2 m} b\beta \tag{4.2}$$

where

S_A	is the stiffness of the bubble-liquid interface;
m	is the effective mass of the system;
b=$1/\kappa$, κ	is the polytropic exponent;
β	is the surface tension.

The effective mass, the polytropic exponent and the surface tension coefficient were given in reference 18.

As shown in Table 4.1, the resonance frequency decreases when the bubble becomes larger. Therefore, it is necessary to operate at low frequencies (in the kHz range) to approach the resonance of gaseous emboli and maximize the harmonic production. Moreover, operating at low frequencies minimizes the generation of harmonics during the propagation of the ultrasound wave. Therefore, no contaminating harmonics due to the nonlinear propagation are produced in the scattered echo.

4.3 Measurements

A device was developed to produce different populations of calibrated microbubbles (Chapter 2). By varying external parameters, we were able

Bubble Diameter(μm)	Resonance frequency (kHz)
10	616
20	303
30	203
40	153
50	124
60	103
80	78
100	62
120	52
140	45
160	39
180	35
200	32

Table 4.1: *Theoretical resonance frequency as a function of the bubble diameter*

to produce bubbles with diameters ranging from 19 μm to 200 μm. An imaging system, illustrated in Figure 4.3 was developed to measure the size and the number of the produced bubbles. It is composed of a variable zoom microscope coupled to a CCD camera (SONY). A flash was used to obtain bubble images with a good contrast and free of motion blurring. Each frame was saved on a personal computer for latter measurements of the bubble diameters and numbers. The produced bubbles were found to have a very narrow distribution (for example, the standard deviation for

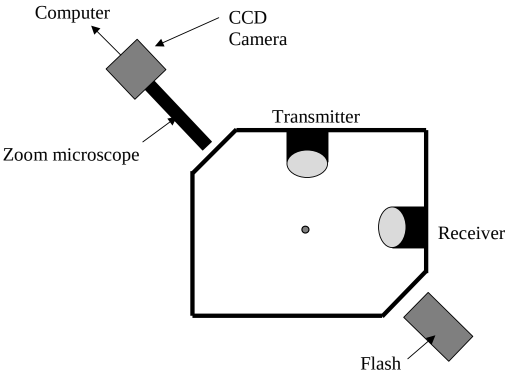

Figure 4.3: *Experimental imaging setup (top view).*

bubble size of 50 μm was 1.5 μm). Figure 4.4 shows images from different bubble populations used in this study.

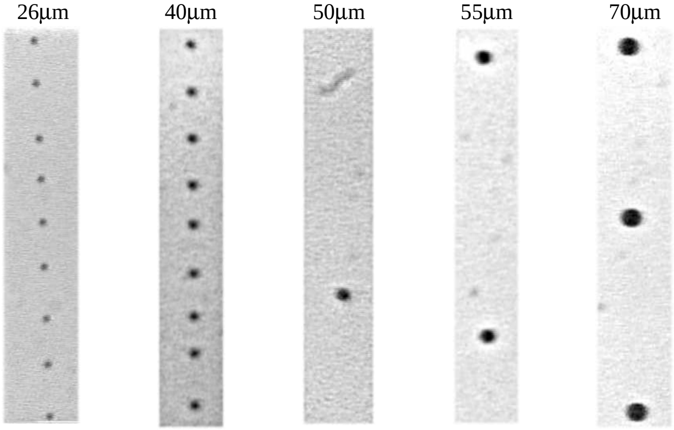

Figure 4.4: *Examples of bubbles produced using set-up shown in Figure 4.3.*

The experimental setup is shown in Figure 4.5. Four single element transducers operating at 130 kHz, 250 kHz, 500 kHz and 1 MHz were used. The transducers operating at 130 kHz and 250 kHz (Matec Instrument Companies Inc, Northborough, USA) were unfocused and used in transmission mode only. The 500 kHz and 1 MHz transducers (Panametrics, Whaltham, USA) were both focused at 75 mm) and used in a passive reception mode. These transmitting and receiving transducers were mounted in the tank perpendicularly as shown in Figure 4.5. The water tank was filled with ISOTON II. A narrow band sine wave burst (10 cycles and 20 cycles for 130 kHz and 250 kHz, respectively) was generated by an Arbitrary Waveform Generator (LW 420A, Lecroy, Chesnut Ridge, NY, USA). This signal was then amplified by an RF Power Amplifier (Model 2100L, ENI, Rochester, USA) and tuned to each transducer to reduce the electrical impedance mismatch. The amplitude of the signal could be adjusted by using a separate variable attenuators (355C/D, HP, Palo Alto, USA). The response of the bubbles received from either the 500 kHz or 1 MHz transducer was amplified using a Pulser Receiver (Model 5052PR, Panametrics) and then sampled on a digital oscilloscope (Model 9400A, Lecroy) with a sampling rate of 50 MHz. A Pulser Generator (PM 5716, Philips, Stockholm, Sweden) was used for synchronization. The response of the bubbles was averaged over 15 traces and acquired on a personal computer for further analysis. The acquired backscattered echo does not correspond to the response of a single bubble, but to the number of bubbles present in the ultrasound beam. This number varies according to the air pressure and the liquid flow used.

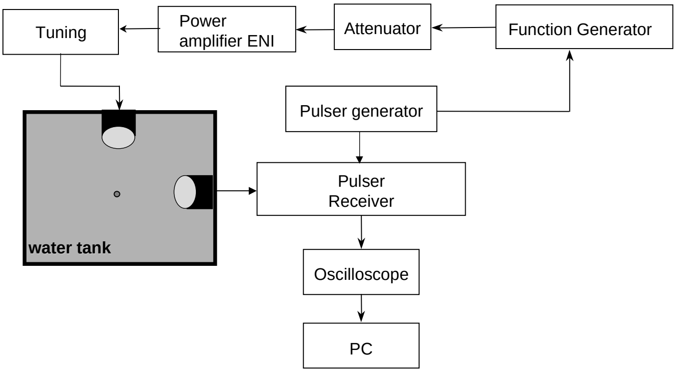

Figure 4.5: *Experimental acoustical setup.*

4.4 Results

Experimental results were obtained using transducers of 130 kHz and 250 kHz in transmission. The acoustic pressure generated at the region of interest as measured with a hydrophone was 30 kPa for the 130 kHz transducer and 54 kPa for the 250 kHz transducer. These transmitted pressures correspond to the maximal amplitudes that could be applied to the bubbles flowpath without inducing any disturbance. Higher pressures generated strong radiation forces pushing the bubbles from their initial stream. Figure 4.6a shows an example of the acoustic pressure generated by the 130 kHz transducer at a distance of 75 mm. The spectrum of this signal is displayed in Figure 4.6b. We clearly see that the propagation of the ultrasound wave is only linear and that no harmonic components were generated during propagation. Figures 4.7a-f present the normalized scattered power spectra measured using 130 kHz transducer in transmission and 500 kHz transducer in reception for six different bubble sizes: 80 μm, 62 μm, 54 μm, 48 μm, 44 μm and 35 μm. The resonance frequencies of these bubbles are, respectively, 78 kHz, 100 kHz, 114 kHz, 128 kHz, 140 kHz and 175 kHz (resonance frequencies were computed using Equation 4.2). These spectra illustrate the behavior of the bubbles, depending on their size. Bubbles with a diameter greater than 62 μm behave linearly and their scattered echoes exhibit a peak only at the transmitted funda-

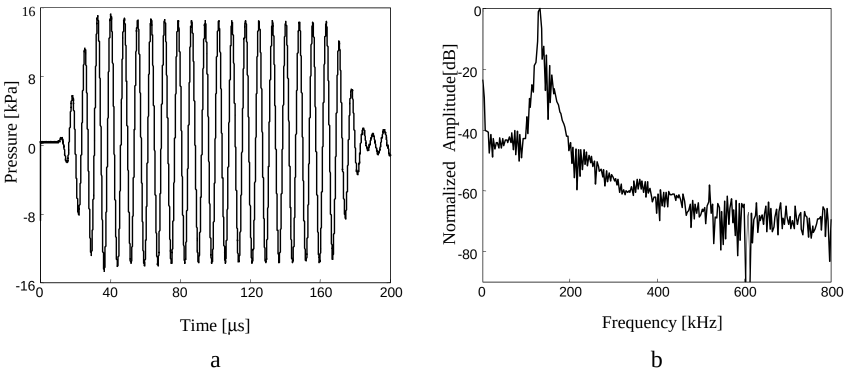

Figure 4.6: *a) Acoustic pressure generated by the 130 kHz transducer measured at a distance of 75 mm; b) spectrum of the acoustic pressure signal.*

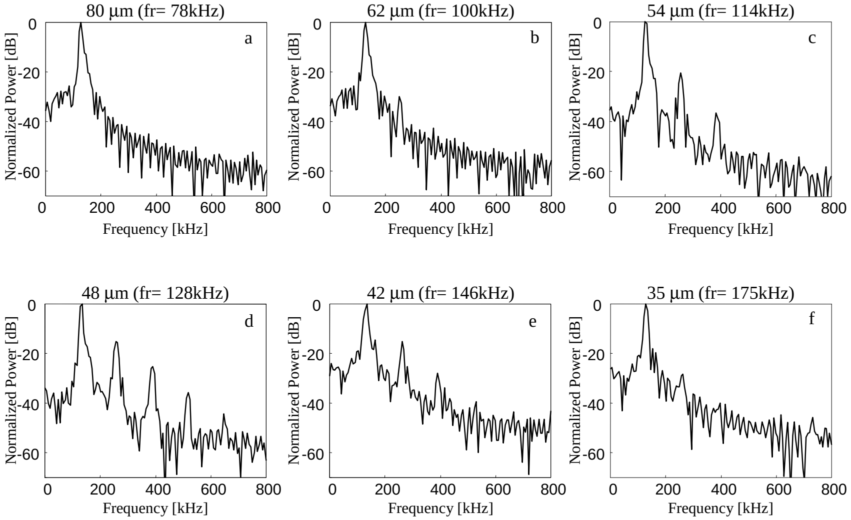

Figure 4.7: *Frequency spectra of scattered echoes for different bubble diameters insonified at 130 kHz: a) 80 μm; b) 62 μm; c) 54 μm; d) 48 μm; e) 42 μm; f) 35 μm.*

mental frequency, as shown in Figure 4.7a for bubbles of 80 μm. When the resonance frequency of the bubbles approaches the transmitted frequency, harmonic components are more and more present in the spectrum (Figure 4.7b-f. A second harmonic component starts appearing for bubbles of 62 μm and 35 μm, sizes closer to the resonance size. These two sizes can be considered as the limit sizes for harmonic generation using 130 kHz insonation frequency. The highest harmonic production appears for the resonant bubbles, in this particular case 48 μm (Figure 4.7d). The response of 48 μm bubbles shows even a fifth harmonic at 650 kHz. These results demonstrate that higher harmonics were generated when the resonance frequency of the bubbles coincided with the emitted frequency. When the resonance frequency is far away from the transmitted frequency (either smaller or higher) the bubbles respond linearly.

According to Eatock and Nishi[12] and to the simulated results presented in Figure 4.2, harmonic components could also be detected in the scattered echo of bubbles with sizes corresponding to half the resonance size. In our case, with an emission frequency of 130 kHz, the resonance size is 48 μm and half the resonance size is 24 μm. This result was confirmed in our experiments and shown in Figure 4.8a-c. These figures present the scattered spectra of bubbles with diameters of 27 μm, 22 μm and 19 μm. We can clearly appreciate the high number of harmonics generated for bubbles extremely close to half the resonance size (22 μm Figure 4.8b). For bubbles either smaller or larger than half the resonance, the number of harmonics progressively decreases as shown in the frequency spectrum of bubbles sizes of 27 μm and 19 μm (Figure 4.8a and c).

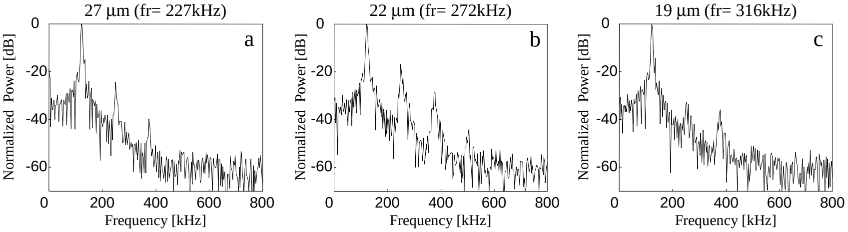

Figure 4.8: *Frequency spectrum of scattered echoes from different bubble diameters insonified at 130 kHz: a) 27 μm; b) 22 μm; c) 19 μm*

A comparison between simulated and measured data is shown in Figure 4.9. In this figure the levels of the second, third and fourth harmonic components as a function of the bubble size are shown. Figures 4.9a-c displayed the results when using 130 kHz transmission frequency. All the harmonics have a maximum amplitude around the resonance size (48 μm) and a second peak at half the resonance size (24 μm). Referring to Figure 4.2, the harmonic levels of bubbles around half the resonance size should be lower than the harmonic levels of resonant bubbles. However, both scattering levels are comparable. This is due to the number of bubbles present in the ultrasonic beam; a larger number of bubbles of half the resonance size (around 100 bubbles) was produced compared to the number of resonant bubbles (around 25 bubbles). A similar trend of results was noticed when employing a 250 kHz transducer in emission coupled to a 1 MHz transducer in reception (Figure 4.9d-f). For this situation, we generated bubbles from 19 μm to 35 μm. Our results show that bubbles larger than 30 μm behave linearly. Bubbles at the resonance size exhibited the maximal harmonic generation and even a fifth harmonic was appreciated. Due to our inability to produce bubbles smaller than 19 μm the lower limit of the harmonic detection could not be found experimentally. The spectrum of bubbles with a diameter of 19 μm was still presenting a quite strong second harmonic, which tends to suggest that smaller bubbles can be detected by their harmonic emissions (in particular, the second harmonic).

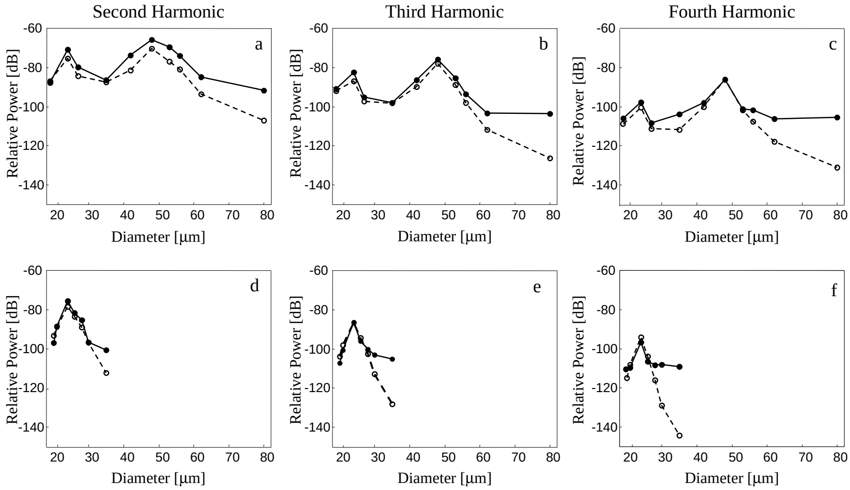

Figure 4.9: *Simulated (dotted line) and measured (solid line) harmonics levels as function of the bubble size: a)-b)-c): second, third and fourth harmonic using a transmission frequency of 130 kHz; d)-e)-f): second, third and fourth harmonic using a transmission frequency of 250 kHz.*

In general, a good agreement is obtained between theory and experimental data. The theoretical model appears to be a useful tool for predicting the behavior of bubbles under ultrasound irradiation. The main discrepancy between simulated and experimental results is due to the effect of the background noise on the harmonic production. This noise is characterized by the formation of a plateau for bubbles larger than the resonance size. This plateau is particularly present in the third and fourth harmonic levels and appears as a limitation to the detection of harmonic components. Some general comments can be made regarding the harmonic levels as function of the embolus size independently of the transmitted frequency. The second harmonic levels (Figure 4.9a and d) exhibit a broad peak, revealing that a large range of bubble sizes can generate a second harmonic. For the third harmonic (Figure 4.9b and e) this peak is narrower due to the fact that only fewer bubbles are able to scatter at the third harmonic frequency. The fourth harmonic (Figure 4.9c and f) is generated only by bubbles very close to the resonance size and the fifth harmonic is produced exclusively by resonant bubbles. This demonstrates that higher harmonics are more sensitive in sizing the bubbles. Therefore, we propose to use the lower harmonics (second or third) to indicate the presence of circulating bubbles and higher harmonics (fourth or fifth) for size determination.

4.5 Conclusions

This chapter demonstrates that the nonlinear behavior of the bubbles (the formation of harmonic components in the frequency spectrum of the scattered echo) may be applicable for the detection and discrimination between different bubble sizes. The use of low frequency transducers offers two main advantages. First, low frequencies generate negligible distortions due to nonlinear propagation. Therefore, any second harmonic contained in the received signals is only due to the nonlinear response of the bubbles and cannot be attributed to nonlinear propagation. Second, low frequencies are much closer to the resonance frequencies of gaseous emboli and, consequently, the acoustic pressure threshold needed to induce nonlinear vibrations of bubbles is reduced.

The technique proposed to detect and characterize circulating emboli is based on the bubble's harmonic scattering. The study of the fundamental component of the frequency spectrum was not included in this chapter. The backscattered echo at the fundamental frequency includes the contribution of all particles present in the ultrasound beam, regardless of size or nature (gaseous or solid). Thus, the fundamental component can only be correlated to the presence of moving particles in the flow, but cannot be used to characterize them. Discrimination between solid and gaseous emboli is performed by monitoring the harmonic emissions: when the frequency spectrum of the backscattered echo exhibits a second (and higher harmonics) component, the particles can be identified as gas emboli because solid particles scatter only linearly. The fourth or fifth harmonic is used to estimate the gaseous embolus size. The fifth harmonic appears to be the most sensitive estimator: bubble size can be evaluated with a maximal deviation of $\pm 2\,\mu$m from resonating bubbles.

As in previous studies, the presented results show that ultrasonic methods exploiting the nonlinearity of the bubbles are sensitive only to specific bubble populations. As an example, only bubble diameters ranging from $30\,\mu$m to $19\,\mu$m insonified at 250 kHz can generate a second harmonic component, and other bubble populations remain undetectable. Nevertheless, the use of two different transducers allows a detection of a larger interval of sizes: with 130 kHz and 250 kHz, bubbles from less than $19\,\mu$m up to $62\,\mu$m could be detected by selecting the second harmonic frequency. Larger bubbles behave linearly and cannot be identified as gaseous emboli. Bubbles smaller than $19\,\mu$m could not be generated. Thus, none experimental conclusion can be made concerning the lower limit of detectable bubbles with the current frequency selection. Resonating bubbles can be selectively detected using the fourth or fifth harmonic. Operating at 130 kHz, bubble diameters of $48\,\mu$m and $24\,\mu$m scatter at the fourth and fifth harmonic frequencies. Operating at 250 kHz, only bubbles of $24\,\mu$m show high harmonic components in their response. Consequently the use of different driving frequencies presents the opportunity to detect a wider range of bubble diameter and to discriminate between different bubble populations.

The present results demonstrate the feasibility of this technique for emboli detection, characterization and sizing. The occurrence of a second harmonic in the frequency spectrum of the received echo allows the detection of gaseous emboli and their distinction from other moving particles (particulate emboli). At this stage in our study, only bubbles generating at least a second harmonic can be differentiated from solid particles. Other bubbles (size not close enough to the resonance size) behave linearly and their frequency spectra would be identical to those of solid particles. Thus, lower frequencies should be adopted to detect bubbles larger than $62\,\mu$m and higher frequencies should be selected to characterize bubbles on the order of few micrometers.

A second orientation of our studies will be to develop a complete multifrequency technique for the detection and differentiation of circulating gaseous and solid emboli. The subharmonic emission from gaseous bubbles also deserves further attention. Theory predicts that under certain conditions (frequency, excitation pulse, acoustic pressure), specific gas bubbles can scatter at half the transmitted frequency. This property could also be applied to the detection and characterization of gaseous emboli.

References

1. W.G. Austen and D.H. Howry, “Ultrasound as a method to detect bubbles or particulate matter in the arterial line during cardiopulmonary bypass”, *J Surg Res*, vol. 5, no. 6: pp. 283-284, 1965.

2. M.P. Spencer, S.D. Campbell, J.L. Sealey, F.C. Henry, and J. Lindberg, “Experiments on decompression bubbles in the circulation using ultrasonic and electromagnetic flowmeter”, *J Occup Med*, vol. 11, no. 5: pp. 238-244, 1969.

3. H. Markus, A. Loh, and M. Brown, “Detection of circulating cerebral emboli using Doppler ultrasound in a sheep model”, *J Neuro Sci*, vol. 122, no. 1: pp. 117-124, 1994.

4. M.A. Moehring and J.R. Klepper, “Pulse Doppler ultrasound detection, characterization and size estimation of emboli in flowing blood”, *IEEE Trans Biomed Eng*, vol. 41, no. 1: pp. 35-44, 1994.

5. D. Russell, R. Brucher, K.P. Madden, W.M. Clark, P.M. Sandset, and J.A. Zivin, “The intensity of the Doppler signal caused by arterial emboli depends on embolus type and size”, *Stroke*, vol. 23, no. 1: pp. 158, 1992.

6. J.L. Smith, D.H. Evans, P.R.F. Bell, and A.R. Naylor, “A comparison of four methods for distinguishing Doppler signals from gaseous and particulate emboli”, *Stroke*, vol. 29, no. 6: pp. 1133-1138, 1998.

7. T.G. Leighton, “The Acoustic Bubble”, London Academic Press Limited, 1994.

8. W. Fairbank and M. Scully, “A new noninvasive technique for cardiac pressure measurement: resonant scattering of ultrasound from bubbles”, *IEEE Trans Biom Eng*, vol. 24, no. 2: pp. 107-110, 1977.

9. J.W. Horton and C.H. Wells, “Resonance ultrasonic measurements of microscopic gas bubbles”, *Aviat Space Environ Med*, vol. 47, no. 7: pp. 777-787, 1976.

10. D.L. Miller, “Ultrasonic detection of resonant cavitation bubbles in a flow tube by their second harmonic emissions”, *Ultrasonics*, vol. 21, no. 5: pp. 217-224, 1981.

11. D.L. Miller, A.R. Williams, and D.R. Gross, “Characterization of cavitation in a flow-through exposure chamber by means of a resonant bubble detector”, *Ultrasonics*, vol. 22, no. 5: pp. 224-230, 1984.

12. B.C. Eatock and R.Y. Nishi, “Numerical studies of the spectrum of low intensity ultrasound scattered by bubbles”, *J Acoust Soc Am*, vol. 77, no. 5: pp. 1692-1701, 1985.

13. B. Hills, B. Kanani, and P. James, “Velocity of ultrasound as an indicator of bubble content”, *Undersea Biomed Res*, vol. 10, no. 1: pp. 17-22, 1983.

14. V.L. Newhouse and P.M. Shankar, “Bubble sizing measurements using the nonlinear mixing of two frequencies”, *J Acoust Soc Am*, vol. 75, no. 5: pp. 1473-1477, 1984.

15. T. Leighton, R. Lingard, A. Walton, and J. Field, “Acoustic bubble sizing by combination of subharmonic emissions with imaging frequency”, *Ultrasonics*, vol. 29, no. 4: pp. 319-323, 1991.

16. N. de Jong and L. Hoff, “Ultrasound scattering properties of albunex microspheres”, *Ultrasonics*, vol. 31, no. 3: pp. 175-181, 1993.

17. P.A. Frost and E.Y. Harper, “Acoustic radiation from surfaces oscillating at large amplitude and small Mach number”, *J Acoust Soc Am*, vol. 58, no. 2: pp. 318-325, 1975.

18. H. Medwin, “Counting bubbles acoustically: a review”, *Ultrasonics*, vol. 15, no. 1: pp. 7-13, 1977.

Chapter 5

Emboli characterization using subharmonic and ultraharmonic emissions

Abstract

Emboli detection and characterization is of importance for different patients, such as those undergoing carotid or cardiac surgery. The emboli occur as particulate or gaseous matters. To select the appropriate treatment and reduce the risk of embolism, it is essential to first detect, then classify and, ultimately size the emboli. We propose in this chapter an approach to characterize and size the emboli based on their nonlinear properties. Gaseous emboli were produced by generating single and uniform air bubbles. These bubbles had diameters ranging from 40 µm to 120 µm. Acoustic measurements were carried out and special attention was devoted to the generation of subharmonic and first ultraharmonic components for gas bubbles of different sizes and at different acoustic pressures. For the scanning frequency and the applied acoustic pressures used in this study, only bubbles ranging from 65 µm up to 110 µm are capable of generating a subharmonic and an ultraharmonic frequency components. However, gaseous emboli outside this range behave differently. In conclusions, such an approach can be used to provide information needed to classify and size emboli.

Based on the publication: "Subharmonic and ultraharmonic emissions for emboli detection and characterization" by P. Palanchon, A. Bouakaz, J. Klein and N. de Jong, *Ultrasound in Medicine and Biology*, vol. 29, no. 3: pp. 417-425, 2003.

5.1 Introduction

For several years, an increased interest has been devoted to the detection and characterization of gas embolism within a variety of clinical areas. Trans-Cranial Doppler (TCD) is now recognized as a reliable tool for detecting the occurrence of cerebral microemboli. This ultrasonic technique is based on the appearance of high-intensity transient signals in the TCD waveform as indicators of circulating emboli. Classifying and sizing emboli is critical for determining the type and size of emboli causing the most important brain damage, for selecting patients who present a high risk of stroke and, hence, for choosing the appropriate treatment (anticoagulants, antiplatelets). Extensive studies and developments have been carried out in a perspective to detect, characterize and possibly size circulating microemboli using TCD. These investigations have attributed to embolic signals different features (velocity, time duration, peak intensity, frequency content) that were extracted from the Doppler signals and analyzed as a function of their composition and size[1−4]. These methods did not lead to convincing results with respect to characterization and/or sizing of microemboli. Therefore, non- Doppler techniques may appear as an attractive alternative that can provide additional information from embolic signals. Such methods are based on the analysis of the radiofrequency (RF) signals instead of the commonly used Doppler signals. This new field of research can take advantage from the extensive research carried out using gas microbubbles. Indeed, for decades, many techniques have been proposed in the literature to detect gas bubbles through their nonlinear behavior[5]. These approaches were based on theoretical investigations as well as experimental data. Theory predicts that under certain acoustic conditions (transmitted frequency, pressure, pulse duration), specific bubbles vibrate nonlinearly. This nonlinearity is characterized by the generation of harmonic ($2f, 3f$), subharmonic ($f/2$) and ultraharmonic ($3f/2, 5f/2$) components in the frequency spectrum of the scattered signal from the bubble. Approaches based on combined frequencies technique[6] appeared as a sensitive tool to size air bubbles. Leighton[7] applied this technique experimentally by considering the nonlinear behavior of the bubbles. The bubble was simultaneously insonated by two different frequencies: the 'imaging' frequency, w_i, fixed and selected far from the resonance frequency of the bubble and the 'pumping' frequency, w_p. The pumping frequency was scanned across a frequency band where the bubble resonance is expected to lie. When the sum and difference component at the subharmonic frequency ($w_i \pm w_p/2$) was maximal, the value of the pumping frequency was defined as the resonance frequency of the bubble and the size was therefore estimated. The main disadvantage of this technique comes from the complex apparatus required to acquire data. Three different ultrasonic elements were involved: one transducer and one loudspeaker for transmitting the 'imaging' and the 'pumping' frequency and one hydrophone to detect the echo backscattered by the bubbles. Furthermore, this method can be used only to size a single bubble at a time. It cannot be applied to the detection of various bubble sizes simultaneously, as when a cluster of bubbles is produced.

In Chapter 4, a new approach to detect gaseous emboli by taking advantage of the higher harmonic components generated by the gaseous emboli have been proposed. The gaseous bubbles were insonified with low frequency ultrasound waves between 130 kHz and 250 kHz. Depending on their size, the frequency spectrum of the scattered echo included some harmonic components. Based on experimental measurements and modelling, off-resonance bubbles oscillated only linearly while bubbles close to the resonance size produced a second harmonic and higher harmonic components. Therefore, using specific scanning frequencies, selective bubble sizes could be discriminated from other moving particles or bubbles. It is known from the literature that nonlinear oscillations of gas bubbles can create also components at the subharmonic ($f/2$) and ultraharmonic ($3f/2$) frequencies. Such components have been studied mainly through numerical investigations[8–9]. Eller[10] and Neppiras[11] studied theoretically the subharmonic and other low frequencies components generation. Their results emphasized the fact that an acoustic threshold is required to generate subharmonic and ultraharmonic component. This threshold is minimal for bubble diameters close to twice the resonance size of the transmitted frequency while other bubble diameters can produce subharmonic and ultraharmonic component but for much higher applied acoustic pressures.

In this chapter, we propose to detect and size circulating emboli using the subharmonic and the first ultraharmonic components. This approach, which is a non-Doppler technique, is based on RF signals scattered by the embolus. By focusing on all these nonlinear components, detection of gas emboli and its differentiation from solid particles become realizable. Moreover, the success of sizing different gas emboli increases. It is known from the literature that solid particles do not scatter nonlinear frequency components. In addition, even at high acoustic pressures, no subharmonic or ultraharmonic component can be generated from nonlinear propagation effects. For that purpose, we have investigated the nonlinear behavior of flowing gas bubbles over a wide range of diameters: between 40 μm and 150 μm. The bubbles were produced using an experimental bubble maker which allows to make bubbles with highly uniform sizes. The subharmonic ($f/2$) and first ultraharmonic ($3f/2$) generation phenomena are particularly emphasized to better understand their physical properties. Their occurrence was studied as a function of the bubble sizes as well as the transmitted acoustic pressures for a scanning frequency of 130 kHz. The experimental results have been compared to a simplified theoretical model, the Keller equation, commonly used to predict the behavior of free gas bubbles. Such frequency components are used to detect and size selective bubble populations. We will demonstrate that with a single frequency, using properties of subharmonic, ultraharmonics and harmonics, bubbles around the resonance size and around twice the resonance size can be detected from the surrounding medium. This property reduces the number of frequencies required to characterize bubbles over a wide range of bubble sizes and increase further the confidence of the technique.

5.2 Methods

Theoretical Model

To study the dynamics of the free gas bubble, a model developed by Keller is used as the theory. This model was extensively described in Chapter 3 and the reader is asked to refer to this chapter for further details. The radius-time solution R(t) of the Equations 3.1 and 3.2 was used as the theoretical basis of this chapter. The predicted scattered echo from the bubbles is determined using a simplified relationship between the instantaneous radius of the bubble $R(t)$ and the wall velocity $\dot{R}(t)$. When the assumption of a large displacement amplitude is made but the Mach number is small, the echo is proportional to the time derivative of $R^2\dot{R}$ and is given by the following formula[12]:

$$E(t) = \frac{\rho}{z}(R(t)^2\ddot{R}(t) + 2R(t)\dot{R}(t)^2) \tag{5.1}$$

where z represents the distance between the bubble and the transducer.

Experimental Setup

A "bubble maker", based on the gas injection principle, was developed to produce different populations of calibrated microbubbles (Chapter 2). By varying either the type of micropipette or the liquid velocity, bubbles with diameters ranging from 40 μm to 150 μm were produced. These bubbles were found to have a very narrow size distribution (90% lie within ±6 μm around the mean diameter). The "bubble maker" is directly connected to the bottom of a water tank containing degassed water. A stream of bubbles is allowed to rise freely in water as they are released from the micropipette's tip. An imaging system composed of a variable zoom microscope (Scienscope, Chino, USA) coupled to a CCD camera (SONY) was used to record images of the flowing bubbles. Imaging frames were saved on a personal computer for measurements of the bubble diameters and numbers. The experimental acoustic setup is shown in Figure 5.1. A single element unfocused transducer operating at 130 kHz (Matec Instrument Companies Inc, Northborough, USA) with a nominal diameter of 31 mm was used in transmission mode. A hydrophone, oriented at an angle of 60 degrees to the direction of the insonating wave was used in a passive reception mode. The active element of the hydrophone had a diameter of 4 mm and its sensitivity remains constant over a frequency bandwidth from 40 kHz up to 1 MHz. The water tank was filled with degassed water. The stream of bubbles was positioned at a distance of 2 cm from the transducer surface, which corresponds to the distance where maximal acoustic pressure in the axial beam profile occurs. A narrow band sine wave burst of 30 cycles was generated by an arbitrary waveform generator (LW 420A, Lecroy, Chesnut Ridge, NY, USA). The pulse repetition rate was fixed at 200 ms. This signal was then amplified by a RF power amplifier (Model 2100L, ENI, Rochester, USA) and tuned through a dedicated tuning circuit to the transmitting transducer. The amplitude of the transmitted signal could be adjusted by using separate variable attenuators (355C/D, HP, Palo Alto, USA). Depending on the attenuator position, various acoustic pressures were measured at the region of interest. The measured peak to peak pressure ranged from 110 kPa up to 410 kPa. The response of the bubbles received by the hydrophone was sampled on a digital oscilloscope (Model 9400A, Lecroy) with a sampling rate of 50 MHz. A Pulser Generator (PM 5716, Philips, Stockholm, Sweden) was used for synchronization. The response of the bubbles was averaged over 10 successive traces and acquired on a Pentium III personal computer for further analysis. The stream of bubbles produced is very uniform and the bubble distribution (size and spatial distribution) remains constant over the acquisition period. Therefore, for each pulse, we can consider that the same bubble population is insonified. We assumed that each bubble contained in the ultrasound beam could be considered as an individual scatterer and that multiple scattering is negligible. Thus, the intensity of the scattered echo of N bubbles of similar size is given by the echo of one bubble multiplied by their number N[13]. The acquired backscattered echo was hence divided by the number of bubbles present over a distance of 1 mm around the center of the ultrasound beam. Over this distance, the acoustic pressure remains constant and corresponds to the maximal pressure measured.

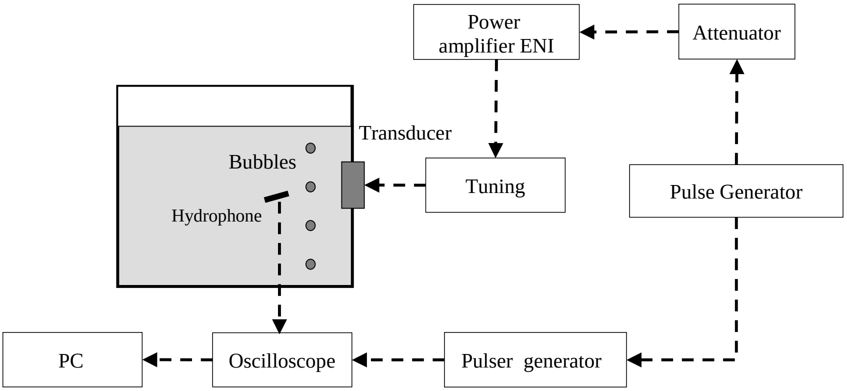

Figure 5.1: *Experimental acoustical setup.*

5.3 Results and Discussions

Figure 5.2 displays the frequency spectra of the backscattered signals from bubbles with six different sizes: 120 μm, 105 μm, 87 μm, 75 μm, 65 μm and 50 μm. The transmitted pressure was 310 kPa and the scanning frequency 130 kHz. According to the resonance frequency formula (Equation 4.2), the corresponding resonance size is 48 μm. Therefore, the bubble sizes currently investigated are above and below twice the resonance size (96 μm). For bubbles much larger than twice the resonance size as is the case for a bubble around 120 μm, the backscattered signal contains only the transmitted fundamental frequency component (Figure 5.2a). At this setting, such bubbles behave only linearly and do not generate subharmonic or ultraharmonic components. However, a very mild second harmonic component is seen but is 50 dB lower than the fundamental component. When the irradiated bubble is slightly smaller, in this particular case 105 μm (Figure 5.2b, a small ultraharmonic component at 195 kHz emerges from the background noise. However, no subharmonic component is seen yet for this size. This observation tends to suggest than the ultraharmonic component can be generated by the bubble earlier than the subharmonic component. For the bubbles with a diameter of 87 μm), which is close to twice the theoretical resonance size (Figure 5.2c), strong subharmonic and ultraharmonics (first and even second ultraharmonic) components can be clearly appreciated in the frequency spectrum. The subharmonic and ultraharmonic components are respectively 20 db and 30 db below the fundamental. As the bubble sizes are getting smaller than twice the resonance size, the levels of subharmonic and ultraharmonic components are progressively decreasing until their disappearance in the background noise. This process can be observed in successive spectra of bubbles of 75 μm, 65 μm and 50 μm (Figure 5.2d-f). However, a different tendency is observed for the second harmonic component. Indeed, the largest bubble used here (120 μm) shows a very tiny second harmonic energy. For bubble with a size close to twice the resonance size, a significant amount of second harmonic energy is generated and then we clearly notice a decrease in the second harmonic energy when the bubbles get smaller. The second harmonic level increases for the smallest bubble used here (50 μm) that is very close to the resonance size (48 μm). This nonlinear behavior tendency as a function of the bubbles' sizes was also noticed for the harmonic components at integer multiples of the fundamental frequency $(2, 3, 4)$ as already described in Chapter 4. The higher harmonic generation results showed that solid emboli and off-resonance bubbles scatter only linearly and hence produce echoes without harmonics. When the diameter of the bubbles is getting closer to the resonant size, higher harmonics are progressively produced (second and third harmonics) and for resonating bubbles, even a fourth and a fifth harmonic could be measured. The results shown here clearly demonstrate that bubble smaller than twice the resonance size can be distinguished from bubble larger than twice the resonance size. The

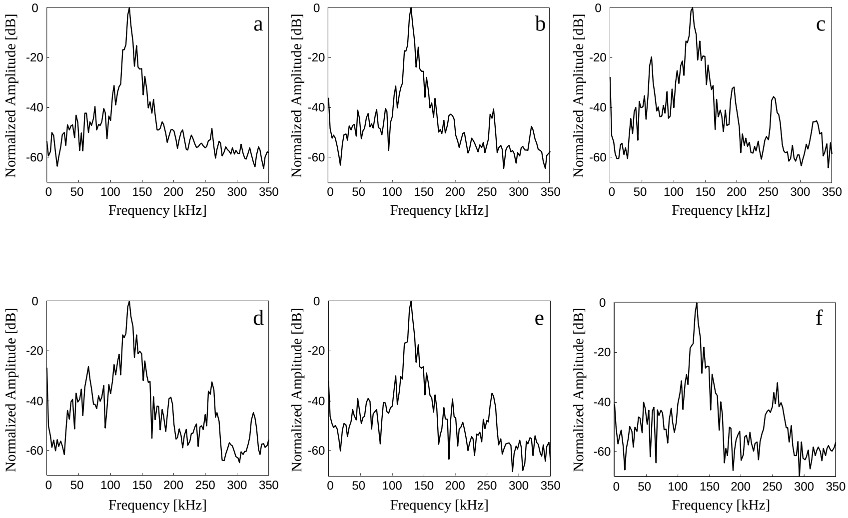

Figure 5.2: *Measured frequency spectra of scattered echoes for different bubble diameters insonified at 130 kHz and 310 kPa: a) 120 μm, b) 105 μm, c) 87 μm, d) 75 μm, e) 65 μm and f) 50 μm.*

main difference is situated at the level of the second harmonic component. As an example, bubbles of 120 μm (larger than twice the resonance size) show a very small peak at the second harmonic frequency, 260 kHz, while bubbles of 65 μm and 50 μm (smaller than twice the resonance size but much close to the resonance size) scatter a significant energy at this frequency. Thus, even if no subharmonic and/or ultraharmonic components are detected in the scattered frequency spectrum, size discrimination can be performed by selecting the generation of a second harmonic component or even higher harmonics ($3f, 4f$).

Figure 5.3 shows, for the scanning frequency of 130 kHz, the subharmonic (at 65 kHz) and the first ultraharmonic (195 kHz) levels of the backscattered signal as function of the bubble size for three different acoustic pressures: 210 kPa (□), 250 kPa (△) and 310 kPa (O). The bubble diameters range from 40 μm up to 105 μm. For acoustic pressures below 210 kPa, no subharmonic component was detected for all the sizes. This pressure corresponds to the minimal measured level required to generate subharmonic and ultraharmonic for these bubble sizes when they are insonified at 130 kHz. At a transmitted acoustic pressure of 210 kPa, a maximum energy is generated at the subharmonic frequency for bubbles around 92 μm as shown in Figure 5.3a. This size corresponds to twice the experimental resonance size. For bubbles slightly larger or smaller than 92 μm, the scattered subharmonic component decays rapidly and only bubbles between 80 μm and 98 μm in diameter can still oscillate at half the transmitted frequency. For bubbles below 80 μm, the measured bubble level remains constant, which is equal to the noise level and the limited dynamic range of the experimental set-up. When the applied pressure is increased to 250 kPa, a wider range of bubble sizes produces a subharmonic component (70 μm and 105 μm). However, we also observe that the maximal subharmonic component occurs for a bubble size of 85 μm, which is slightly smaller than twice the experimental resonance size (92 μm). Again, for much smaller bubbles the subharmonic level remains constant. As the pressure increased to 310 kPa, the maximal peak is shifted to 80 μm and the subharmonic level becomes extremely wide: bubbles between 58 μm up to 110 μm generate a subharmonic component. The shift in size where maximal subharmonic generation occurs when the applied acoustic pressure increased might be attributed to a different resonance frequency. Indeed, to compute the resonance frequency, we used the expression given by Medwin[14]. This expression is derived using linear theory, and we believe that this formula is not valid anymore at these high acoustic pressures, and the natural resonance frequency of a given bubble is slightly shifted to a lower value. Lauterborn[9] also mentioned such a shift for the ultraharmonic component. He explained this phenomenon by considering that, at high acoustic pressures, the bubbles start vibrating at a “free” frequency instead of their natural resonance frequency. This new oscillating frequency would be defined as the mean amplitude of the steady state oscillations.

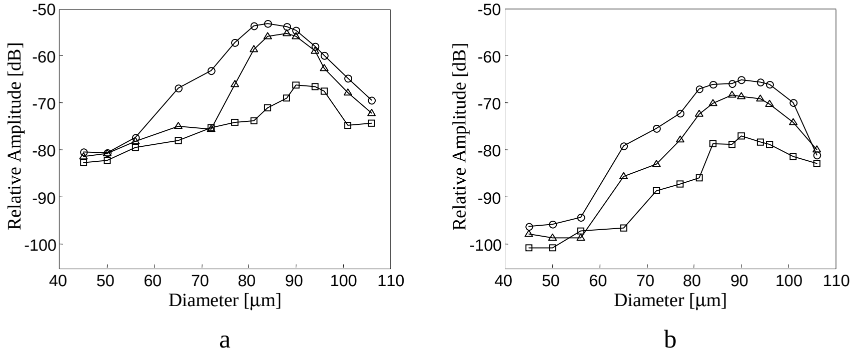

Figure 5.3: *Subharmonic and first ultraharmonic level as a function of the bubble diameter using a transmit frequency of 130 kHz for three different acoustic pressures: 210 kPa(□), 250 kPa(△) and 310 kPa(O): a) subharmonic level; b) ultraharmonic level.*

Figure 5.3b shows the ultraharmonic generation as a function of the diameter for the same applied acoustic pressures. For all the pressures, it can be noticed that the ultraharmonic component presents a wider peak than the subharmonic curve at its maximal value. The ultraharmonic component is spread over a wider bubble size range than the subharmonic component. This makes the ultraharmonic component less sensitive to size the bubbles but appears however as a better tool for bubble detection. The size shift of the maximal ultraharmonic level as the pressure increases is also noticed here but looks less apparent due to the wider maximal peak.

To look more closely at the subharmonic and ultraharmonic generation, we show in Figure 5.4 the subharmonic (△) and ultraharmonic (O) components as a function of the transmitted acoustic pressure. Four different bubble sizes were selected: 70 μm, 85 μm, 90 μm and 100 μm. These bubbles' sizes correspond to the regions below, close and above twice the resonance size. The acoustic pressures used here range from 110kPa up to 410 kPa. The development of the subharmonic and ultraharmonic component as function of the applied acoustic pressure shows for all sizes a similar trend consisting of three distinct stages: absence, growth and saturation. This evolution is markedly noticeable for bubbles close to twice the resonance size. For bubbles of 85 μm and 90 μm (Figure 5.4a and b), the subharmonic and ultraharmonic components emerge starting from an acoustic pressure

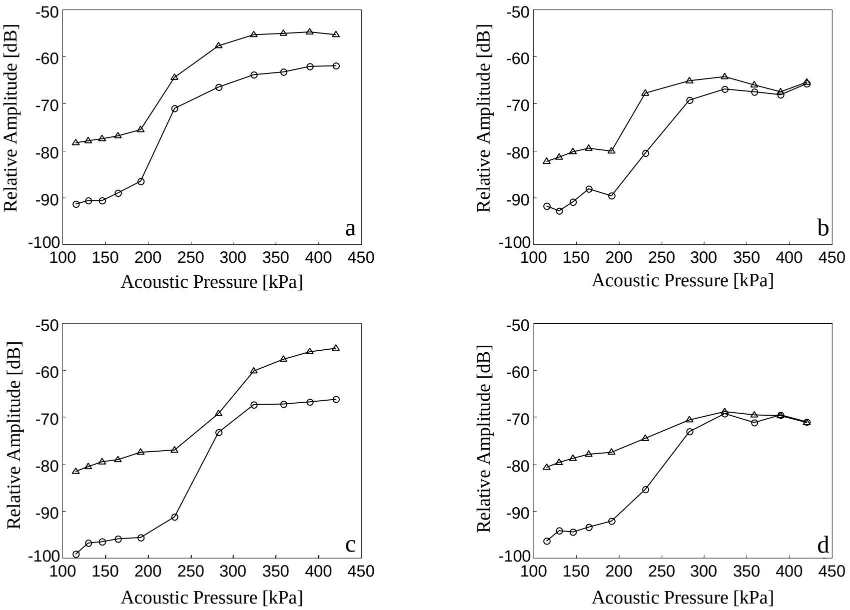

Figure 5.4: *Subharmonic (△) and ultraharmonic (O) levels as a function of the transmitted acoustic pressure using a scanning frequency of 130 kHz. Four different bubble sizes were studied: a) 85 μm; b) 85 μm; c) 70 μm and d) 100 μm.*

around 210 kPa. Between 210 kPa and 250 kPa, both components grow very rapidly with an increase up to 20 dB. For much larger acoustic pressures, the saturation phase is reached and constant levels are maintained. For a bubble size smaller than twice the resonance size, in this particular case a 70 μm bubble (Figure 5.4c), the subharmonic and ultraharmonic components behave differently. The subharmonic level rapidly grows between 210 kPa and 300 kPa above which the slope of growth is lower. For this size, we notice that the subharmonic component continues developing and up to the maximal pressure used here (410 kPa), no saturation phase has appeared. This behavior can be used to explain the shift in size at which a maximum subharmonic generation occurs when the acoustic pressure increased. Comparison of panels a and b with panel c shows that bubbles with size close to twice the resonance size exhibit a saturation phase for pressures above 300 kPa, while bubbles smaller than twice the resonance size still show an increase in their subharmonic component. Consequently, while the subharmonic level remains constant for bubble of twice the resonance size, it continues to grow for smaller bubbles giving hence a much broader range of bubbles oscillating at the subharmonic frequency. Probably, the saturation phase for smaller bubbles will be reached for acoustic pressures higher than (40 kPa). In contrary to the subharmonic component, the ultraharmonic component of the70 μm bubble seems to reach a saturation trend starting from pressures above 300 kPa. For bubbles larger than twice the resonance size, 100 μm (Figure 5.4d), the subharmonic component shows a linear growth between 180 kPa and 250 kPa. Such bubbles are quite far from twice the resonance size and only generate a small subharmonic component for high pressures. A saturation phase also occurs for very high pressures. The ultraharmonic component can also be decomposed into a rapid growth phase and a saturation phase. Nevertheless, it has to be noticed that the ultraharmonic component is becoming as strong as the subharmonic component in the saturation phase which means that the ultraharmonic can be generated in larger amounts compared to the subharmonic. For all bubble sizes, the ultraharmonic component is generated slightly earlier the subharmonic component. Lauterborn[9] has also demonstrated theoretically that for bubbles larger than 20 μm the generation of first ultraharmonic component required lower acoustic pressure threshold compared to the subharmonic generation.

Figure 5.5 displays the simulated subharmonic and ultraharmonic components as function of the bubble size. The acoustic pressures were selected to correspond to the measured amplitudes: 210 kPa (□), 250 kPa (△) and (310 kPa) (O). The simulated curves are given here for illustration purposes. At the lowest acoustic pressure, 210 kPa, the subharmonic component exhibits a narrow peak around a bubble size of 96 μm. This size corresponds to twice the theoretical resonance size as computed from the Medwin[14] formula. Experimentally, the maximal subharmonic component was occurring for a bubble size slightly smaller than 92 μm. As the pressure increases a size shift of the maximal subharmonic level and a broadening around twice the resonance size can be observed. For the highest pressure, the subharmonic component saturated over a wide range of bubble size. The same trends of results are also obtained for the first ultraharmonic component. These results corroborate the experimental data.

Figure 5.6 shows the required acoustic pressure to generate a subharmonic component at a frequency of 130 kHz as a function of the bubble diameter. Simulations are shown in solid line and measurement points are given in circles. The acoustic pressure has been normalized to the minimal required acoustic pressure for bubbles at twice the resonance size. The theoretical curve as a V-shape. Its vertex corresponds to the size that is able to produce a subharmonic for the lowest acoustic pressure, in that case 96 μm. As the acoustic pressure increases, a wider range of bubble

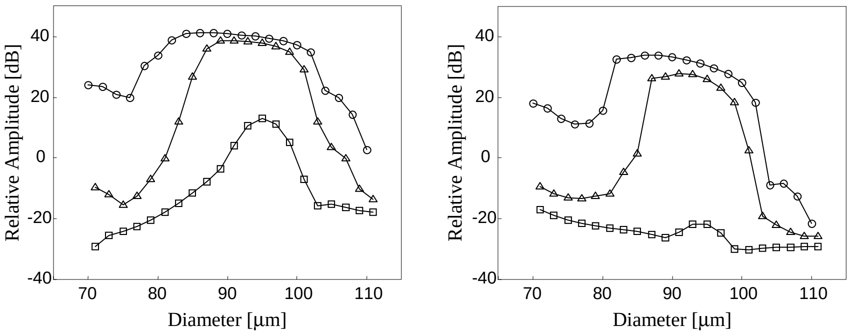

a

b

Figure 5.5: *Simulated subharmonic and first ultraharmonic level as a function of the bubble diameter using a transmitting frequency of 130 kHz for three different acoustic pressures: 210 kPa (□), 250 kPa(△) and 310 kPa(O): a) subharmonic level; b) ultraharmonic level.*

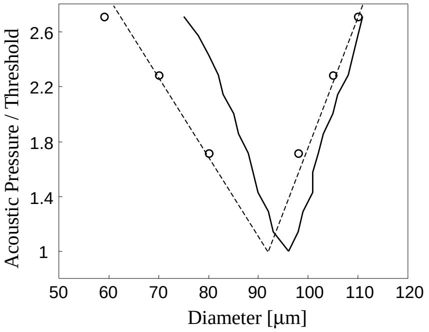

Figure 5.6: *Subharmonic generation as a function of the bubble size and the required acoustic pressure with a transmitting burst of 30 cycles at 130 kHz: simulated curve (solid line); experimental measurements (O); extrapolation of the measurements (dashed line).*

sizes could generate a subharmonic component. This result is confirmed by previous studies. We can also appreciate that the cone is not symmetric: bubbles smaller than twice the resonance size can produce a subharmonic for lower pressures than bubbles larger than twice the resonance size. The experimental points show a similar tendency. However with the instrumentation used in the set-up, it was not possible to use much lower excitation acoustic pressure without having a significant noise at the subharmonic frequency. The extrapolation of the experimental points, presented by a dashed line, shows however that the minimal acoustic pressure for subharmonic generation occurs for a bubbles size of 93 μm. As explained above in this section, the difference might be due to an experimental resonance frequency different from the computed one. Nevertheless, the asymmetry of the theoretical curve is also visible with the experimental data. These curves show that gas emboli around 90 μm generate a subharmonic component for all the applied pressures. Nevertheless, for bubbles below 70 μm or larger than 100 μm require much higher pressures, at least twice the lowest pressure, to produce a subharmonic component with significant signal to noise ratio. This characteristic can be exploited as a sizing parameter.

5.4 Conclusions

To date, the detection of circulating microemboli is performed using TCD instruments. This technique exploits only the Doppler signal extracted at the fundamental frequency component. The properties of the gas emboli at the scanning fundamental frequency resemble to a large extent to those of solid emboli. As a consequence, gas particle detection becomes cumbersome when only the transmitted frequency is used. As shown in this study, gas emboli have the property of splitting and redistributing the insonating energy into different components in the scattered acoustic spectrum. When the acoustic pressure is high enough, gas bubbles produce components at higher frequency (second harmonic and higher), the subharmonic frequency and the ultraharmonic frequency. These newly generated frequency components are intrinsic to gas emboli only and are not shown by solid emboli. In addition their generation depend on the size of the gaseous emboli. When bubbles are scanned at 130 kHz and with a transmitted acoustic pressure of 310 kPa, only bubbles between 65 μm and 110 μm can scatter at the subharmonic or the ultraharmonic frequency. Bigger bubbles still behave only linearly and their nature cannot be characterized. On the other side, smaller bubbles (less than 70 μm in this particular case), do not generate a subharmonic or an ultraharmonic component but a second harmonic component can be observed in the frequency spectrum. This component is also a characteristic of the nonlinear behavior of the bubbles. Overall, for a scanning frequency of 130 kHz, bubbles smaller than 110 μm can be detected from the surrounding medium and classified as a gaseous embolus.

The sizing procedure includes two different steps. A gross estimation of the bubble size can be obtained directly via the detection of the subharmonic, the ultraharmonic or higher harmonic components. As demonstrated in this chapter, only bubbles around twice the resonance size generate a subharmonic or an ultraharmonic component. Furthermore, bubbles close to the resonance size generate a second or higher harmonic components. The range of detectable bubble diameters is strongly dependent on the transmitted acoustic pressure. Higher the acoustic pressure is, wider the bubble size range will be. On the other hand, the sensitivity of the sizing estimation will decrease. A more precise estimation of the bubble size can be obtained by changing and adapting two different parameters: the frequency and the acoustic pressure. By changing them in an iterative process, the bottom of the triangle from Figure 5.6 can be reached which give a very accurate estimation of the bubble diameter. Other scanning frequency would be required to characterize larger bubbles. It is within this context that we suggest the use of subharmonic, ultraharmonic and higher harmonics components to detect an embolus, characterize its nature and ultimately determine its size.

Some discrepancies were noticed between the experimental and simulated results presented in this study. The most important difference occurs for the estimation of twice the resonance size. It can be explained by the fact that the equation used to compute the natural resonance frequency is not valid anymore in this situation. The level of the simulated subharmonic and ultraharmonic component as a function of the bubble size differs from those observed experimentally. For the study of higher harmonic production, a very good correlation was found between the simulated and the measured results that validated the theoretical model for describing the nonlinear behavior of the bubbles (see Chapters 3 and 4). It is thought that Keller equation is not well suited for the study of the subharmonic and ultraharmonic generation at the scanning frequency used here.

References

1. C. Lucchesi, G. Darbellay, J. Ponard, J.M. Vesin, J. Krayenbuehl, G. Devuyst, and G. Dietler, “Solid/gas and size classification via inductive machine learning: results and whereabouts”, *Cerevasc Dis*, vol. 11(suppl 3): pp. 1-47, 2001.

2. E.O. Belcher, “Quantification of bubbles formed in animals and man during decompression”, *IEEE Trans Biomed Eng*, vol. 27, no. 6: pp. 330-338, 1980.

3. M.A. Moehring, “Fundamental concepts regarding sizing and discrimination of air bubbles and red cell aggregates using pulse Doppler ultrasound”, *Echocardiography*, vol. 13, no. 5: pp. 567-571, 1996.

4. D. Russell and R. Brucher, “Discrimination of cerebral microemboli”, *Cerevasc Dis*, vol. 11(suppl3): pp. 4, 2001.

5. D.L. Miller, “Ultrasonic detection of resonant cavitation bubbles in a flow tube by their second harmonic emissions”, *Ultrasonics*, vol. 21, no. 5: pp. 217-224, 1981.

6. V.L. Newhouse and P.M. Shankar, “Bubble sizing measurements using the nonlinear mixing of two frequencies”, *J Acoust Soc Am*, vol. 75, no. 5: pp. 1473-1477, 1984.

7. T.G. Leighton, A.D. Phelps, D.G. Ramble, and D.A. Sharpe, “Comparison of the ability of eight acoustic techniques to detect and size a single bubble”, *Ultrasonics*, vol. 34, no. 6: pp. 661-667, 1996.

8. A. Prosperetti, “Nonlinear oscillations of gas bubbles in liquids: transient solutions and the connection between harmonic signal and cavitation”, *J Acoust Soc Am*, vol. 57, no. 4: pp. 810-821, 1975.

9. W. Lauterborn, “Numerical investigation of nonlinear oscillations of gas bubbles in liquids”, *J Acoust Soc Am*, vol. 59, no. 2: pp. 283-293, 1976.

10. A. Eller and H.G. Flynn, “Generation of subharmonics of order one-half by bubbles in a sound field”, *J Acoust Soc Am*, vol. 46, no. 3: pp. 722-727, 1968.

11. E.A. Neppiras, “Subharmonic and other low frequency emissions from bubbles in sound-irradiated liquids”, *J Acoust Soc Am*, vol. 46, no. 3: pp. 587-601, 1968.

12. P.A. Frost and E.Y. Harper, “Acoustic radiation from surfaces oscillating at large amplitude and small Mach number”, *J Acoust Soc Am*, vol. 58, no. 2: pp. 318-325, 1975.

13. N. de Jong and L. Hoff, “Ultrasound scattering properties of albunex microspheres”, *Ultrasonics*, vol. 31, no. 3: pp. 175-181, 1993.

14. H. Medwin, “Counting bubbles acoustically: a review”, *Ultrasonics*, vol. 15, no. 1: pp. 7-13, 1977.

Chapter 6

Emboli detection using new transducer designs

Chapter 6A

Single frequency transducer

Abstract

A specific transducer design has been developed to detect and characterize gaseous emboli using their nonlinear properties. It is composed of separate transmitting and receiving parts. The transmit part, consisting of a PZT material, emits at a frequency of 500 kHz and can generate pressures up to 410 kPa. On top of the transmit surface, a thin PVDF layer is glued and used for receiving frequencies from 250 kHz ($f_0/2$) up to 2.5 MHz ($5f_0$). In order to evaluate this new design, ultrasonic measurements were carried out with gas bubbles with diameters ranging from 10 µm up to 90 µm and solid particles between 350 µm and 550 µm. The experimental results confirmed our previous findings: gaseous emboli with a diameter close to the resonance size scatter significantly at higher harmonic components (from the 2nd harmonic up to the fifth) while bubbles with a diameter around twice the resonance size produce a subharmonic and/or an ultraharmonic component. Meanwhile, solid particles and bubble at other sizes behave only linearly and their scattered spectra appeared without any harmonics. The study demonstrates the utility of this approach in using a single transducer to detect and characterize selective gaseous emboli from other particles using their nonlinear behavior.

Based on the publication: "Emboli detection using a new transducer design" by P. Palanchon, A. Bouakaz, J. Klein and N. de Jong, *Ultrasound in Medecine and Biology*, vol. 30, no. 1: pp. 123-126, 2004.

6A.1 Introduction

Since the past decade, many efforts have been made to develop techniques that could allow the detection of micro-embolic signals, their classification as particulate or gaseous matter and, to a lesser extent, the estimation of their size. A reliable detection and characterization technique may have a number of important clinical applications, such as the adjustment of medical therapy according to the incidence of embolic signals. The commonly used techniques to detect circulating emboli are based on Doppler processing using Trans Cranial Doppler instruments. Embolic information may be extracted from the Doppler signal through the use of specific parameters[1−3] or signal processing techniques[4−6]. Although approaches based on TCD gave good results for the detection of circulating micro-emboli, none of them offers the possibility of characterizing and/or sizing these moving scatterers with a sufficient sensitivity. In Chapter 3 and Chapter 4, the nonlinear behavior of gaseous emboli has been suggested as a new direction of investigation. Under appropriate scanning conditions, a gaseous embolus may pulsate nonlinearly and the frequency spectrum of the backscattered signal will be characterized by the appearance, in addition to a fundamental component (at the transmitted frequency f_0), of harmonic $(2f_0, 3f_0)$, sub-harmonic $(f_0/2)$ or ultra-harmonic $(3f_0/2, 5f_0/2)$ components. In this approach the Doppler signal has been discarded to the benefit of the Radio Frequency (RF) signal. The RF signal is defined as the signal directly backscattered by the embolus. The Doppler signal, as used in TCD instrument, is only reconstructed from the fundamental frequency of the scattered RF signal and the information contained at other frequency bandwidths, such as the nonlinear components, are filtered out either by the transducer itself or by the Doppler processing. These nonlinear frequency components represent new and additional information generated by the microembolus and therefore should be considered for investigation.

When the nonlinear components have to be considered as useful information, their reception will require a specific technology to detect them with a sufficient sensitivity. First of all, it has been shown in Chapter 3 that the bubbles need to be insonified at a frequency close to their own resonance frequency to behave nonlinearly without transmitting considerable amount of acoustic power. Bubbles with diameters smaller or larger than the resonance size behave only linearly and do not scatter any harmonics. The resonance frequency of the bubbles being inversely proportional the bubble size, low-frequency technology has to be applied. As an example, a free air bubble with a diameter of $12\,\mu$m has a resonance frequency of 500 kHz. Furthermore, the detection of higher frequency components requires a wide frequency band in reception: from the sub-harmonic frequency up to the fifth harmonic frequency. Indeed, if a transmitted frequency of 500 kHz is considered, the RF signal may contain information in a frequency range between 250 kHz and 2.5 MHz. A single element transducer, such as the one used with TCD instruments, cannot achieve such a requirement due to its limited frequency band. A dedicated transducer design was developed to fulfill these technical conditions and is described in this chapter.

6A.2 Measurements and results

6A.2.1 Transducer characteristics

To achieve maximal sensitivity in transmission and reception modes, the transducer design investigated in this study is composed of separate transmitting and receiving capabilities. Two different materials have been selected from their own capacities to transmit and receive an ultrasound(US) signal. This prototype was designed in our laboratory and realized by SEA (Soquel, CA, USA). A picture is given in Figure 6A.1a. The aperture of the transmitting part is 16 mm and it has an unfocused surface. The transmitting part consists of a lead zirconate titanate ceramic (PZT), material known for its high capabilities in transmission. The receiving part of the design consists of a layer of polyvinylidene fluoride (PVDF) with a thickness of 400 μm. The PVDF layer was glued on top of the transmitting part. The PVDF material was chosen for its extremely good capabilities in passive reception mode over a wide frequency band. The receiving part of this transducer presents a relatively constant detection level for frequencies ranging from 50 kHz up to 5 MHz. Figure 6A.1b shows the transmitting and receiving frequency responses of the transducer. The center frequency is around 540 kHz and the bandwidth is 35% at -6 db. Figure 6A.2 shows the acoustic profiles of the transducer in the axial direction (Figure 6A.2a and in the radial direction (Figure 6A.2b measured at 65 mm. The transmitting pulse consisted of a burst of 10 cycles with a low drive level. For this transducer, the far field distance is 73 mm and the last axial maximum is reached around 20 mm. Beyond this depth, the acoustic pressure decays due to the divergence of the beam and at a distance of 40 mm (which corresponds to our depth of investigations) the pressure has decayed by 2dB. The lateral profile given in Figure 6A.2b was measured at 65 mm to avoid near field interferences. It shows a beam width of 8 mm at -3 dB level. This width is too wide for imaging purposes, but it is not a limitation for our application. Side lobes are created at approximately 25 mm radial extent with a level of -16 dB relative to the main lobe level.

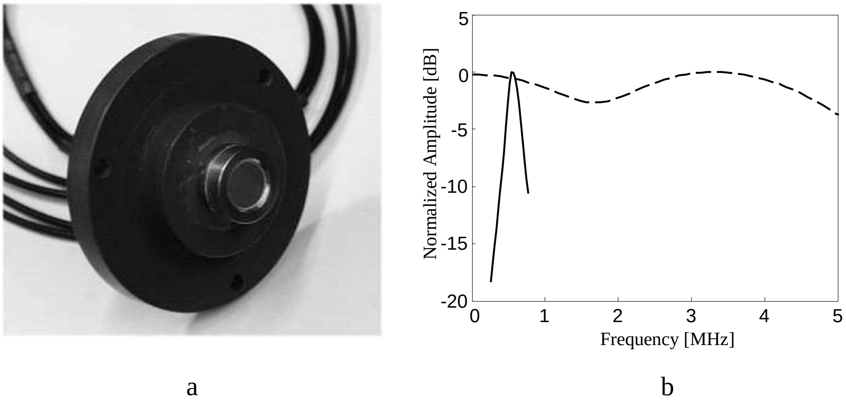

Figure 6A.1: *a) Picture of the prototype ; b) frequency response of the transmitting part (solid line) and the receiving part (dotted line).*

6A.2.2 Emboli investigation with the new transducer design

This transducer design has been tested for the detection and characterization of emboli through different sets of experiments. The embolic materials consisted of both gas bubbles and solid particles. The solid emboli were simulated using Contour Embolization Particles (Boston Scientific, Fremont, CA, USA) with diameters between 350 μm and 500 μm. Various bubbles populations were produced using a homemade bubble maker, allowing the generation of calibrated microbubbles[7]. Their diameters ranged from 10 μm to 90 μm. The stream of bubbles was positioned at a distance of 40 mm from the transducer surface. The acoustical experimental setup was composed of a sine wave burst generated by an Arbitrary Waveform Generator (LW 420A, Lecroy, Chesnut Ridge, NY, USA). The pulse repetition time (PRT) was adjusted to 10 ms. The signal was then amplified by a RF Power Amplifier (Model 2100L, ENI, Rochester, MA, USA). The amplitude of the transmitted signal could be adjusted with separate variable attenuators (355C/D, HP, Palo Alto, USA). The acoustic pressures at the location of the bubbles were measured using a needle hydrophone (Reson GmbH, Germany). They ranged from 110 kPa up to 410 kPa. The received signal was sampled on a digital oscilloscope (Model 9400A, Lecroy) with sampling rate of 50 MHz. A Pulser Generator (PM 5716, Philips, Stockholm, Sweden) was used for synchronization. The backscattered signal was averaged over 10 successive traces and acquired on a Pentium III personal computer for further analysis.

The behavior of air bubbles with a diameter well above the resonance size

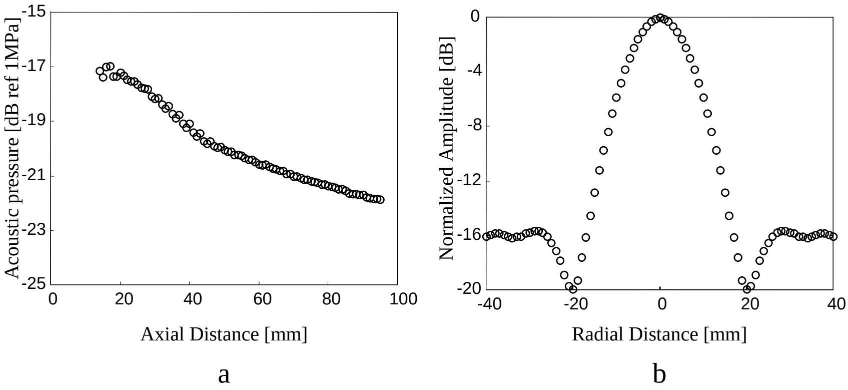

Figure 6A.2: *Measured acoustic beam profiles of the generated acoustic field. a) axial beam profile, b) lateral beam profile measured at 65 mm.*

(12 μm) was investigated. These bubbles have, respectively, a diameter of 90 μm, 60 μm and 35 μm corresponding to resonance frequencies of 71 kHz, 106 kHz and 178 kHz. A burst of 10 cycles with an acoustic pressure of 150 kPa was applied to the stream of bubbles. The measured spectrum of the backscattered signal from the bubbles and received at the PVDF surface exhibits a peak only at the transmitted frequency, which means that such bubbles behave only linearly. The scattering behavior is dependant on the bubble size: the larger the bubble, the higher the scattered power will be. Bubbles with a diameter larger than the resonance size can be detected through an increase of the power of the RF signal at the transmitted frequency, but no information concerning the nature or the size of these emboli can be extracted from the radio frequency signals.

Due to intrinsic limitations of our bubbles maker, a proper stream of uniform bubbles with a diameter smaller than 30 μm could not be obtained and was replaced by a cloud of bubbles. These bubbles do not present a uniform diameter but their distribution size is narrow enough to make some conclusions regarding the results obtained with such a population of bubbles. For the set of measurements, bubbles with a mean diameter around the resonance size and twice the resonance size were investigated. Figure 6A.3a presents the frequency spectrum of the scattered signal from bubbles with a mean diameter of 12 μm, which correspond to the resonance size of the scanning frequency. The measured acoustic pressure was 150 kPa at the bubbles' location. Higher frequency components can clearly be identified: second, third, fourth and even a small fifth harmonic. Figure 6A.3b displays the scattered frequency spectrum from a cloud of bubbles with a mean diameter corresponding to twice the resonance size of ($24\,\mu$m). The transmit pulse had an acoustic pressure of 410 kPa and contained 10 cycles. From the spectrum, subharmonic and ultraharmonic components can clearly be observed. This is in accordance with the theory that predicts a low acoustic pressure to generate subharmonic and ultraharmonic component when the transmitting frequency is close to twice the resonance frequency of the insonified bubbles.

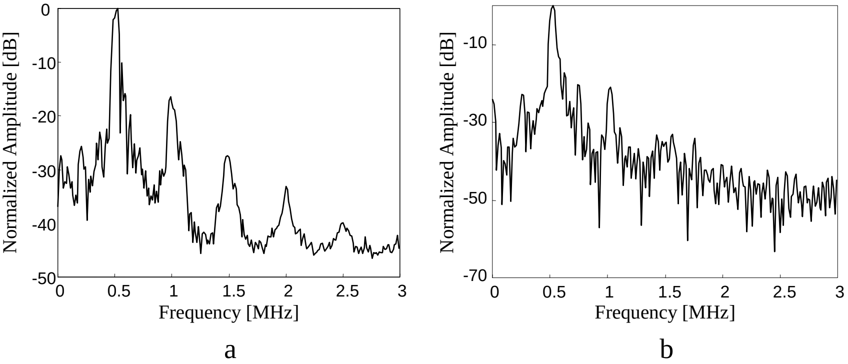

Figure 6A.3: *a) Frequency spectrum of the signal backscattered by a mixture of bubbles with diameters close to the resonance size; b) frequency spectrum of the signal backscattered by a mixture of bubbles with diameters close to twice the resonance.*

The detection of solid emboli was carried out using an acoustical arrangement slightly different from the previous experiments. The new ultrasonic transducer was mounted in a water bath and generates a four-cycles burst at 150 kPa. Contour Embolization particles were used to simulate particulate emboli at a concentration of 1 mm^3 diluted in 200 ml of water. These particles were diluted in a small container at a distance of 70 mm from the transducer. As expected by theory (see Chapters 3 and 4), the solid particles behave linearly and the frequency spectrum of the backscattered signals exhibited a peak only at the fundamental frequency.

6A.3 Discussions and conclusions

In this chapter, a new transducer design has been investigated for the detection and classification (gaseous or particulate matter) of micro-emboli *via* the nonlinear behavior of gas bubbles. The main advantage of this configuration is that optimal transmission and reception modes are achieved with a single transducer. The detection of microemboli from the surrounding medium and the production of nonlinear components require a high sensitivity in transmission. In addition, a wide frequency band in reception allows the recording of frequency components that, until now, were discarded in emboli studies. The preliminary results confirm the previous conclusions obtained with several transducers:

> 1) either gas bubbles or solid particles can be detected from the surrounding medium. Their scattering properties are directly correlated to their size or their number as predicted by the theory;
> 2) air bubbles with a diameter close to the resonance size generate higher harmonics (second up to the fifth);
> 3) air bubbles with a diameter close to twice the resonance size exhibit a subharmonic and ultraharmonic component;
> 4) a size estimation of the bubbles can be performed by looking to the type of nonlinear component produced: subharmonic (bubbles around $24\,\mu$m) or higher harmonics (bubbles around $12\,\mu$m).

Overall, such a transducer appears very valuable for the detection, the characterization and the sizing of gaseous emboli. Similar design can also be adapted to detect and characterize emboli using TCD. Nevertheless, the current design presents some technical limitations: the most important one is the limited range of detectable bubble sizes due to a single transmitted frequency. To increase the range of bubble diameters that can be characterized, a multi-frequency transducer should be developed. Each transmitted frequency will lead to the detection of bubble populations around its resonance size and twice its resonance size. This approach is currently under investigation.

Chapter 6B

Multifrequency frequency transducer

Abstract

The classification of circulating microemboli as gaseous or particulate matter is essential to establish the relevance of the detected embolic signals. Until now, Doppler techniques have failed to determine unambiguously the nature of circulating microemboli. Recently, we have introduced a new approach based on the analysis of Radio Frequency (RF) signal and using the nonlinear characteristics of gaseous bubbles to characterize emboli. The main limitation of these studies was the requirement of two separate transducers for transmission and reception. This study presents a multi-frequency transducer with two independent transmitting elements and a separate receiving part with a wide frequency band. The transmitting elements are positioned in a concentric design and cover a frequency band between 100 kHz and 600 kHz. The receiving part consists of a PVDF layer. The new transducer has been tested in vitro using gaseous emboli. It could correctly classify and size air emboli with diameters ranging from 10 μm to 105 μm.

Based on the publication: " Multifrequency transducer for microemboli classification and sizing" by P. Palanchon, A. Bouakaz, J. Klein and N. de Jong, *Accepted for publication in IEEE Transactions on Biomedical Engineering.*

6B.1 Introduction

In Chapter 6A, a new transducer design with adequate transmitting and receiving capabilities was presented. This transducer was composed of a transmitting part, emitting at a center frequency of 500 kHz. On top of it, a layer of polyvinylidene fluoride (PVDF) was glued and used as a passive receiver. Experimental measurements showed that such a configuration could only characterize gaseous emboli with a diameter smaller than 35 μm, whereas larger emboli could be correctly detected, but not discriminated from particulate emboli. To overcome this limitation and increase the method specificity by enlarging the range of detectable gaseous embolus sizes, a multifrequency transducer, also named "Embolus Transducer", was designed and constructed. It is based on a similar design as the single frequency transducer but contains two independent transmitting elements. They operate at center frequencies of 130 kHz and 360 kHz, respectively. The reception of the backscattered RF signal is achieved by a third element, characterized by a wide frequency band, located on the surface of the transmitting part.

6B.2 Transducer design

The multifrequency transducer designed for microemboli harmonic classification is displayed in Fig. 6B.1. It is composed of three separate and independent elements: two elements are used in transmission and one in reception. The transmitting part consists of two concentric piezocomposite elements. The outer element operates at a center frequency of 130 kHz and the inner element operates at a center frequency of 360 kHz. Both elements can be driven separately and can operate indifferently in transmission or in reception mode. A specific electronic tuning was included to compensate for the impedance mismatch between the transmitters and the external electronic devices. It consisted of inductances of 470 μH for the high frequency (HF) inner element and 1880 μH for the low frequency (LF) outer element, mounted in series with each transmitting element. A matching layer composed of epoxy (thickness $\lambda/4$ of each frequency) was added to the surface of these two elements to couple the transmitting part to the propagation medium and no backing was used. A schematic drawing displayed in Fig. 6B.1b, details the multifrequency transducer design. The inner element has a diameter of 20 mm and the width of the outer ring is 3.7 mm. The thickness of each element is, respectively, 5 mm for the high frequency inner element and 13 mm for the low frequency outer ring. To avoid any interference and crosstalk between both elements, a filler was inserted between the two transmitters. The receiving part consists of a 110 μm thick layer of polyvinylidene fluoride (PVDF) glued on top of the matching layer and covers the complete transducer surface. The total aperture of the transducer is 30 mm.

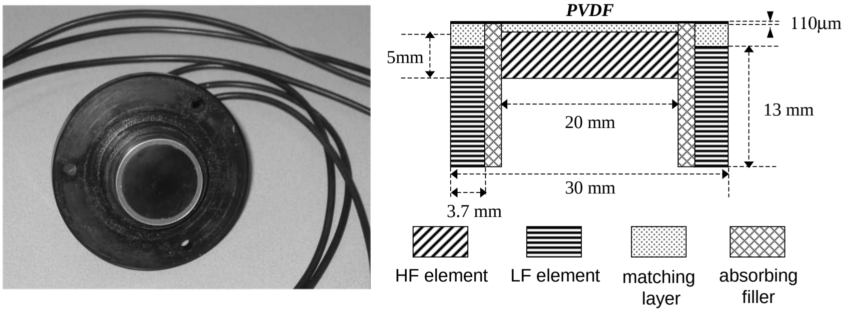

a b

Figure 6B.1: *a) Photograph of the multifrequency transducer; b) transversal drawing of the transducer.*

6B.3 Experimental setup

6B.3.1 Transducer characteristics measurements

To evaluate the ultrasonic capabilities of this transducer, beam profiles and sensitivity measurements were carried out. The pressure fields were detected by a needle hydrophone with an active area of 4 mm in diameter (Reson GmbH, Kiel, Germany). A personal computer controlled the 3-D motion of the hydrophone and acquired the received data. The hydrophone was attached to a $x-y-z$ translation device (Time and Precision, Hampshire, UK), enabling it to be precisely positioned at specific points in the transducer field. The movement of the translation stage was automatically controlled with a personal computer using a dedicated software. The hydrophone output was connected, through a low-pass filter, to a digital oscilloscope (Model 9400A, Lecroy). The captured pressure waveforms were digitized at a sampling rate of 100 MHz, and then transferred to a personal computer for further processing. The multifrequency band transducer was driven by an ENI power amplifier (Model 2100L, ENI, MA, Rochester, USA), using a ten-cycle electrical signal delivered by an arbitrary waveform generator (Model 332505, Agilent). A low excitation level was used to avoid distortions and to ascertain the effective aperture geometry of the source. The beam profile measurements were performed across the beam, in the lateral direction, for both transmitting elements. In addition, the sensitivity as a function of the frequency was measured, for each element, at a distance of 40 mm. The procedure consisted of transmitting a narrow frequency band burst and varying the frequency while keeping the electrical driving level constant. The sensitivity was computed after normalizing the received signal from the hydrophone to the hydrophone sensitivity. The frequency was swept, with steps of 10 kHz, from 10 kHz up to 800 kHz for the HF inner element, and from 10 kHz up to 300 kHz for the LF outer element.

6B.3.2 Transducer evaluation

A block diagram, displayed in Fig. 6B.2, shows the experimental setup used to test the performances of the multifrequency transducer. The transducer was mounted in a water tank ($30 \times 30 \times 20\, cm$). A narrow band sine wave burst (7 or 10 cycles) was generated by an arbitrary waveform generator (Model 332505, Agilent) with a pulse repetition time of 100 ms. The electrical signal was then amplified by an RF Power Amplifier (Model 2100L, ENI, Rochester, USA) and its amplitude could be controlled by separate variable attenuators (355C/D, HP, Palo Alto, CA, USA). The scattered signal was received with the PVDF element. This signal was electrically tuned using a wideband amplifier (Keithley Instrument) and filtered with a pass-band filter to increase the signal to noise ratio. The RF signal was then sampled on a digital oscilloscope (Model 9400A, Lecroy) with a sampling rate of 50 MHz. The response of the bubbles was averaged over 10 signals and acquired on a personal computer for further analysis. The generated acoustic pressures were separately measured at the locations of the bubbles using a needle hydrophone, as described previously. To simulate gaseous emboli, calibrated and uniform air bubbles were generated using a “home-made” bubble maker[7]. The bubbles sizes could be externally controlled by the operator. Gaseous emboli with a diameter ranging from 160 μm down to 10 μm were studied in this work. These bubbles had a very narrow size distribution (92% lie within a $\pm 4\, \mu m$ of the mean diameter) which guarantees similar diameters between all the insonified bubbles.

6B.4 Results and discussions

6B.4.1 Transducer characteristics:

Acoustic pressure measurements were performed for both the LF outer and the HF inner elements. They are presented in Table 6B.1. It was shown in previous studies[8,9] that these pressure levels are sufficient to

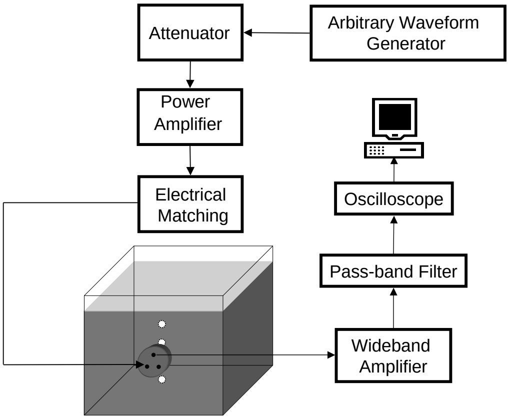

Figure 6B.2: *Drawing of the experimental acoustic setup.*

induce the bubbles into nonlinear motion and to generate harmonic components. Fig. 6B.3 shows the frequency response of both piezocomposite elements in transmission. The LF outer ring exhibits a maximum at a center frequency of 135 kHz with a bandwidth of 34% at −6 dB. The HF inner transducer shows a wider sensitivity with a center frequency around 360 kHz and a −6 dB bandwidth of 53%. Overall, the total transmitting part covers a frequency band between 100 kHz and 600 kHz which provides a wide flexibility in transmission.

		HF inner element	LF outer element
Last axial maximum (mm)		14	24
Maximal p-p pressure (kPa)	at the last axial maximum	445	355
	40mm	370	230
	75mm	245	145

Table 6B.1: *Measured maximal deliverable acoustic pressure of the LF outer element and the HF inner element at various depths: at the last axial maximum distance, at 40 mm and at 75 mm.*

The lateral beam profiles measured at 40 mm and 75 mm for the HF inner element are displayed in Fig. 6B.4. Both measurements are performed in the far field of the transducer. They show a −6 dB beamwidth of 14 mm and 23 mm, respectively, at 40 mm and 75 mm. Side lobes are noticed at approximatively 14 mm radial extent with a level of −14 dB be-

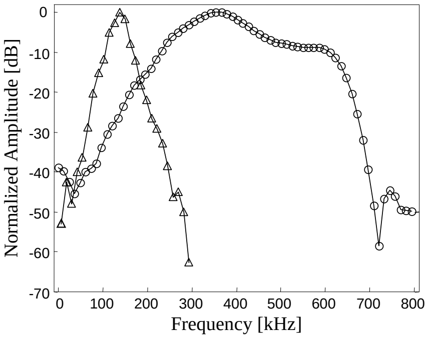

Figure 6B.3: *Measured sensitivity of the transmitting elements: HF inner element (O) and LF outer element (△).*

low the main lobe level at 40 mm whereas a side lobe at a level of −17.5 dB is created at 24 mm when the lateral profile is measured at 75 mm. Beside measurements, simulations of the beam profile were carried out using Field program[10]. The predicted profile correlates well with the measured profile and all the measured features of the beam are well reproduced by the simulations. The lateral beam profiles were also measured at 40 mm and 75 mm for the LF outer ring and they are presented in Fig. 6B.5. At 40 mm, the bandwidth at −6 dB is 18 mm but a strong side lobe appears at 24 mm at a level of -10 dB below the main lobe due to the ring geometry. At larger depth (75 mm), the same tendency can be observed: side lobes are produced at 45 mm with a level of −10 dB. The −6 dB beamwidth of the ring measures 35 mm at this depth. Simulations were also carried out for the ring transducer and good correlation is observed with the measurements. The measured beamwidths can be considered wide when compared to the ones usually encountered in the medical field. Nevertheless, it is not a limitation for our application, since this transducer was not developed for imaging purposes.

6B.4.2 Transducer evaluation for microemboli detection

The capabilities of the multifrequency band transducer were evaluated for the detection, the characterization and the sizing of gaseous emboli. Particulate emboli have not been studied on purpose. It was demonstrated in Chapter 6A, that particulate emboli are only leading to an increase of the RF signal amplitude. The frequency spectrum of a solid embolus exhibits only a peak at the transmitted frequency independently on its size and the acoustic settings used in our experiments. Therefore, the

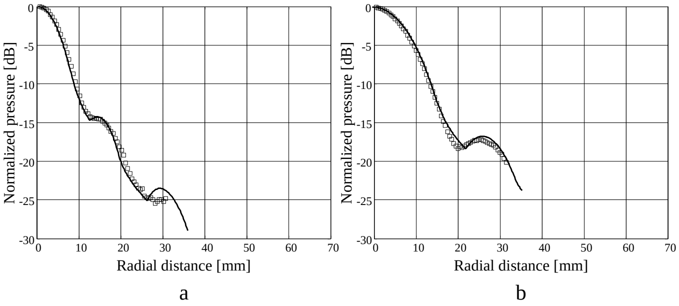

Figure 6B.4: *Simulated (solid line) and experimental (□) lateral beam profiles of the LF outer ring at 40 mm(a) and 75 mm(b).*

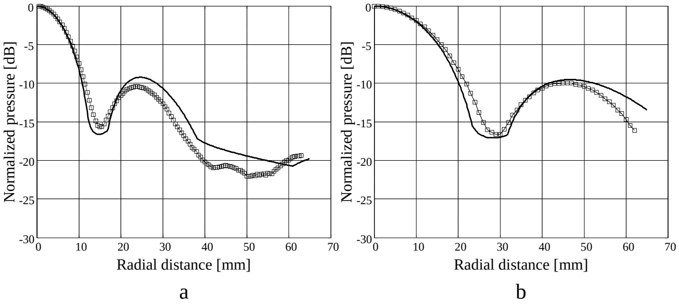

Figure 6B.5: *Simulated (solid line) and experimental (□) lateral beam profiles of the LF outer ring at 40 mm(a) and 75 mm(b).*

appearance of any harmonic components into the frequency spectrum of the RF signal backscattered by an embolus can be considered as the unique feature to classify the embolus as a gaseous particle. Indeed, we investigated the harmonic and subharmonic generation from air emboli of different sizes when interrogated with the multifrequency transducer.

Harmonic emissions:

The harmonic generation process was investigated in details using the LF outer element at its center frequency ($f_0 = 130\,\mathrm{kHz}$). The corresponding microembolus resonance size is $48\,\mu$m. The stream of bubbles was located 75 mm from the transducer's surface and irradiated with a burst of seven-cycle generating a pressure of 70 kPa. Fig. 6B.6a-d display the frequency spectrum of the backscattered RF signal received by the PVDF element, for bubbles with a diameter of $90\,\mu$m, $55\,\mu$m, $50\,\mu$m and $40\,\mu$m.

On the upper right corner of each curve, the bubble diameter is indicated by an arrow on the theoretical backscattered cross-section of an air bubble where the maximal cross-section occurs at the resonance size (D_0).

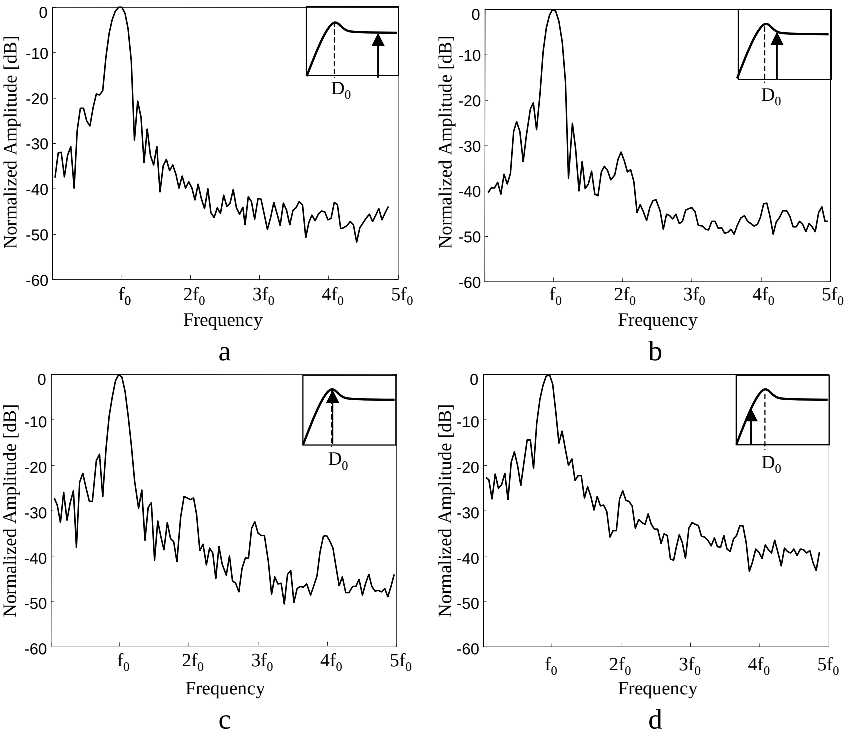

a

b

c

d

Figure 6B.6: *Simulated frequency spectra of the backscattered RF signal for different gaseous embolus sizes: a) 90 μm b) 55 μm, c) 50 μm and d) 40 μm. The LF outer ring is used as the transmitter.*

For an air embolus much larger than the resonance size, in this particular case 90 μm (Fig. 6B.6a), the frequency spectrum of the backscattered signal exhibits only a peak at the transmitted frequency f_0. Such large air emboli behave linearly and hence cannot be distinguished from other moving particles. When the bubble size gets closer to the resonance size, as shown in Fig. 6B.6b, the bubble starts vibrating nonlinearly and we can appreciate a second harmonic component 31 dB below the fundamental. Fig. 6B.6c presents the frequency spectrum of the scattered signal from a bubble with a size of 50 μm that can be assimilated to the resonance size. The spectrum clearly shows that resonant bubbles can generate a high number of harmonics: second ($2f_0$), third ($3f_0$) and fourth ($4f_0$) harmonic components. When the bubble diameter becomes smaller than the resonance size, the number of harmonic components regressively decreases and for a bubble of 40 μm, only a second harmonic is generated. For these specific scanning conditions (LF outer element, acoustic pressure of 70 kPa), gaseous emboli with a diameter between 60 μm and 40 μm generate a second harmonic component and, thus, can be correctly classified as gaseous matter. When the acoustic pressure is increased up to its maximal value (145 kPa), the range of gaseous embolus sizes leading to the production of a second harmonic component is extended from 30 μm up to 75 μm. Bubbles' sizes outside this range can be detected by looking at the increase of backscattered signal power at the fundamental frequency (f_0) but, they cannot be characterized as gaseous matter. The same observations were noticed with the HF inner transmitting element (corresponding resonance size: 17 μm). The transmitted ultrasonic burst consisted of a 10 cycles pulse generating an acoustic pressure of 130 kPa at the bubble location, 40 mm from the transducer's surface. The experimental results obtained with both elements are summarized in Table 6B.2.

Subharmonic and ultraharmonic emissions

The nonlinear behavior of air bubbles leading to the formation of subharmonic and ultraharmonic components was studied in detail in Chapter 5. It was demonstrated that gaseous emboli with a diameter corresponding to twice the resonance size produce a subharmonic at low acoustic pressure levels. In this section, we evaluate the subharmonic and ultraharmonic generation capabilities of the embolus transducer using gaseous emboli with a resonance frequency close to half the transmitted frequency. The HF inner element was set in transmission and the PVDF element in reception mode. Fig. 6B.7 displays the levels of the subharmonic ($f_0/2$) and the first ultraharmonic ($3f_0/2$) components as a function of the bubbles size. The ultrasound burst contained 10 cycles generating an acoustic pressure of 165 kPa. The stream of bubbles was located 40 mm from the transducer's surface. The curves demonstrate that for a transmitted frequency of 360 kHz, a subharmonic component can be generated for bubbles with a diameter ranging between 20 μm and 45 μm. A maximum response of both the subharmonic and the ultraharmonic was found for a gaseous embolus of 32 μm in diameter, which is slightly smaller than the theoretical value. Such a behavior was reported in Chapter 5 and it was related to an inadequacy of the theoretical resonance frequency formula when high acoustic pressure levels are used.The same curve tendency can be observed with the first ultraharmonic but the amplitude of this component is smaller than the subharmonic component. We also notice that the ultraharmonic component is spread over a wider bubble size range than the subharmonic component amplitude.

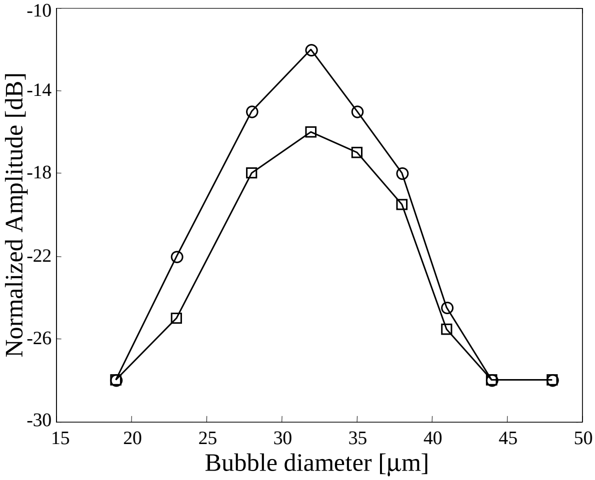

Figure 6B.7: *Subharmonic (O) and first ultraharmonic (□) level as a function of the embolus diameter using the HF inner element as the transmitter.*

Bubble sizes larger than 45 μm have shown to behave linearly at this transmitting frequency and do not generate nonlinear components. At the opposite, even though bubbles smaller than 20 μm did not show any subharmonic or ultraharmonic components at this acoustic pressure level, they could still reflect energy in the higher harmonic band (second harmonic and so on). Therefore, such bubbles can be correctly classified as gaseous emboli. The same trend of results was obtained when the LF outer element was used as the transmitter and they are summarized in Table 6B.2.

Sizing procedure

The multifrequency band transducer offers the possibility to characterize a wide range of gaseous emboli: from $10\,\mu m$ up to $105\,\mu m$. Referring to Table 6B.2, each transmitting element can classify specific gaseous embolus size ranges. Typically, for each transmitted frequency, we notice that bubbles around the resonance size generate higher harmonics whereas bubbles around twice the resonance size produce a subharmonic or an ultraharmonic component. Therefore, the order of the nonlinear component generated can be used to size the detected gaseous embolus. As an example, using the LF inner element as a transmitter, a gaseous embolus with a diameter between $\pm 20\,\mu m$ around the resonance size generates higher harmonics and a gaseous embolus with a diameter of $\pm 10\,\mu m$ around twice the resonance size produces a subharmonic component. The sizing resolution can be improved by selectively receiving the higher harmonics (>2). The number of harmonics increases as the embolus size gets closer to the resonance size. A third harmonic is only produced for bubbles very close to the resonance size whereas a fourth and fifth harmonic can only be generated for resonant bubbles.

	Second harmonic	Subharmonic
LF outer element	$30 - 75\,\mu$m	$85 - 105\,\mu$m
HF inner element	$10 - 30\,\mu$m	$22 - 44\,\mu$m

Table 6B.2: *Gaseous emboli size range leading to the formation of a second harmonic and subharmonic component as a function of the transmitting frequency: the LF outer element and the HF inner element.*

6B.5 Conclusions

The multifrequency band transducer studied in this chapter appears to have a promising potential to detect, classify and size gaseous microemboli. The detection of circulating microemboli is achieved by detecting the increase of the fundamental components as it is the case for conventional TCD methods. The classification processing is based on the nonlinear behavior of gaseous emboli: gaseous emboli can generate harmonics and/or subharmonics whereas solid particles do not. Using both the second harmonic and the subharmonic as parameters to classify the detected emboli, gaseous bubbles with a diameter between $10\,\mu$m and $105\,\mu$m could be characterized as gaseous matter. The sizing procedure is based on the type of generated nonlinear components: higher harmonics are generated by gaseous emboli with a diameter close to the resonance size whereas gaseous emboli with a diameter close to twice the resonance size are leading to subharmonic and ultraharmonic components. Typically, the accuracy of the approach in estimating the embolus size is $\pm 20\,\mu m$. A finer estimation can be realized for a limited bubble size range. Gaseous embolus with a diameter very close to the resonance ($\pm 4\,\mu m$) can be discriminated from other sizes by the production of a third and even a fourth harmonic in their frequency response.

One of the disadvantages of such a transducer design is related to the side lobe levels created by the external ring element. These side lobe levels are higher than those generated by a circular transducer and can limit the dynamic range of the transducer. However, this design presents several advantages such as the wide frequency band allowing to transmit frequencies between 100 kHz up to 600 kHz. Each element can be controlled separately and independently. Due to the wide frequency band available simultaneously in transmission and reception mode, the performance of the multifrequency transducer could be valuably improved. The large beamwidths allow a single embolus to be scanned by several discrete frequencies and, therefore, by sweeping the transmitted frequency over the complete frequency band (from 100 kHz up to 600 kHz), specific gaseous embolus size ranges could be selectively detected and sized. The main advantage of such an approach will be to enlarge the classifiable embolus size, especially for large bubbles. It is expected that a gaseous embolus of 200 μm generates nonlinear components when insonified by a frequency of 100 kHz. In addition, such a transducer could be easily adapted to operate with TCD systems.

An immediate clinical application of this embolus transducer could be to detect gaseous microemboli during cardiac surgery where it is known that a large number of gaseous emboli are produced. The transducer could be located on the extracorporeal circuit or directly on the carotid artery. Before going on clinical practice, few technical improvements of the transducer design are currently under realization to improve its efficiency both in transmission and in reception mode. In particular, a higher sensitivity of the LF outer element as well as a better signal to noise ratio would be required for *in vivo* tests.

References

1. J.L. Smith, D.H. Evans, P.R.F. Bell, and A.R. Naylor, “A comparison of four methods for distinguishing Doppler signals from gaseous and particulate emboli”, *Stroke*, vol. 29, no. 7: pp. 1133-1138, 1998.

2. H.S. Markus and M.M. Brown, “Differentiation between different pathological cerebral embolic materials using Transcranial Doppler in an *In-Vitro* model”, *Stroke*, vol. 24, no. 1: pp. 1-5, 1993.

3. D. Georgiadis, T.G. Mackay, A.W. Kelman, D.G. Grosset, D.J. Wheastley, and L. K.R., “Differentiation between gaseous and formed embolic materials *in Vivo*: application in prosthetic heart valve patients”, *Stroke*, vol. 25, no. 8: pp. 1559-1563, 1994.

4. G. Devuyst, G.A. Darbellay, J.M. Vesin, V. Kemeny, M. Ritter, D.W. Droste, C. Moline, J. Serena, R. Sztajzel, P. Ruchat, C. Lucchesi,

G. Dietler, E.B. Ringelstein, P.A. Despland, and J. Bogousslavsky, “Automatic classification of HITS into artifacts or solid or gaseous emboli by a wavelet representation combined with dual gated TCD”, *Stroke*, vol. 32, no. 12: pp. 2803-2809, 2001.

5. G.A. Darbellay, G. Devuyst, J.M. Vesin, M. Ritter, D. Droste, C. Molina, J. Serena, R. Sztatjzel, T. Karapanayiotides, E.B. Ringelstein, C. Lucchesi, J. Bogousslavsky, and P.A. Despland, “The classification of cerebral microemboli into gaseous bubbles and solid clots is not a piece of cake!!!”, *Cerebrovas Dis*, vol. 11 (Suppl 13): pp. 16, 2001.

6. D. Russell and R. Brucher, “Online automatic discrimination between solid and gaseous cerebral microemboli with the first multifrequency Transcranial Doppler”, *Stroke*, vol. 33, no. 8: pp. 1975-1980, 2002.

7. P. Palanchon, J. Klein, and N. de Jong, “Production of standardized air bubbles: application to embolism studies”, *Rev Sci Instrum*, vol. 74, no. 4: pp. 2558-2564, 2003.

8. P. Palanchon, A. Bouakaz, J.H. van Blankestein, J. Klein, N. Bom, and N. de Jong, “New technique for emboli detection and discrimination based on nonlinear characteristics of gas bubbles”, *Ultrasound Med Biol*, vol. 27, no. 6: pp. 801-808, 2001.

9. P. Palanchon, A. Bouakaz, J. Klein, and N. de Jong, “Subharmonic and ultraharmonic emissions for emboli detection and characterization”, *Ultrasound Med Biol*, vol. 29, no. 3: pp. 417-425, 2003.

10. J.A. Jensen, “Field: a program for simulating ultrasound systems”, *Ultrasound Med Biol*, vol. 34, no. 51: pp. 351-353, 1996.

Chapter 7

Ultrasonic manipulation of a gaseous embolus

Abstract

Previous studies dealing with contrast agent microbubbles have demonstrated that ultrasound (US) can significantly influence the movement of microbubbles. In this chapter, we investigate the influence of the acoustic radiation force on individual gaseous emboli using high-speed photography. We emphasize the effects of the US parameters (pulse length, acoustic pressure) on different bubble patterns and their consequences on the translational motion of the bubbles. A stream of uniform air bubbles with diameter ranging from 35 μm *to 79* μm *was generated and insonified with a single US pulse emitted at a frequency of 130 kHz. The bubble sizes were chosen to be above, below and at resonance. The peak acoustic pressures used in these experiments ranged from 40 kPa up to 120 kPa. The axial displacements of the bubbles produced by the action of the US pulse were optically recorded using a high-speed camera at 1 kHz frame rate. The experimental results were compared to a simplified force balance theoretical model including the action of the primary radiation force and the fluid drag force. Although the model is quite simple and does not take into account phenomena like bubble shape oscillations and added mass, the experimental findings agree with the theoretical predictions. The measured axial displacement increases*

Based on the publication: "Optical observations of acoustical radiation force effects on individual air bubbles" by P. Palanchon, P. Tortoli, A. Bouakaz and N. de Jong, *Accepted for publication in IEEE Transactions on Ultrasonics Ferroelectrics and Frequency Control.*

quasi-linearly with the burst length and the transmitted acoustic pressure. This displacement also varies with the size and the density of the air bubbles, reaching a maximum at the resonance size of 48 µm. The predicted displacement values differ by 15% from the measured data except for resonant bubbles where the displacement was overestimated by about 40%. This study demonstrates that even a single US pulse produces radiation forces that are strong enough to affect the bubble position.

7.1 Introduction

To obtain the desired response to ultrasound (US) by microbubbles, it is necessary to know their reaction to the different forces they experience during insonation. Among these forces, the primary, or Bjerknes, radiation force[1] may play important roles. The effect of radiation force may have been experienced in study dealing with microemboli detection. Smith et al.[2] have reported that Doppler embolic signals from gaseous emboli often display regions of frequency modulations whereas signals originated from solid emboli never exhibits such a behavior. The reason of this sudden frequency change was not really understood but it could be related to the displacement induced by the ultrasound waves.

A preliminary evaluation of radiation force effects on microbubbles has been reported by Dayton[3], who optically observed that a streamline of contrast agents was pushed away from the insonifying transducer. Experimental results have shown that when such translations are related to full populations of contrast agents suspended in moving fluids, they may yield to considerable distortions in the corresponding Doppler spectra[4–5]. A Doppler approach was used to indirectly validate a simple theoretical model, in which the microbubbles movements are evaluated through the combination of the primary US force with the drag force of the fluid in which they are suspended. Experimental spectra obtained by insonifying full populations of Levovist microbubbles were positively compared with the spectra estimated according to such a model[5]. A similar, but more accurate model was developed in reference 6. This model, which includes the added mass force and evaluates all the effects of bubble oscillations, was compared to experiments performed on individual phospholipid shelled microbubbles.

The aim of this chapter was to establish the influence of radiation forces on the response of microemboli and therefore on the corresponding Doppler signal. The effects of radiation forces associated to a single US pulse on a stream of individual gaseous emboli with a diameter ranging from 35 μm to 79 μm were evaluated qualitatively and quantitatively. The axial displacement was measured using a high-speed imaging system. The influence of the acoustic parameters as well as of the size and the density of the bubbles was investigated.

7.2 Materials and methods

Experimental set-up

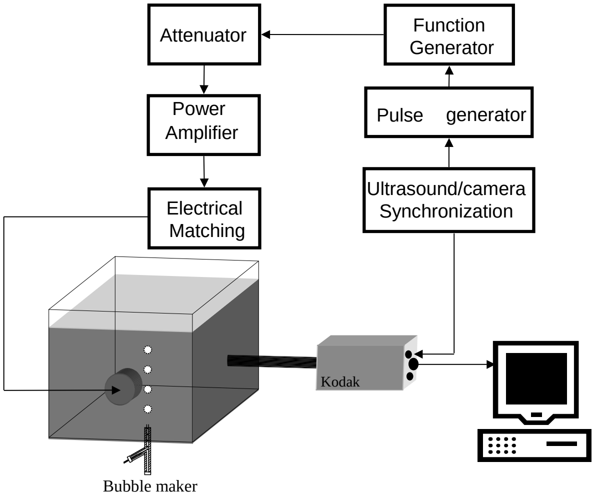

Figure 7.1: *Experimental setup.*

The experimental setup is shown in Figure 7.1. A streamline of bubbles was generated by a home made \bubble maker"[7], allowing the production of calibrated and uniform air bubbles. The operator could independently control the size and the number of the generated bubbles by varying the settings of this device. The bubble streamline was directed from the bottom to the top of the tank, as the bubbles are dragged by the movement of the flow generated by a gear pump. A single-element US transducer was positioned to produce acoustic waves directed perpendicularly to the streamline. The imaging system was composed of a high-speed camera (CR2000, Kodak) directly mounted on a long zoom microscope (Sciencescope, Chino, USA) and focused on the microbubbles. The frame rate of the camera was fixed at 1 kHz. A constant light source provided the necessary illumination for the recordings. The optical resolution of this system was 3 μm/pixel. The ultrasonic arrangement included a function generator producing a single sinusoidal burst, coherent with the camera frame synchronism and a radio-frequency power amplifier (Model 2100L, ENI, Rochester, MA, USA). A home made electrical matching circuit was used to compensate the impedance mismatch between the US transducer and the electronics. The acoustic pressure produced by the transducer could be adjusted with appropriate attenuators and was separately measured using a calibrated hydrophone (Reson GmbH, Kiel, Germany). The tip of the needle was positioned in the optical field of view, so that the measured acoustic pressure, ranging from 40 kPa to 120 kPa, corresponded to the pressure applied to the bubbles. The images taken by the high-speed camera were saved on a personal computer for analysis. The bubbles' characteristics (diameter and separation distance between two successive bubbles) as well as their displacements were computed using a MATLAB program (The MATHWORKS, Natick, MA, USA).

Simulation model

The displacement of the bubbles is predicted using a simple theoretical model similar to the one described by Tortoli[4]. It assumes that the bubble displacement is induced by the action of the primary radiation force and the drag force of the fluid. The trajectory of the bubbles can be traced by solving the following vector motion equation:

$$\vec{F_{US}}(t) + \vec{F_D}(t) = m\frac{d\vec{V_b}(t)}{dt} \tag{7.1}$$

where

$\vec{F_{US}}$	is the primary radiation force;
$\vec{F_D}$	is the drag force;
$\vec{V_b}$	is the instantaneous bubble velocity;
m	is the bubble mass.

The expression of the primary radiation force is similar to the one described by Leighton[8] and Dayton[3]. It assumes that the bubble diameter is much smaller than the acoustic wavelength, the bubble remains spherically symmetric during pressure changes and the acoustic waves are planar and parallel. When a single pulse is considered, the amplitude of the primary radiation force is expressed by:

$$\vec{F_{US}} = \frac{{P_A}^2 D}{2\rho c f}\,\frac{\delta_{tot} f_0/f}{[(f_0/f)^2 - 1]^2 + (\delta_{tot} f_0/f)^2} \tag{7.2}$$

where

f	is the transmitted frequency,
c	is the US propagation speed,
P_A	is the peak acoustic pressure,
f_0	is the resonance frequency,
D	is the equilibrium bubble diameter,
ρ	is the fluid density,
δ_{tot}	is the total damping coefficient.

The total damping coefficient and the resonance frequency are defined, respectively, by the Equations 3.3 and 3.7.

When an US pulse is applied to a moving bubble, it induces an acceleration of the bubble so that it is diverted from the flow path. The difference between the fluid and the bubble velocity yields to a drag force. Assuming that the bubble remains spherical and the surrounding fluid is Newtonian, the drag force is defined by the formula:

$$\vec{F_D} = C_D Re \frac{\pi D \nu \rho_0}{8} (\vec{V_f} - \vec{V_b}) \tag{7.3}$$

where

$\vec{V_b}$	is the instantaneous bubble velocity,
$\vec{V_f}$	is the fluid velocity,
R_e	is the Reynolds number,
C_D	is the drag coefficient,
ρ	is the fluid density,
ν	is the fluid viscosity.

Note that this equation does not include the effects of bubble radial motion in the translating bubbles. In practice, according to this model, it is expected that each bubble is accelerated along the transducer (horizontal) axial direction until it reaches a steady velocity, V_b, such that the corresponding drag force, as described by Equation 3.3, perfectly balances the radiation force. This equilibrium condition is achieved quite rapidly[3], and holds as long as the bubble is insonated by the US burst, i.e., for a time, T_X, depending on the transmitted burst length. At the end of such time interval, the displacement turns out to be: d = $V_b T_X$ (and is thus proportional to the number of transmitted cycles). Afterwards, the bubble is dragged again along the (vertical) direction of the fluid flow. Equation 7.1 was solved numerically using a simple Euler one-step method.

7.3 Results and discussions

The translation of the bubbles in the wave propagation direction was investigated following two different approaches. In a first set of measurements, the influence of US parameters such as the pulse length and the peak acoustic pressure was studied for specific bubble diameters. Secondly, the displacement induced by the radiation force was examined as a function of the bubbles' diameter and density (defined by the separation distance between two successive bubbles). Air bubbles with diameter between 35 μm to 79 μm were studied. Their rising velocity (i.e., the fluid velocity) was ranging from 200 μm/ms to 290 μm/ms. Figure 7.2 shows an example of the translational displacement produced by a single acoustic pulse composed of 10 cycles and generating an acoustic pressure of 110 kPa. Three subsequent frames spaced 1 ms apart (one taken before and two after the US pulse transmission) are overlapped in the same picture. The resting diameter of the bubbles was 48 μm. $X_{initial}$ represents the position of the bubbles before insonification and Δ is the measured displacement. It can be observed that the bubble is displaced to the right by an amount of about 165 μm and has moved up about 250 μm. The horizontal translation is consistent with the prediction of the model, while the vertical movement of the bubble is associated to the drag force of the fluid.

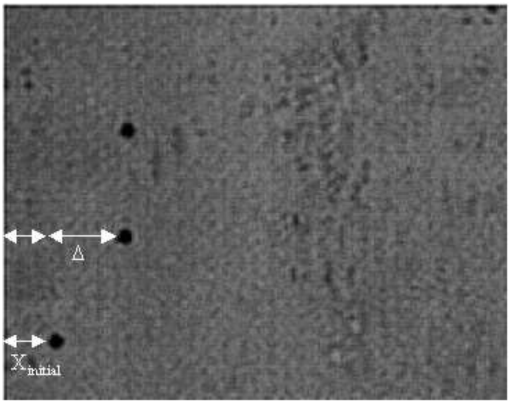

Figure 7.2: *Superposition of 3 consecutive frames showing the displacement of a 48 μm bubble induced by a ten-cycle US pulse emitting 110 kPa at 130 kHz : before the US burst and after the US burst. The vertical displacement corresponds to the 260 μm/ms fluid velocity.*

Figure 7.3 displays the measured displacement as a function of the pulse length. The number of cycles ranged from 5 to 30 cycles. The diameter of the bubbles was 48 μm and the acoustic pressure was set to 54 kPa. As expected from theory, the displacement increases linearly with the number of cycles. Figure 7.4 displays the influence of the transmitted acoustic pressure on three different bubble sizes: 62 μm (△), 55 μm (□) and 48 μm (O). The bubbles were insonified with a 10-cycle burst and the distance between two successive bubbles was kept around 1 mm. In all cases, according to the theoretical model, the combined action of radiation and drag force should produce a displacement that varies quasi-linearly with the acoustic pressure. This linear dependency between the displacement and the acoustic pressure can be noticed for the three bubble sizes, although in the case of a resonant bubble 48 μm, the growing rate differs at low and high acoustic pressure levels. We can also observe that each curve exhibits a different slope. As the bubble is closer to the resonance size 48 μm, the measured displacement increases with acoustic pressure at a much faster rate. While the three bubble diameters experience quite similar displacements at low pressure, the difference is dominant at high pressure levels. For instance, the difference between translations of 48 μm and 62 μm bubbles is only 10 μm at 48 kPa, but reaches 170 μm at 120 kPa.

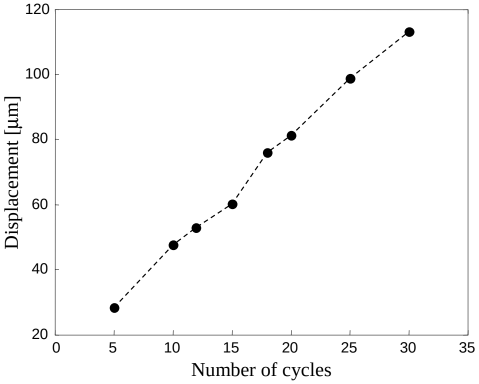

Figure 7.3: *Measured displacements for 48 μm bubbles as a function of the pulse length.*

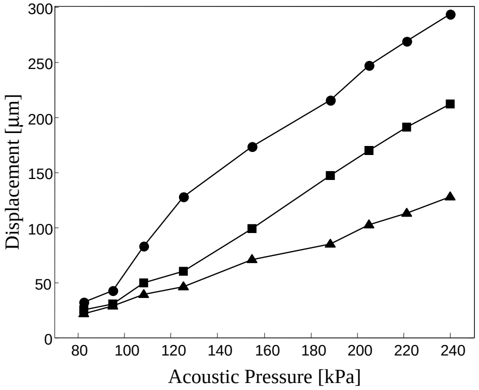

Figure 7.4: *Measured displacements as a function of the transmitted acoustic pressure for three different bubble diameters: 48 μm(O), 55 μm(□) and 62 μm(△).*

In a second set of experiments, the influence of the bubble density has been investigated by exploiting the 'bubble maker' capability of generating bubbles with various mutual distances. Figure 7.5a-c show 48 µm bubbles with three different distributions, corresponding to separation distances around (a) 200 µm, (b) 350 µm and (c) 900 µm, respectively. The displacement measured for each distribution, is displayed in Figure 7.5d as a function of the bubble diameter. The US burst consisted of 10 cycles with a peak acoustic pressure of 54 kPa. We can first observe that the change in the measured displacement depends on the bubble size. Each curve exhibits a maximum for a bubble diameter of 48 µm, which corresponds to the resonance size for a transmit frequency of 130 kHz. When the bubbles are smaller or larger than the resonance size, the displacement rapidly decreases. It can also be noticed that the measured displacement is highly dependent on the density of the bubbles.

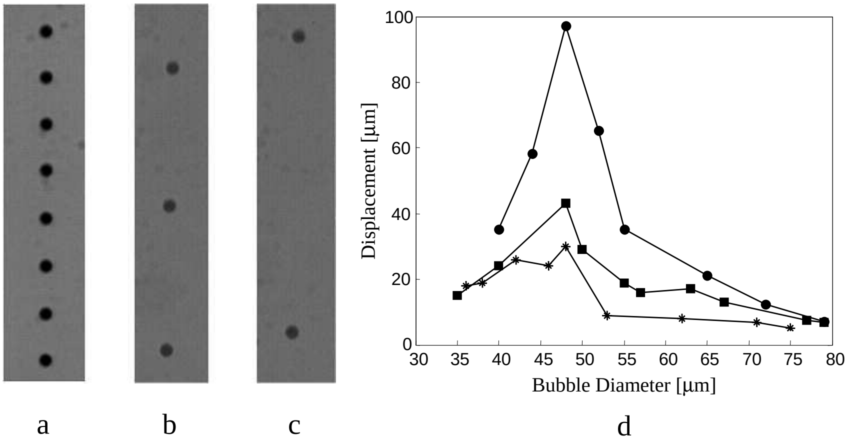

Figure 7.5: *Bubble patterns with separation distances between two successive bubbles of: a) 200 µm, b) 350 µm and c) 900 µm; d) bubble displacements as function of diameter for three different separation distances between two successive bubbles: 900 µm(O), 350 µm(□) and 200 µm(∗).*

When the separation distance between two successive bubbles decreases, the displacement induced by the US pulse is considerably reduced. The effect is dominant for bubbles around the resonance size while the difference becomes smaller for bubbles larger or smaller than the resonance size. In the case of resonant bubbles, the displacement is reduced by 56% when the separation distance between two bubbles goes down from 900 µm to 350 µm and by 70% when the separation distance is reduced to 200 µm. As the separation distance decreases, the displacement for bubbles larger than the resonance size exhibits a smaller decay. Considering the smallest distance between the bubbles, the displacement for bubbles of 53 μm and 75 μm decays only by a factor of 2 while this decay reaches a factor of 4 for the largest separation distance. This set of measurements underlines the fact that there is a strong interaction between the bubbles when they are closer to each other. Only for a large separation distance (e.g.:$>$ 900 μm), each bubble can be considered as an independent scatterer. When the number of bubbles increases, each bubble interferes with its neighboring bubbles. This interaction is mainly influenced by the secondary radiation force resulting from the pulsating bubbles. The secondary radiation force between bubbles arises when a pulsating bubble is radiating a pressure field acting on a second bubble. When bubbles with a similar diameter are considered, the secondary radiation force results in an attractive force. Therefore, it may conduct to a bubble streamline more resistant to the primary radiation force. An example of the effect of the secondary radiation force is given in Figure 7.6. The resting radius of the bubbles is 53 μm and the separation distance is 170 μm, as shown in Figure 7.6a. When a single pulse with an acoustic pressure of 110 kPa is applied to the bubbles, the bubbles flow pattern is disturbed and the bubbles are become closer as visible in Figure 7.6b.

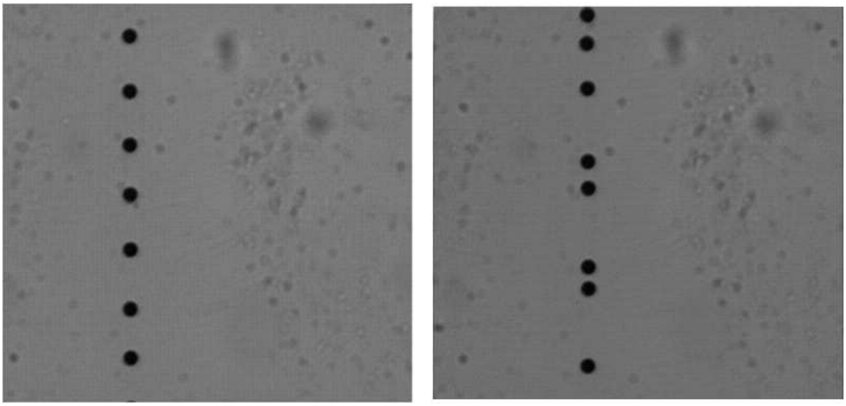

a b

Figure 7.6: *Example of the secondary radiation force effect on a streamline of microbubbles:a) before the US burst, b) after the US burst.*

The measured displacement was compared to the displacement computed from the theoretical model as a function of the bubble size. Figure 7.7 shows the simulated (O) and experimental displacements ($\Diamond$) as a function of the bubble diameter. Since the theoretical model considers the behavior of a single bubble, the largest separation distance between the bubbles was used in these experiments. A burst of 10 cycles with a pressure of 54 kPa was applied to the bubbles. Both curves present the same tendency: a maximal displacement is observed at the resonance size. For bubbles far above the resonance size, the theoretical model agrees quite well with the experiments. The difference between measured and predicted displacements is about 15%. Larger discrepancy can be observed around the resonance size, where the simulations overestimated the measurements by about 40%.

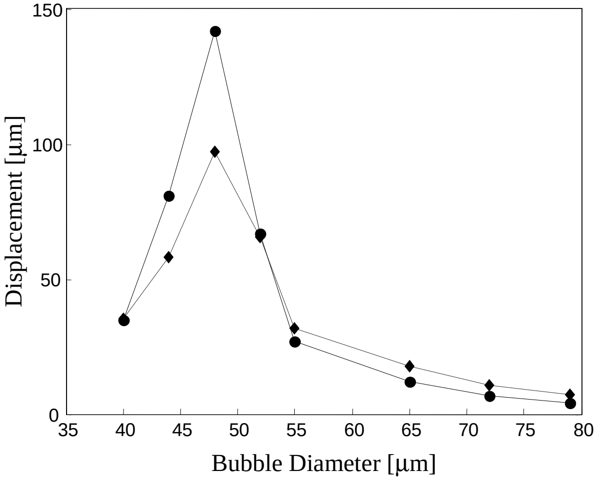

Figure 7.7: *Comparison between computed (O) and measured ($\Diamond$) bubble displacements at 55 kPa with a separation distance of 900 μm as a function of bubble diameter.*

The discrepancy between theory and measurements for resonant bubbles might be ascribed partly to measurement uncertainties and partly to an inadequate theoretical description of the bubble oscillations. Due to the strongly resonant behavior of the bubbles, a possible small difference between the measured and the actual bubble size can dramatically influence the results. Such problem was limited, although not totally eliminated, by changing the bubble diameter until a maximal displacement could be observed. Moreover, resonating free air bubbles experience very strong nonlinear expansions and contractions, while the model considers a fixed (resting) radius for the drag force and ignores possible contribution of added mass force, which is known to be relevant for highly nonlinear

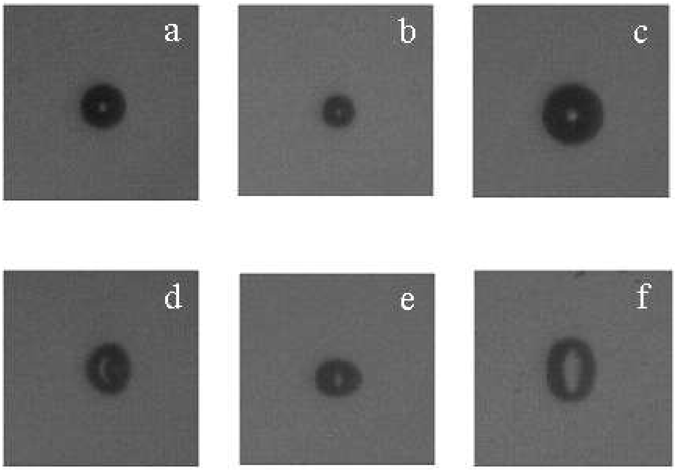

Figure 7.8: *Oscillations of a bubble with* $44\,\mu$m *diameter observed with the Brandaris 128. a)-b)-c) nonlinear bubble pulsations; d)-e)-f) non-spherical bubble vibrations.*

oscillations[10]. The discrepancies between measurements and model predictions become more evident at higher pressures. The model in fact assumes that the bubble remains spherical under ultrasonic irradiation. However, for resonant bubbles, and relatively high pressures, such assumption is no more valid. This finding was demonstrated using the ultra fast digital camera and some data are presented in Chapter 3. As an example, the oscillations induced by a 60 kPa pressure wave on a bubble of 44 μm resting radius were recorded at frame rate of 1.5 MHz and are displayed in Figure 7.8. The figure shows various frames taken during a single 6 cycles insonation burst. First three frames show the bubble at rest (Figure 7.8a), at maximal compression (Figure 7.8b) and at maximal expansion (Figure 7.8c). Figure 7.8d-f, taken during later insonation cycles, display clearly non-spherical oscillations of the bubbles. The effect was reversible and after the passage of the US burst, the bubbles recovered their initial diameter and shape Such images confirm that, even at a relatively low acoustic pressure, the bubble shape does not remain spherical anymore and new surface vibration modes are generated.

7.4 Conclusions

In this chapter, the effects of the acoustic radiation force on the bubble translation were investigated as a function of the bubble characteristics and the US parameters. As expected by theory, the bubble displacement increases linearly with both the burst length and the transmitted acoustic pressure. The displacement is strongly correlated to the bubble diameter as well as to the separation distance between two bubbles. It has been demonstrated that, independently of the US settings, bubbles at the resonance size lead to a maximal displacement while other bubble sizes produce lower but non-negligible displacements. The density of the bubbles also affects considerably the measured displacement. For high bubble concentration, the displacement induced by the US force strongly decreases. This may be related to the effect of secondary radiation force, which seems to have a limiting effect similar to that of the drag force. The theoretical model here shows a good overall agreement with the experiments, both qualitatively and quantitatively. Only around the resonance size, the simulations appreciably overestimate the displacement. This is probably due to the fact that the model neglects the bubble size oscillations that are relevant in the case of large free air bubbles like those used in this work. At relatively high pressure levels, the behavior of free air bubbles is quite complex, as observed with an ultra fast digital camera, and therefore the simplified theoretical model may be not accurate enough. A more complex model including the effect of bubble oscillations on the drag force as well the added mass force would be more suitable in this regime. Overall, this study has demonstrated that even a single US pulse may disturb considerably a flow path of individual air bubbles and consequently its shape and its response.

References

1. V.F.K. Bjerknes, "Fields of force", New York: Columbia University Press, 1906.

2. J.L. Smith, D.H. Evans, and A.R. Naylor, "Analysis of the frequency modulation present in Doppler ultrasound signals may allow differentiation between particulate and gaseous cerebral emboli", *Ultrasound Med Biol*, vol. 23, no. 5: pp. 727-734, 1997.

3. P.A. Dayton, K.E. Morgan, A.L. Klibanov, G. Brandenburger, K.R. Nightingale, and K.W. Ferrara, "A preliminary evaluation of the ef-

fects of primary and secondary radiation forces on acoustic contrast agents", *IEEE Trans Ultrason Ferr Freq Con*, vol. 44, no. 6: pp. 1264-1277, 1997.

4. P. Tortoli, M. Pratesi, and V. Michelassi, \Doppler spectra from contrast agents crossing an ultrasound field", *IEEE Trans Ultrason Ferr Freq Con*, vol. 47, no. 3: pp. 716-726, 2000.
5. P. Tortoli, V. Michelassi, M. Corsi, R. D., and Y. Takeushi, \On the interaction between ultrasound and contrast agents during Doppler investigations", *Ultrasound Med Biol*, vol. 27, no. 9: pp. 1265-1273, 2001.
6. P.A. Dayton, J.S. Allen, and K.W. Ferrara, \The magnitude of radiation force on ultrasound contrast agents", *J Acoust Soc Am*, vol. 112, no. 5: pp. 2183-2192, 2002.
7. P. Palanchon, J. Klein, and N. de Jong, \Production of standardized air bubbles: application to embolism studies", *Rev Sci Instrum*, vol. 74, no. 4: pp. 2558-2564, 2003.
8. T.G. Leighton, \The Acoustic Bubble", London Academic Press Limited, 1994.
9. H. Medwin, \Counting bubbles acoustically: a review", *Ultrasonics*, vol. 15, no. 1: pp. 7-13, 1977.
10. T.J. Matula, \Bubble levitation and translation under single bubble sonoluminescence conditions", *J Acoust Soc Am*, vol. 114, no. 2: pp. 775-781, 2003.
11. C.T. Chin, C. Lance, J. Borsboom, F. Mastik, M.E. Frijlink, N. de Jong, M. Verslluis, and D. Lhose, \Brandaris 128: a digital 25 million frames per second camera with 128 highly sensitive frames", *Rev Sci Instrum*, vol. 74, no. 12: pp. 5026-5034, 2003.

Chapter 8

Summary and conclusions

8.1 Introduction

The ultrasound community has experienced dramatic technical advances over the last decades, such as blood flow measurements with elaborate Doppler techniques or real time three-dimensional imaging with 2-D phased array transducers. This was partly ascribed to the advantages of ultrasound over other diagnostic modalities, including its low cost, real-time character and safety.
One of these recent ultrasound technologies is Transcranial Doppler (TCD). TCD is a non-invasive ultrasound method used to assess blood flow velocity in the major basal intracranial arteries on a real time basis. Since the early 60's, experimental studies have been carried out to evaluate the ability of TCD to detect, quantify and classify intracranial emboli. Many research centers have investigated the appearance of high intensity transient signals in the TCD waveform as indicators of circulating microemboli, in a wide variety of clinical areas: cardiac and carotid surgery[1,2], following prosthetic heart valve insertion[3], cerebral angiography[4], atrial fibrillation[5] and decompression sickness[6]. Many reports have emphasized the ability of TCD, combined to sophisticated signal processing techniques, to identify microemboli in the brain circulation. Unfortunately, this technology presents some limitations to distinguish between emboli and artefacts[7−11] and more importantly to determine the embolus composition[12−14]. Therefore, the accuracy and clinical significance of the TCD technique for emboli classification has not yet been scientifically established. Further research is currently undergoing to implement an on-line automated embolus detection and classification method in clinical routine[15−17].

8.2 Nonlinear scattering

This thesis has investigated a novel approach to detect, quantify and classify microemboli using ultrasound. It was demonstrated through various experimental and theoretical studies that the acoustic signatures of gas particles, solid particles and tissues are different from each other. The first difference between these scattering structures occurs at the main transmit (fundamental) frequency, basis of TCD emboli detection methods. Even though the scattering capability of a gaseous embolus is usually stronger than solid particulate, their discrimination based on their responses at the fundamental frequency is very delicate. The main difference between scattering properties of solid and gaseous emboli occurs in their nonlinear regime, known as harmonics. Gaseous emboli due to their extremely high compressibility can enter into natural resonance scattering ultrasound energy not only at the fundamental frequency but also at harmonics of the fundamental frequency $2f_0, 3f_0$, etc. Beside these harmonic frequencies, subharmonic ($1/2f_0$) and ultraharmonic ($3/2f_0, 5/2f_0$, etc) components might also be generated. All these nonlinear frequency components can only be attributed to gas particles and cannot be generated by solid emboli. Moreover, harmonic frequency generation depends not only on the transmitted frequency and acoustic pressure, but also on the size of the gaseous embolus. This size-harmonic relationship gives a real opportunity to size gaseous emboli using harmonic ultrasound.

Chapter 2 describes in details a technical device to generate controllable gas microbubbles, used to simulate gaseous emboli. Such a device is of extreme importance to conduct acoustic measurements and elaborate new ultrasonic methods to detect and classify microemboli. The "bubble maker" relies on a glass micropipette connected to an air pressure source. The bubbles are carried away by a liquid flowpath crossing the micropipette tip. By adjusting the settings of the device, air bubbles can be produced with various sizes and densities. Typically the size of generated microbubbles ranges from $10\,\mu$m to $300\,\mu$m, a size within the same range as clinically encountered emboli sizes.

Chapter 3 evaluates a theoretical model based on a modified Rayleigh-Plesset equation that predicts the dynamics and acoustic response of a gaseous embolus. To do so, a high speed camera (BRANDARIS128) was used to observe the oscillations of individual gaseous embolus under ultrasound insonification. The experimental findings were compared to theoretical predictions and showed satisfactory agreements. The model is hence used to assess the acoustic properties of gaseous emboli and serves as the theoretical basis to investigate the performances of a new detection and classification method.

Chapter 4 demonstrates that gaseous emboli exposed to low frequency transmission signals generate second and higher harmonics depending on their initial diameter. Solid emboli do not oscillate and reflect the acoustic energy passively at the transmitted fundamental frequency. Therefore any harmonic component detected in the scattered emboli signal indicates the presence of gaseous emboli and discards the presence of solid emboli. Measurements and simulations showed that the generation of higher harmonic frequencies ($2^{nd}, 3^{rd}, 4^{th}, 5^{th}$) is ascribed to gaseous emboli with sizes close to the resonance size where the highest harmonic component is associated only with resonant gaseous emboli. Based on these findings, it is suggested to use the second harmonic to attest the presence of gaseous emboli and the higher harmonics to give indication of their size. With the frequencies used in our experimental setup (130 kHz and 250 kHz), only gaseous emboli with a diameter between $19\,\mu$m and $62\,\mu$m were detected. In order to enlarge the range of detectable emboli sizes, it was proposed, in Chapter

5, to focus on the subharmonic and the first ultraharmonic components. These frequency components occur at $1/2f_0$ and $3/2f_0$, and are exclusively generated by gaseous emboli with a size close to twice the resonance size, widening by that the range of detectable bubble diameters. By performing *in-vitro* acoustic experiments and modelling, it was established that these harmonic components are very sensitive to the size of the gaseous embolus. With selective reception of subharmonic and ultraharmonic, emboli with a diameter ranging from 65 μm to 110 μm could be detected at frequencies of 65 kHz and 195 kHz using an ultrasound waveform of 130 kHz in transmission. As a conclusion the combination of second and higher harmonics, subharmonic and ultraharmonic, gaseous microemboli with size extending from 19 μm to 110 μm can be correctly classified and sized.

8.3 Embolus transducer

This new harmonic classification approach requires an ultrasound technology different from the current TCD detection systems. Simulations and measurements showed that frequencies used in transmission should be close to the resonance frequency of clinically known gaseous emboli, and thus should be much lower than frequencies conventionally used in the medical field. TCD transducers operate in the MHz range ($2 - 2.5$ MHz) and, hence, cannot generate the required acoustic energy at this low frequency band. Second, received frequencies within the harmonic band also differ from TCD received frequencies. Last, the frequency bandwidth of received signal (including various harmonic components) is wider and cannot be covered by current TCD transducer technology. All these requirements have instigated the use of a new generation of emboli transducers. The "Embolus Transducer" should be able to transmit in the low frequency band and receive multiple high frequencies over a wide frequency band.

Chapter 6 of the thesis describes two transducer designs where the second prototype can be considered as an improved version of the first one. Basically, the new transducer for emboli detection and classification is composed of 2 transmit elements, where both elements have different center frequency. The prototype has center frequencies of 130 kHz and 360 kHz. In order to receive subharmonic, harmonics and ultraharmonic of gaseous emboli, the receive transducer should operate with a high sensitivity over a wide frequency band: from 50 kHz up to a few MHz. With currently available transducer technology, PVDF based elements represent a judicious choice. A layer of PVDF was added on top of both transmitting elements and used in receive mode only. The performances of this transducer for emboli detection and classification were assessed in an *in vitro* setup. Although the tests are preliminary, the obtained results demonstrate the feasibility of this novel harmonic approach combined with the new emboli transducer in detecting, classifying and sizing a wide range of gaseous emboli.

8.4 Ultrasound manipulation of a gaseous embolus

In the last Chapter of the thesis, the mechanical influences of ultrasound waves on flowing gaseous microbubbles were investigated experimentally. The purpose of this study was to establish any direct influence of ultrasound waves on the movement and behavior of the microbubbles and by that on their Doppler response. The interaction between ultrasound waves and flowing microbubbles was recorded optically and showed that strong radiation forces are applied on the microbubbles deforming by that their initial trajectory. In addition, it was observed that with adequate ultrasonic interrogation conditions, the microbubbles undergo strong distortion and fragmentation. Although demonstrated in a controlled experimental environment, such a consequence can be used to destroy or break a gaseous embolus into smaller fragments, reducing or eliminating by that its clinical consequences.

8.5 General discussion and future directions

Embolus transducer: Current TCD transducers were designed to assess blood flow velocity and therefore were optimized for this task. The preliminary *in vitro* results appear promising and thus encourage to continue further developments of the Embolus Transducer. Although it was tested with a method based on RF signal processing, it could also operate in a Doppler-like mode to take benefit of the advantages of both methods. The nonlinear properties of gaseous microemboli are not exploited in current TCD processing. Our conviction is that they bring real opportunities for microemboli classification and should be also used in combination with Doppler processing to improve the detection and discrimination rate. The emboli transducer operating at low frequency (less than 500 kHz) may present some advantages over the common TCD probes, resulting in a better microembolic signal detection. The signal to background noise ratio is expected to increase when lower frequencies are used in transmission. Furthermore, lower frequencies lead to a better skull penetration, improving by that the identification of the cerebral arteries. Previous studies using a 1 MHz TCD probe demonstrated the improvement of the embolic signal detection[18] as well as the reduction of patient presenting absent or insufficient temporal bone windows[19]. The current emboli transducer design still requires further improvements. The preliminary results have shown some limitations in both transmission and reception modes. For instance, the low frequency outer element generates insufficient acoustic pressures, which reduces the generation of the subharmonic component. Furthermore, the electronics used to match the impedance between the different elements of the transducer and the experimental instrumentation conduct to a decrease of the signal to noise ratio, reducing the detection sensitivity. Technical improvements are currently under realization.

Harmonic emboli classification and sizing: The literature reports many studies describing new processing strategies used to detect and classify gaseous and solid microparticles using TCD techniques. The radiofrequency information has been filtered out and only Doppler information is remaining. Nonlinear properties of gaseous emboli could be exploited in this area and combined to some sophisticated signal analysis to provide more efficient methods of emboli detection and classification. This thesis presents the basis of a classification and sizing system based on harmonic ultrasound. The classification part is based on the appearance of nonlinear components into the frequency spectrum of the backscattered RF signal and is directly correlated to the presence of a gaseous embolus. Meanwhile, the sizing procedure is performed by selective harmonic component type: higher harmonics (from the 2^{nd} harmonic) are correlated to gaseous emboli with a diameter close to the resonance diameter of the insonated frequency. Subharmonic and/or ultraharmonic give evidence of gaseous emboli with a diameter close to twice the resonance diameter of the insonated frequency. This approach offers the possibility to estimate gaseous emboli diameters with a deviation of $\pm 20\,\mu m$.

Future directions: The immediate extension of the work presented in this thesis include the study of an improved version of the emboli transducer in animal experiments as well as in clinical situations. The embolus transducer could be used either in extracorporeal circuits or directly applied on the carotid artery. A TCD instrument may be used conjointly to ensure the correct positioning of the transducer in respect to the blood flow as well as to validate the emboli detection performed by the emboli transducer.

A second approach of the embolism problem would be to exploit the direct action of the ultrasound burst on a gaseous embolus. As reported in Chapters 3 and 7, under specific ultrasound scanning conditions, gaseous emboli are undergoing strong shape distortions and they can even break apart. This property can be used to destroy gaseous emboli. Further investigations are required to specify the ideal ultrasonic conditions in terms of frequency, acoustic pressure, burst length and pulse repetition rate. The results presented in this thesis show that an eight-cycles single burst transmitted at frequency of 130 kHz is sufficient to break microbubbles between 80 μm and 225 μm into smaller bubble fragments, rendering them less harmful.

References

1. W. Pugsley, L. Klinger, C. Paschalis, T. Treasure, M. Harrison, and S. Newman, “The impact of microemboli during cardiopulmonary bypass on neuropsychological functioning”, *Stroke*, vol. 25, no. 7: pp. 1393-1399, 1994.

2. R.G.A. Ackerstaff, C. Jansen, and F.L. Moll, “Carotid endarterectomy and intraoperative emboli detection”, *Echocardiography*, vol. 13, no. 5: pp. 543-550, 1996.

3. D. Georgiadis, D. Grosset, A. Kelman, A. Faichney, and K.R. Lees, “Prevalence and characteristics of intracranial microemboli signals in patients with different types of prosthetic cardiac valves”, *Stroke*, vol. 25, no. 11: pp. 587-592, 1994.

4. H.S. Markus, A. Loh, D. Israel, T. Buckenham, A. Clifton, and M.M. Brown, “Microscopic air embolism during cerebral angiography and strategies for its avoidance”, *The Lancet*, vol. 341, no.: pp. 784-787, 1993.

5. C.H. Tegeler, L.P. Hitchings, M. Eicke, J. Leighton, R.K. Fredericks, T.R. Downes, D.A. Stump, and G.L. Burke, “Microemboli detection in stroke associated with atrial fibrillation”, *J Cardiovasc Tech*, vol. 9: pp. 283-284, 1990.

6. B.A. Hills and B.D. Butler, “Size distribution of intravascular air emboli produced by decompression”, *Undersea Biomed Res*, vol. 8, no. 3: pp. 163-170, 1981.

7. J. Molloy and H.S. Markus, “Multigated Doppler ultrasound in the detection of emboli in a flow model and emboli signals in patients”, *Stroke*, vol. 27, no. 9: pp. 1548-1552, 1996.

8. E.V. van Zuilen, W.H. Mess, C. Jansen, I. van Der Twell, J. van Gijn, and R.G.A. Ackerstaff, “Automatic embolus detection compared with human experts”, *Stroke*, vol. 27, no. 10: pp. 1840-1843, 1996.

9. M. Cullinane, G. Reid, R. Dittrich, Z. Kaposzta, R.G.A. Ackerstaff, V. Babikian, D.W. Droste, D. Grosset, M. Siebler, L. Valton, and

H.S. Markus, “Evaluation of new online automated embolic signal detection algorithm including comparison with panel of international experts”, *Stroke*, vol. 31, no. 6: pp. 1335-1341, 2000.

10. L. Fan, D. Evans, and A. Naylor, “Automated embolus identification using a rule-based expert system”, *Ultrasound Med Biol*, vol. 27, no. 8: pp. 1065-1077, 2001.

11. N. Aydin, S. Padayache, and H.S. Markus, “The use of the wavelet transform to describe embolic signals”, *Ultrasound Med Biol*, vol. 6, no.: pp. 953-958, 1999.

12. G. Devuyst, G.A. Darbellay, J.M. Vesin, V. Kemeny, M. Ritter, D.W. Droste, C. Moline, J. Serena, R. Sztajzel, P. Ruchat, C. Lucchesi, G. Dietler, E.B. Ringelstein, P.A. Despland, and J. Bogousslavsky, “Automatic classification of HITS into artifacts or solid or gaseous emboli by a wavelet representation combined with dual gated TCD”, *Stroke*, vol. 32, no. 12: pp. 2803-2809, 2001.

13. D. Russell and R. Brucher, “Online automatic discrimination between solid and gaseous cerebral microemboli with the first multifrequency Transcranial Doppler”, *Stroke*, vol. 33, no. 8: pp. 1975-1980, 2002.

14. J.L. Smith, D.H. Evans, P.R.F. Bell, and A.R. Naylor, “A comparison of four methods for distinguishing Doppler signals from gaseous and particulate emboli”, *Stroke*, vol. 29, no. 7: pp. 1133-1138, 1998.

15. M. Cullinane, Z. Kaposzta, S. Reihill, and H.S. Markus, “Online automated detection of cerebral embolic signals from a variety of embolic sources”, *Ultrasound Med Biol*, vol. 28, no. 10, pp. 1271-1277, 2002.

16. A.G. Munts, W.H. Mess, E.F. Bruggemans, L. Walda, and R.G.A. Ackerstaff, “Feasibility and reliability of on-line automated microemboli detection after carotid endarterectomy. A Transcranial Doppler study”, *Eur J Vasc Endovasc Surg*, vol. 25, no. 3, pp. 262-266, 2003.

17. L. Fan, D.H. Evans, A.R. Naylor, and P. Tortoli, “Real-time identification and archiving of micro-embolic Doppler signals using a knowledge-based DSP system”, *Med Biol Eng Comput*, vol. 42, no. 2, pp. 193-200, 2004.

18. M. Cullinane and S.H. Markus, “Evaluation of 1 MHz transducer for Transcranial Doppler ultrasound including embolic signal detection”, *Ultrasound Med Biol*, vol. 27, no. 6: pp. 785-800, 2001.

19. C. Klotzsch, O. Popescu, and P. Berlit, “A new 1 MHz probe for Transcranial Doppler sonography in patients with inadequate temporal bone windows”, *Ultrasound Med Biol*, vol. 24, no. 1: pp. 101-103, 1998.

Samenvatting

Medisch ultrageluid heeft de laatste tientallen jaren grote vooruitgang geboekt als gevolg van technische vernieuwingen. Voorbeelden hiervan zijn hoogfrequent toepassingen en het meten van de snelheid van bloed door middel van geavanceerde Doppler technieken. Een van deze technieken die grote vooruitgang heeft geboekt is Transcranile Doppler (TCD). TCD is een niet-invasieve methode om de bloedstroom in de hersenarterin te meten. Dit gebeurt "real-time". Verschillende studies hebben sinds begin jaren zestig TCD gebruikt om embolin in de hersenen te detecteren, te kwantificeren en te classificeren. Een tijdelijke, maar zeer expliciete verhoging van het TCD-signaal werd gebruikt als indicator voor embolin. Deze embolin kunnen ontstaan na een kunstklep- of carotis-operatie, nadat een angioscan van de hersenen is gemaakt, bij atriumfibrilatie of bij diepzee duiken. Talrijke artikelen beschrijven het gebruik van TCD, inclusief het gebruik van geavanceerde signaal bewerking, om embolin in de hersenen te identificeren. Toch heeft het gebruik van deze techniek een tweetal serieuze beperkingen. Enerzijds om embolin te onderscheiden van artifacts (signaalveranderingen die lijken op een embolie, maar die geen embolie blijkt te zijn) en te bepalen of een embolie een gasbel is of dat het bestaat uit een vetbolletje, geklonterd bloed of ander materiaal (deeltjesembolie).

Dit proefschrift beschrijft een nieuwe methode om embolin te klassificeren en te kwantificeren m.b.v. ultrageluid. Theoretische studies en experimenten, beschreven in dit proefschrift hebben aangetoond dat de ultrageluidseigenschappen van gasembolin verschilt met die van vaste deeltjes en dat van weefsel. Dit is reeds het geval voor de reflecties van fundamentele frequentie, die feitelijk de basis is voor het TCD-signaal. De intensiteit van de reflectie van een gasembolie is gewoonlijk veel hoger van die van een deeltjesembolie, maar desalniettemin blijft een techniek gebaseerd op dit intensiteit-verschil zeer delicaat. Het belangrijkste verschil tussen gas- en een deeltjesembolie is hun lineaire gedrag als ze aangestraald worden door ultrageluid, resulterend in boventonen (harmonische) in de reflectie. Gasembolin, onder invloed van ultrageluid, vertonen bovendien een resonant gedrag, vergelijkbaar met een massa-veer systeem. De compressibiliteit van het gas in de bel is dan het analagon voor de veerconstante. De vloeistof rondom de bel is analagon voor de massa. Zo'n systeem trilt naast de fundamentele ook in zijn harmonische $(2f_0, 3f_0, etc...)$, maar ook op de subharmonische $(1/2f_0)$ en ultraharmonische $(3/2f_0, 5/2f_0, etc...)$. Deeltjesembolin vertonen al. deze harmonische en subharmonische niet. De amplitude van deze harmonische, in geval van een gasembolie hangt niet alleen af van de uitgestraalde frequentie en amplitude van het ultrageluid, maar ook van de grootte van de gasembolie. Het gebruik van deze afhankelijkheid (harmonische en grootte) is een ideale mogelijkheid om de grootte van gasembolin m.b.v. ultrageluid op te meten.

Hoofdstuk 2 beschrijft in detail het apparaat waarmee microbellen, die vergelijkbaar zijn met de gasembolin kunnen worden gemaakt. Zo'n apparaat is uiterst belangrijk daar hiermee op een gecontroleerde en reproduceerbare wijze studies kunnen worden uitgevoerd om gasembolin te klassificeren. De bellenmaker bestaat uit een micropipet waardoor lucht met een instelbare druk wordt geblazen. Langs het uiteinde van de micropipet stroomt water en deze neemt de luchtbel die aan het einde van de pipet ontstaat mee in de vloeistofstroom. Door de luchtdruk en de snelheid van het water te variren kunnen bellen van verschillende grootte en concentratie gemaakt worden. Op deze manier kunnen belgrootte tussen de 10 en 300 μmm worden gemaakt. Dit is dezelfde range als die van de gasembolin die in de klinische praktijk voorkomen.

In hoofdstuk 3 wordt een theoretisch model gepresenteerd dat is gebaseerd op de Rayleigh-Plesset vergelijking. Met dit model is het dynamisch gedrag en daarbij het ultrageluidveld van een gasembolie te berekenen als het door ultrageluid wordt aangestraald. De experimenten zijn in goede overeenstemming met de theoretische resultaten. Het theoretische model is gebruikt om de akoestische eigenschappen van gasembolin te voorspellen en om nieuwe detectie en klassificatie strategien te testen.

In hoofdstuk 4 wordt aangetoond dat gasembolin, afhankelijk van hun grootte, en aangestraald met laagfrequentie ultrageluid, 2^{nd} en hogere harmonische afstralen. Deeltjes-embolin vertonen geen volumetrillingen, zoals gasembolin en reflecteren (terugstralen) hierdoor alleen maar de fundamentele, ingestraalde frequentie. Dus, harmonische componenten in het gereflecteerde signaal geeft de aanwezigheid aan van gasembolin en sluit hierbij deeltjesembolin uit. Metingen en simulaties tonen aan dat hogere harmonische $(2^{nd}, 3^{rd}, 4^{th}, 5^{th})$ veroorzaakt worden door gasembolin met een grootte dichtbij de resonantie grootte. M.a.w. de hogere harmonische componenten treden alleen op voor resonante bellen. De 2^{nd} harmonische kan gebruikt worden om de aanwezigheid van bellen aan te tonen en de hogere harmonische om de grootte te bepalen. Doordat in de experimenten 130 kHz en 250 kHz werd gebruikt konden alleen maar embolin tussen 19 en 62 μm worden opgemeten.

Om een groter bereik te kunnen meten, wordt in hoofdstuk 5 de methode uitgebreid naar de sub- en ultraharmonische. Dit zijn de componenten op $1/2f_0$ en $3/2f_0$ en worden alleen afgestraald door bellen die een grootte hebben gelijk aan tweemaal de resonatiegrootte. Zowel de experimenten, als het theoretische model bevestigen dat de sub- en ultraharmonische een zeer goede indicator is voor de belgrootte. Gasembolin varirend van 65 en 110 μm konden worden gemeten m.b.v. de sub- en ultraharmonische, zijnde 65 en 195 kHz indien een aanstraalfrequentie wordt gebruikt van 130 kHz. Dus als de sub- en ultraharmonische in combinatie met de tweede en hogere harmonische wordt toegepast, dan kunnen gasembolin, varirend van 19-110 μm worden opgemeten. Deze nieuwe methode van detecteren en klassificeren kan niet met een huidige TCD-machine, maar vereist een compleet nieuw systeem. Zowel de simulaties als de experimenten laten zien dat de ingestraalde ultrageluidfrequentie nabij de resonatiefrequentie (100 - 500 kHz) van de gasembolin moet liggen. Dit houdt aanzienlijk lagere frequenties in dan normaal worden gebruikt in de medisch ultrageluid diagnostiek. TCD-transducers hebben een frequentie van 2 MHz en zijn derhalve niet geschikt om ultrageluid uit te zenden met frequenties tussen de 100 en 500 kHz. Verder kunnen de harmonische frequenties ook niet worden ontvangen door een TCD-transducer en bovendien is de bandbreedte van een TCD te beperkt om alle harmonische berhaupt te kunnen ontvangen. Een ideale transducer voor emboliedetectie moet derhalve verschillende frequenties uitzenden in de 100 kHz range en is in ontvangst gevoelig voor de harmonische.

Hoofdstuk 6 beschrijft 2 nieuwe "embolie-transducers" waarbij de tweede een verbeterde versie is van de eerste. De nieuwe transducer bestaat uit 2 ringen, waarbij de binnenring een frequentie heeft van 360 kHz en de buitenring van 130 kHz. Deze 2 ringen worden gebruikt in zenden. In ontvangst dienen zowel de sub-, als ook de ultra- en higherharmonisch te worden ontvangen. Dit betekent een frequentieband tussen 50 kHz en 1 MHz en het gebruik van PVDF-materiaal is dan een logische en gerechtvaardigde keuze. Een PVDF-laag is bovenop de 2 ringen gemonteerd en wordt als ontvanger gebruikt. Deze nieuwe transducer is in vitro getest. Alhoewel de resultaten nog een voorlopig karakter hebben, tonen deze wel de potentie aan om met n transducer een grote variteit aan gasembolin te kunnen detecteren en te classificeren.

In het laatste hoofdstuk wordt de stralingsdruk die de bellen ondervinden experimenteel bestudeerd. Deze stralingsdruk veroorzaakt een verplaatsing van de bellen die van invloed kunnen zijn op het Doppler signaal. Optische opnamen m.b.v. een lange-afstands microscoop en een snelle camera tonen aan dat deze verplaatsing significant is en dat hierdoor het bellentraject verstoord wordt.

Dankwoord

A Ph. D. thesis is linked to only one author but it could not have been done without the contribution of many people.

Prof. J. Klein, as one of my promotors, I really thank you for you support as a clinician to better harmonize my research with the clinical field. Your enthusiasm about this 'technical' project was extremely encouraging.

Prof N. de Jong, you have always guided my research with constructive advices and judicious comments. Thanks for giving me the opportunity to obtain a Ph. D. in such a world-famous lab. I hope I was able to catch some of your scientific skills in default of the Dutch language.

Prof. K. Bom and Prof. van der Steen, I am very honored to graduate from your lab. Working with you was inspiring. I am grateful for your constant encouragement and interest to this challenging project.

Dr. Piero Tortoli, it was a pleasure to discuss about Doppler and bubbles and I enjoyed working with you. Ammiro altrettanto le vostre competenze scientifiche che le vostre grande qualità umane.

Charles Lancée, it is always very compelling to talk with you about everything but also transducers. Your contribution to the design of the embolus transducer was very helpful.

Jan Honkoop, I greatly acknowledge your support for solving all the electronic troubles. Thanks for your time and your patience for explaining electronics. I hope you won't be so anxious anymore when I start soldering again.

Leo Bekkering and Wim van Alphen, thanks for all the technical developments. Special thanks to Leo for all the extra work you and for these nice 'Ph. D. studentproof' devices you built. Cees Pakvis, thanks for helping in setting up the Brandaris camera experiments and for the wonderful drawings you made for this thesis. I would be pleased to be one of your sponsors for the coming "Tour de France".

Writing a thesis in a language that is not your mother tongue is not an easy task. So, my sincere thanks go to Dave Goertz, Charles Lancée and Ayache Bouakaz for spending extra time reviewing the chapters of this thesis. Special thanks to Michiel Postema and Fons Laan for their help in solving my incessant LaTeX troubles.

I sincerely thank Mieke Pruijsten for her assistance in preparing my Ph. D. official documents and Riekje Daane for her unconditional cheerfulness and contagious giggles. I do not forget the help of Corrie Eefting when I started my Ph. D..

Martijn Frijlink, Marco Voormolen, Egon Merks, Antoinette ten Have, Roland van Lindt, Ester Vlaanderen, also named the “Expecho Bulls”, sure you will never win the volley ball tournament but you are definitively the best working team of Erasmus. Fritz Mastik, thanks for your help in fixing the software problems and you will always be welcome for a glass of ‘Calvados’. Radj Baldewsing (de autochtone maar niet de allochtone), sorry for disappointing you when you learned that I was a “simple” Ph. D. student and not a postdoc. I also thank the rest of the Exp Echo colleagues for sustaining an enjoyable working atmosphere, Boudewijn Krenning, Annemieke van Wamel, Johannes Schaar, Jerome Borsboom, Frans van Egmond, Esther Leung, Paul van Meer, Erik Droog and Marcia Emmer.

I would not forget Peter and Barbara, I hope you are used now to the Swiss “Patee”; María en Fermín, muchas gracias por vuestra amistad; Stéphane et Tine, un Rasteau vous attend au frais.

I would like to thank my “French Girls Connection” of Rotterdam: Odile, Zhajia, Florence, Marie, Marilyn and Faiza. Thanks for your friendship and for the nice French atmosphere that helped me to survive in the Netherlands!

I also thank all my friends in France, who supported me during this time away.

Un grand merci à toute ma famille et plus spécialement à Katia pour avoir pollué régulièrement ma mailbox et à mamy pour m'avoir tenue au courant des petits “potins” familiaux durant ces années d'exil. Je dédie aussi cette thèse à mes parents qui ont toujours soutenu mes choix et m'ont constamment encouragée durant ces longues années d'études. Je ne saurais oublier la grande qualité de leur service de livraison à domicile.

Special affection to my sweet boy, Enzo, for waking me up every morning at 6.00 am, singing your favorite song and for teaching me how life could be easy: eating banana and watching the Teletubbies.

Finally, Ayache. This thesis could not have been made without your support during all these years. I will try to resume my feelings with these few words: “Achkourouka aala kouli e'ssaaada ellati djalabta fi hayati”.

Curriculum Vitæ

Peggy Palanchon was born on April 9, 1973 in Rosny-Sous-Bois, France. She completed her high school education in 1991 at Lycée André Boulloche at Livry-Gargan, France. The same year she started her study at the University Pierre et Marie Curie (Paris VI) where she obtained her Master in Mechanics and Physics in 1996. In 1997, she completed her educational program at the Institut National des Sciences Appliquées (INSA) in Lyon, France where she obtained a Diplôme d'Etudes Approfondies (DEA) at the department of Acoustics. Her graduation project was carried out at the laboratory CREATIS (Centre de Recherche et d'Applications en Traîtement de l'Image et du Signal). From November 1997 to February 1999, she worked at the Whitaker Center, headed by Prof. K.K. Shung, Pennsylvania University, State College, USA. Her research project consisted of modelling and fabricating novel transducers for medical applications and particularly Doppler applications. Her research focused on the conception of the Diffracting-Grating transducer, which was developed in close collaboration with the industrial company EchoCath Inc., Princetown, USA. In March 1999, she started a new project at the Experimental Echocardiography, headed by Prof. dr. ir. N. Bom. The idea was to develop a simple ultrasonic device to measure non-invasively the volume of urinary bladder. In July 1999, she started a Ph. D. at Erasmus Medical Center, conjointly with the Anesthesiology Department, at the Laboratory of Experimental Echocardiography under the supervision of Prof. dr. ir. J. Klein and Prof. dr. ir. N. de Jong. Her Ph. D. research focused on the development of a new method using ultrasound to detect and characterize gaseous and solid microemboli.

List of publications

Peer reviewed international journals

- P. Palanchon, A. Bouakaz, J.H. van Blankestein, J. Klein, N. Bom and N. de Jong, “New Technique for emboli detection and discrimination based on nonlinear characteristics of gas bubbles”, *Ultrasound Med Biol*, vol. 27, no. 6: pp. 801-808, 2001
- P. Palanchon, A. Bouakaz, J. Klein and N. de Jong, “Subharmonic and ultraharmonic emissions for emboli detection and characterization”, *Ultrasound Med Biol*, vol. 29, no. 3: pp.417-425, 2003
- P. Palanchon, J. Klein and N. de Jong, “Production of standardized air bubbles: application to embolism studies”, *Rev Sci Instrum*, vol. 74, no. 4: pp. 2558-2564, 2003
- P. Palanchon, A. Bouakaz, J. Klein and N. de Jong, “Emboli detection using a new transducer design”, *Ultrasound Med Biol*, vol. 30, no. 1: pp. 123-126, 2004.
- P. Palanchon, D. Van Loon, N. Bom and C.H. Bangma, “Bladder volume measurements with a limited number of fixed sound beams”, *Ultrasound Med Biol*, vol. 30, no. 3: pp. 289-294, 2004.
- P. Palanchon, P. Tortoli, A. Bouakaz and N. de Jong, “Optical observations of acoustical radiation force effects on individual air bubbles”, *Accepted for publication in IEEE Trans Ultrason Ferr Freq Con*, 2004.
- P. Palanchon, A. Bouakaz, J. Klein and N. de Jong, “Multifrequency transducer for microemboli classification and sizing”, *Accepted for publication in IEEE Trans Biomed Eng*, 2004.

- P. Palanchon, A. Bouakaz, J. Klein and N. de Jong, “Modelling and optical measurements of the acoustic behavior of air bubbles’, *Submitted.*

Conference proceedings

- D. Vilkomerson, T. Chilipka, M. Delamere, P. Lopath, P. Palanchon and K.K. Shung, “Clinical blood flow measurements using diffraction-grating transducers”, *IEEE Ultrasonics Symposium Proceedings*, vol. 2: pp. 1501-1508, 1998.
- P. Palanchon, D. Vilkomerson, T. Chilipka and K.K. Shung, “Improved diffracting grating transducers”, *SPIE Proceedings Medical Imaging*, vol. 3664: pp. 155-160, 1999.
- P. Palanchon, H. Meeder, N. de Jong, J. Klein and N. Bom, “Emboli detection and discrimination using harmonic imaging”, *IEEE Ultrasonics Symposium Proceedings*, vol. 2, pp. 1497-1500, 2000.
- P. Palanchon, A. Bouakaz, J. Klein and N. de Jong, “Gaseous emboli detection through subharmonic and ultraharmonic emissions”, *IEEE Ultrasonics Symposium Proceedings*, vol. 2: pp. 1904-1907, 2002.
- P. Palanchon, P. Tortoli, A. Bouakaz and N. de Jong, “Observations of radiation forces effects on individual air bubbles with high-speed photography”, *IEEE Ultrasonics Symposium Proceedings*, 2003.
- P. Palanchon, A. Bouakaz and N. de Jong, “Air bubble oscillations in an ultrasound field: theoretical and optical results”, *IEEE Ultrasonics Symposium Proceedings*, 2004.
- P. Palanchon, A. Bouakaz, J. Klein and N. de Jong, “A new multifrequency transducer for microemboli detection”, *IEEE Ultrasonics Symposium Proceedings*, 2004.
- M. Versluis, P. Palanchon, D. Goertz, S. van der Meer,C.T. Chin, D. Lohse and N. de Jong, “Microbubbles surface mode”, *IEEE Ultrasonics Symposium Proceedings*, 2004.

Conference abstracts

- D. Vilkomerson, T. Chilipka, P. Lopath, P. Palanchon and K.K. Shung, “Clinical blood flow measurements using diffraction-grating transducers”, *IEEE Ultrasonics Symposium*, 1998.
- P. Palanchon, D. Vilkomerson, T. Chilipka and K.K. Shung, “Improved diffracting grating transducers”, *SPIE*, San Diego, CA, USA, 1999.
- P. Palanchon, H. Meeder, N. de Jong, J. Klein and N. Bom, “Emboli detection and discrimination using harmonic imaging”, *IEEE Ultrasonics Symposium*, Porto Rico, 2000.
- P. Palanchon, J. Klein, N. Bom and N. de Jong, “Air bubbles detection and sizing method using higher harmonics”, *6th European Symposium on Ultrasound Contrast Imaging*, Rotterdam, The Netherlands, 2001.
- P. Palanchon, J. Klein, N. Bom and N. de Jong, “Nonlinear response of gaseous emboli for clinical application”, *Euroecho*, Nice, France, 2001.
- P. Palanchon, A. Bouakaz, J. Klein, N. Bom and N. de Jong, “Emboli characterization using ultrasonic harmonic scattering”, *6th Meeting of the European Society of Neurosonology and Cerebral Hemodynamics*, Lisbon, Portugal, 2001.
- P. Palanchon, A. Bouakaz, J. Klein and N. de Jong, “New ultrasonic transducer for characterization of micro emboli”, *7th Meeting of the European Society of Neurosonology and Cerebral Hemodynamics*, Bern, Switzerland, 2002.
- P. Palanchon, A. Bouakaz, J. Klein and N. de Jong, “Gaseous emboli detection through subharmonic and ultraharmonic emissions”, *IEEE Ultrasonics Symposium*, Munich, Germany, 2002.
- P. Palanchon, A. Bouakaz, J. Klein and N. de Jong, “A new ultrasonic transducer design for detection and classification of microemboli”, *Ultrasonics Symposium*, Grenada, Spain, 2003.
- P. Palanchon, A. Bouakaz, J. Klein and N. de Jong, “Nonlinear bubbles properties applied to emboli detection and discrimination”, *5th World Congress on Ultrasonics*, Paris, France, 2003.

- P. Palanchon, P. Tortoli, A. Bouakaz and N. de Jong, “Observations of radiation forces effects on individual air bubbles with high-speed photography”, *IEEE Ultrasonics Symposium*, Hawaii, USA, 2003.

- M. Versluis, S. van der Meer, D. Lohse, C.T. Ching, D. Goertz, P. Palanchon and N. de Jong, “Surface modes of ultrasound contrast agents”, *9th European Symposium on Ultrasound Contrast Imaging*, Rotterdam, The Netherlands, 2004.

- P. Palanchon, A. Bouakaz, J. Klein and N. de Jong, “Multifrequency transducer for emboli classification”, *9th Meeting of the European Society of Neurosonology and Cerebral Hemodynamics*, Wetzlar, Germany, 2004.

- P. Palanchon, A. Bouakaz and N. de Jong, “Air bubble oscillations in an ultrasound field: theoretical and optical results”, *IEEE Ultrasonics Symposium*, Montréal, Canada, 2004.

- P. Palanchon, A. Bouakaz, J. Klein and N. de Jong, “A new multifrequency transducer for microemboli detection”, *IEEE Ultrasonics Symposium*, Montréal, Canada, 2004.

- M. Versluis, P. Palanchon, D. Goertz, S. van der Meer, C.T. Chin, D. Lohse and N. de Jong, “Microbubbles surface modes”, *IEEE Ultrasonics Symposium*, Montréal, Canada, 2004.